

# Investigation of Manufacturing and Characterization of Radar Absorbing Hybrid Structures

Submitted to the Graduate School of Natural and Applied Sciences  
in partial fulfillment of the requirements for the degree of

Doctor of Philosophy

in Material science and Engineering

by

Mohamed Yousef Ali Issa

ORCID 0000-0001-8131-4244

June 2022

This is to certify that we have read the thesis **Investigation of Manufacturing and Characterization of Radar Absorbing Hybrid Structures** submitted by **Mohamed Yousef Ali Issa**, and it has been judged to be successful, in scope and quality, at the defense exam and accepted by our jury as a DOCTORAL THESIS.

**APPROVED BY:**

**Advisor:** **Assoc. Prof. Dr. Hüsnügül Yılmaz Atay**  
İzmir Kâtip Çelebi University .....

**Committee Members:**

**Prof. Dr. Mücahit Sütçü**  
İzmir Kâtip Çelebi University .....

**Assoc. Prof. Dr. Onur Ertuğrul**  
İzmir Kâtip Çelebi University .....

**Assoc. Prof. Dr. Serdar Yıldırım**  
Dokuz Eylul University .....

**Assoc. Prof. Dr. Mustafa Erol**  
Dokuz Eylul University .....

**Date of Defense: June 24, 2022**

# Declaration of Authorship

I, **Mohamed Yousef Ali Issa**, declare that this thesis titled **Investigation of Manufacturing and Characterization of Radar Absorbing Hybrid Structures** and the work presented in it are my own. I confirm that:

- This work was done wholly or mainly while in candidature for the Doctoral degree at this university.
- Where any part of this thesis has previously been submitted for a degree or any other qualification at this university or any other institution, this has been clearly stated.
- Where I have consulted the published work of others, this is always clearly attributed.
- Where I have quoted from the work of others, the source is always given. This thesis is entirely my own work, with the exception of such quotations.
- I have acknowledged all major sources of assistance.
- Where the thesis is based on work done by myself jointly with others, I have made clear exactly what was done by others and what I have contributed myself.

Date: 24.06.2022

---

# Investigation of Manufacturing and Characterization of Radar Absorbing Hybrid Structures

## Abstract

Significant development of radar systems after World War II has led to studying the interaction between electromagnetic waves at radar frequencies and different materials. One perspective of these studies is to ascertain ways of decreasing reflected waves. However, the applications have not been limited only to defense applications but also to different fields where human beings are exposed to electromagnetic waves to avoid potential health effects due to exposure to electromagnetic waves. Since the discovery of radar systems, many studies have focused on electromagnetic radiation and absorbing materials to design a material with good reflection loss. Therefore, this work aims to manufacture material with unique properties such as strong absorption of electromagnetic waves, lightweight and thickness, and cost-effectiveness using a composite hybrid structure reinforced by cobalt oxide ( $\text{Co}_3\text{O}_4$ ), copper-copper oxide ( $\text{Cu-Cu}_2\text{O}$ ), and barium hexaferrite ( $\text{BaFe}_{12}\text{O}_{19}$ ). Chemical reduction and sol-gel were used for synthesizing reinforcement materials; barium hexaferrite, copper oxide, and cobalt oxide. Polyester resin was used as a matrix material. Synthesized powders were analyzed and characterized by using various characterization techniques such as differential thermal analysis, X-ray diffractions (XRD), vibrating sample magnetometer (VSM), scanning electron microscopy (SEM), and particle size analysis. Three-Layer RAM structures were prepared layer by layer, and the concentration of the filler powders was the same in each layer. RAM structures were investigated using a vector network analyzer (VNA). Based on the radar absorbing analysis, the most effective absorption is possessed by sample RA5 50 wt.%, which

consists of two layers of cobalt oxide and one layer of copper-copper oxide. The maximum value of the reflection loss was- 45 dB at a frequency of 10.25 GHz. The produced material can be used as a coating material due to its limited mechanical properties and is intended for military, medical, and household purposes.

**Keywords:** Radar absorbing material, cobalt oxide, copper-copper oxide, barium hexaferrite

# Radar Absorbsiyon Hibrit Yapıların İmalatı ve Karakterizasyonunun İncelenmesi

## ÖZ

İkinci Dünya Savaşı'ndan sonra radar sistemlerindeki önemli gelişmeler, radar frekanslarındaki elektromanyetik dalgalar ile farklı malzemeler arasındaki etkileşimin araştırılmasına yol açmıştır. Bu çalışmaların bir perspektifi, yansıyan dalgaları azaltmanın yollarını bulmaktır. Ancak uygulamalar sadece savunma uygulamalarıyla sınırlı kalmamış, elektromanyetik dalgalara maruz kalmanın olası sağlık etkilerinden kaçınmak için insanların elektromanyetik dalgalara maruz kaldığı farklı alanlarla da sınırlı kalmıştır. Radar sistemlerinin keşfinden bu yana, birçok çalışma, iyi yansıma kaybı olan bir malzeme tasarlamak için elektromanyetik radyasyon ve soğurucu malzemeler üzerine odaklanmıştır. Bu çalışma, kobalt oksit ( $\text{Co}_3\text{O}_4$ ), bakır-bakır oksit ( $\text{Cu-Cu}_2\text{O}$ ) ve baryum heksaferrit ( $\text{BaFe}_{12}\text{O}_{19}$ ) ile güçlendirilmiş kompozit hibrit yapı kullanılarak, elektromanyetik dalgaları güçlü absorpsiyon, hafif ve kalınlık gibi benzersiz özelliklere sahip ve uygun maliyetli malzeme üretmeyi amaçlamaktadır. Takviye malzemelerinin sentezlenme süreci; baryum heksaferrit ve kobalt oksit kimyasal indirgeme ve sol-jel kullanılarak yapılmıştır. Matris malzemesi olarak polyeşter reçine kullanılmıştır. Sentezlenen tozlar, diferansiyel termal analiz, X-ışını kırınımları (XRD), titreşimli numune manyetometresi (VSM), taramalı elektron mikroskobu (SEM) ve parçacık boyutu analizi gibi çeşitli karakterizasyon teknikleri kullanılarak analiz ve karakterize edildi. Üç katmanlı RAM yapıları, katman katman hazırlandı ve dolgu tozlarının konsantrasyonu her katmanda aynıydı. RAM'lerin yapıları vektör ağ analizörü (VNA) kullanılarak araştırılmıştır. Radar soğurma analizine göre en etkili soğurma, iki kat kobalt oksit ve bir kat bakır-bakır oksitten

oluşan ağırlıkça %50 RA5 numunesindedir. Yansıma kaybının maksimum değeri, 10.25 GHz frekansında - 45 dB idi. Üretilen malzeme, sınırlı mekanik özellikleri nedeniyle kaplama malzemesi olarak kullanılabilir ve askeri, tıbbi ve evsel amaçlar için tasarlanmıştır.

**Anahtar Kelimeler:** Radar absorpsiyon malzemeleri, baryum hekzaferrit, kobalt oksit, bakır oksit

*This work is dedicated to my parent.*



# Acknowledgment

First and foremost, I am incredibly grateful to my supervisor, Assoc. Prof. Dr. Hüsnügül Yılmaz Atay for her constant guidance, support, and great friendship and her unique and charming way of teaching the simplicity and beauty of science.

I would like to express my thanks to Allah, "God" who gave me the knowledge, and without his help and support, I would not have the ability to complete this project.

I would like to thank the Center for fabrication and Application of Electronic Materials "EMU" at Dokuz Eylul University for providing the necessary equipment for this work, especially Assoc. Prof..Dr. Mustafa Erol contributed to the work with his knowledge, and many thanks to Mr. Abdulvahid çelevi and Mr. Erman Demircilioglu, who helped in the characterization.

Finally, yet importantly, I would like to thank my family member, especially my parents, for their love, unfailing encouragement, patience, and assistance over the years. I am forever indebted to my parents, who have always kept me in their prayers.

# Table of Contents

<b>Declaration of Authorship</b> .....	<b>II</b>
<b>Abstract</b> .....	<b>III</b>
<b>Öz</b> .....	<b>V</b>
<b>Acknowledgment</b> .....	<b>VIII</b>
<b>Table of Contents</b> .....	<b>IX</b>
<b>List of Figures</b> .....	<b>XI</b>
<b>List of Tables</b> .....	<b>XIII</b>
<b>List of Abbreviations</b> .....	<b>XIV</b>
<b>1 Introduction</b> .....	<b>1</b>
1.1 Objective .....	1
1.2 The scientific novelty of the work.....	2
1.3 Importance of the research .....	2
<b>2 Electromagnetic waves and radar absorbing materials</b> .....	<b>4</b>
2.1 Electromagnetic waves .....	4
2.2 Loss mechanism in electromagnetic wave .....	8
2.3 Radar-absorbing material .....	13
2.4 Absorber materials .....	17
2.4.1 Barium hexaferrite .....	17
2.4.2 Copper.....	21
2.4.3 Cobalt oxide.....	22
2.5 Sol-gel process .....	23
<b>3 Experimental</b> .....	<b>27</b>
3.1 Materials.....	27
3.2 Production of fillers.....	27
3.2.1 Barium hexaferrite powders $\text{BaFe}_{12}\text{O}_{19}$ .....	27

3.2.2 Copper-copper oxide powder.....	28
3.2.3 Cobalt oxide.....	29
3.3 Preparation of composite samples.....	29
3.4 Characterization.....	32
3.4.1 X-ray diffraction analysis .....	32
3.4.2 Scanning electron microscopy .....	34
3.4.3 Particle size analysis .....	35
3.4.4 Thermal analysis .....	36
3.4.5 Vibrating sample magnetometer (VSM).....	37
3.4.6 Microwave network analyzer.....	38
<b>4 Results and discussion .....</b>	<b>41</b>
4.1 Phase analysis.....	41
4.2 Scanning electron microscope.....	43
4.3The energy dispersive X-ray (EDX).....	48
4.4 Particle analysis .....	49
4.5 Thermal analysis.....	51
4.6 Vibrating sample magnetometer (VSM).....	53
4.7 Density of composites .....	56
4.8 Microwave network analyzer .....	58
<b>5 Conclusion.....</b>	<b>71</b>
<b>References .....</b>	<b>73</b>
<b>Curriculum Vitae .....</b>	<b>89</b>

# List of Figures

Figure 1.1 The steps of the work.....	3
Figure 2.1 Electromagnetic spectrum .....	5
Figure 2.2 Explanation of the Radar Principle .....	14
Figure 2.3 Mechanisms of interaction between the intensity waves and material ....	15
Figure 2.5 Preparation of barium hexaferrite using goethite and barium carbonate..	19
Figure 2.6 Synthesizing of barium hexaferrite using d-fructose .....	20
Figure 2.7 Basic synthesizing process of cobalt steps using precipitation method ...	22
Figure 2.4 Sol-gel preparation steps.....	24
Figure 3.1 Synthetization steps of barium hexaferrite .....	28
Figure 3.2 Synthetization steps of copper powder .....	28
Figure 3.3 Synthesized cobalt oxide powder .....	29
Figure 3.4 RAM's preparation steps after placing; a) first layer, b) second layer and c) third layer .....	30
Figure 3.5 RAM samples .....	30
Figure 3.6 Panalytical Empyrean X-ray diffractometer .....	33
Figure 3.7 Brag's equation of diffraction.....	34
Figure 3.8 Sigma 300VP from Carl Zeiss scanning electron microscope .....	35
Figure 3.9 Master Sizer Hydro 3000.....	36
Figure 3.10 TA SDT Q600 Thermal analysis .....	37
Figure 3.11 Dexing Magnet VSM 550.....	37
Figure 3.12 Schematic showing a typical magnetic hysteresis loop.....	38
Figure 3.13 Agilent Technologies / PNA-L – N5230C .....	39
Figure 3.14 S-parameters .....	39
Figure 3.15 Simplified diagram of a vector network analyzer in forward transmission mode S11.....	40

Figure 4.1 XRD pattern of a) barium hexaferrite, b) cobalt oxide, c) Cu-Cu <sub>2</sub> O.....	43
Figure 4.2 SEM images of barium hexaferrite (a) 250 kx (b) 1.00 kx (c) 5 kx magnifications .....	44
Figure 4.3 SEM images of cobalt oxide (a) 250 x (b) 1.00 kx (c) 5 kx magnification .....	45
Figure 4.4 SEM images of copper- cuprous oxide (a) 250 x (b) 1.00 kx (c) 10 kx magnifications .....	45
Figure 4.5 SEM images of; a) RA2 5%, b) RA3 10%, c) RA4 10% , d) RA5 25% , e) RA5 50% and f) RA6 25%.....	47
Figure 4.6 SEM image of a) RA5 50%, b) RA3 15%, c) RA1 25% and d) RA6 25% sample cross section.....	47
Figure 4.7 EDX spectrum of a) barium hexaferrite, b) cobalt oxide and c) Cu and Cu <sub>2</sub> O .....	49
Figure 4.8 Particle size distribution of a) barium hexaferrite, b) cobalt oxide and c) Cu and Cu <sub>2</sub> O .....	50
Figure 4.9 TGA/DSC curve of a) barium hexaferrite, b) cobalt oxide and c) Cu -Cu <sub>2</sub> O .....	53
Figure 4.10 Magnetic hysteresis loop of a) barium hexaferrite, b) cobalt oxide and c) Cu and Cu <sub>2</sub> O .....	55
Figure 4.11 Reflection loss of RA1 as a function of frequency.....	59
Figure 4.12 Reflection loss of RA2 as a function of frequency.....	59
Figure 4.13 Reflection loss of RA3 as a function of frequency.....	60
Figure 4.14 Reflection loss of RA3 as a function of frequency.....	61
Figure 4.15 Reflection loss of RA5 as a function of frequency.....	62
Figure 4.16 Reflection loss of RA6 as a function of frequency.....	63
Figure 4.17 Reflection loss of 5% composites as a function of frequency .....	64
Figure 4.18 Reflection loss of 10% composites as a function of frequency .....	64
Figure 4.19 Reflection loss of 15% composites as a function of frequency .....	65
Figure 4.20 Reflection loss of 25% composites as a function of frequency .....	65
Figure 4.21 Reflection loss of 50% composites as a function of frequency .....	66
Figure 4.22 RL of composites containing 50% of BaFe <sub>12</sub> O <sub>19</sub> , Cu-Cu <sub>2</sub> , and Co <sub>3</sub> O.....	67

# List of Tables

Table 2.1 Maximum limits of permissible levels of exposure to electromagnetic radiation .....	7
Table 3.1 Design and composition and layer thickness of composites.....	30
Table 4.1 Magnetic properties of the synthesized samples.....	56
Table 4.2 Density of composites.....	56
Table 4.3 Summaries of reflection loss values.....	63

# List of Abbreviations

EM	Electromagnetic
WHO	World Health Organization
CENELEC	European Committee for Electromagnetic Standardization
ICNIRP	International Commission on Non-Ionizing Radiation Protection
IRPA	International Radiation Protection Association
EMR	Electromagnetic radiation
CVD	Chemical vapor deposition

# Chapter 1

## Introduction

### 1.1 Objective

The intensive development of scientific and technological progress has led to a sharp decrease in the safety of the environment associated with the emergence of new sources of electromagnetic pollution, such as cellular, satellite radio communications, navigation, and radar systems, radio installations, medical devices, household appliances and other technical means intended for transmission and use of electromagnetic energy. Electromagnetic radiation (EMR), generated by various sources, causes equipment and technology malfunctions and adversely affects human health. Radio-absorbing materials (RAM) and electromagnetic shields are one method of solving these problems. In this regard, many studies have been conducted to develop radio-absorbing materials (RAM) capable of ensuring the electromagnetic compatibility of radio-electronic devices, medical equipment, and other equipment associated with generating electromagnetic radiation as the production of unique clothing for human protection. Such materials should have a set of properties: an adequate level of absorption, flexibility, low weight, manufacturability, and low cost, which are primarily determined by the operating conditions of the type of object to be protected.

There is tremendous interest in RAMs that are effective in the microwave frequency band corresponding to the operation of most household and industrial sources of electromagnetic radiation.

The primary purpose of this study is to produce and develop flexible multilayer radio-absorbing materials with significant electrophysical properties for protecting humans



and other biological and technical objects from the effects of electromagnetic radiation in the radio frequency range.

Following the goal of the work, it was necessary to solve the following research tasks:

- a) Analyze literature that previously performed theoretical and experimental studies and scientifically substantiate approaches for developing flexible composite materials for human and equipment protection from electromagnetic radiation in the microwave frequency range.
- b) Develop a straightforward approach to fabricate an effective multilayer radar absorbing with a gradient distribution over the thickness.
- c) Establish a relationship between the reflection loss and concentration of the filler in the hybrid structure.

## 1.2 The scientific novelty of the work

- A comprehensive approach has been developed for fabricating flexible multilayer radar-absorbing materials based on cobalt oxide  $\text{Co}_3\text{O}_4$ , copper-copper oxide  $\text{Cu-Cu}_2$ , and barium hexaferrite  $\text{BaFe}_{12}\text{O}_{19}$  using polyester as a matrix. In general, most radar-absorbing studies used epoxy as a matrix material. This study investigated the microwave absorption capabilities of polyester matrix composite materials. It is worth mentioning that copper was proposed instead of copper-copper oxide. However, during synthesizing process, it found  $\text{Cu}$  particles that cannot be synthesized under given conditions. Therefore, as copper-copper oxide and have an excellent absorbing property in microwave frequencies, formed powder was chosen as an excellent alternative material.
- The relationship has been established between the frequency dependences of reflection loss of radar absorbing material, structural characteristics, and the concentration of reinforcement in each multilayer composite structure.

## 1.3 Importance of the Research

The findings of this work are useful for further developments and expand the understanding of radar-absorbing materials in terms of producing effective material with a simple preparation method and easy to utilize. Furthermore, as radar-absorbing

materials nowadays are not limited to only defense applications, the study could also benefit commercial uses in electromagnetic interference (EMI) shielding fields. The advantages of using structural multilayer radio-absorbing with a layer-by-layer gradient distribution of magnetic dispersed filler are a highly effective way of protecting against EM in the radio frequency range.

The fundamentals theory of wave propagation in a layered structure, scattering and transmission of electromagnetic waves, and evaluation of the effectiveness of multilayer structure were used. The step of this work is shown in Figure 1.1 and can be summarized as follow:

- 1- Synthesizing and preparing additives or reinforcement materials; using different synthesizing methods, barium hexaferrite  $\text{BaFe}_{12}\text{O}_{19}$ , cobalt oxide  $\text{Co}_3\text{O}_4$ , and copper-copper oxide  $\text{Cu-Cu}_2$ .
- 2- SEM, XRD, particle analysis and DTA were performed on powder samples.
- 3- Polyester resin was used as a matrix due to its lightweight nature, good dielectric properties, and impact resistance, and it could perform more efficiently when used as a multilayer structure.
- 4- Multiple layers of structures were prepared by using additives with equal thickness. The absorption properties of the structures were investigated

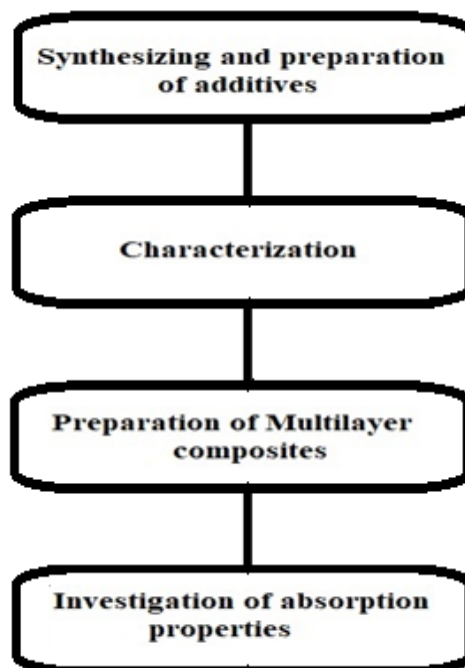


Figure 1.1: The flow chart of the study

# Chapter 2

## Electromagnetic waves and Radar absorbing materials

### 2.1 Electromagnetic waves

Electromagnetic waves are a form of energy with an electric and magnetic field created when a charged particle is accelerated by an electric field, causing it to move. In the 1870s, a scientific theory was developed by the Scottish physicist Maxwell James to describe electromagnetic waves. Maxwell noticed that Electricity and magnetism fields could be compatible with forming electromagnetic waves and summarized this relationship between electric and magnetic to what is known as Maxwell's Equation. Electromagnetic waves emerge spontaneously in nature. The natural electromagnetic field exists in the north-south direction around the earth's globe and consists of waves that help the birds find their way but are not visible. In addition to natural electromagnetic fields, also emitted from artificial sources cover the entire environment in daily life.

Human-made electromagnetic sources include x-ray devices that are the source of X-rays, low-frequency electromagnetic wave sources, data transmission lines such as TV antennae emitting high-frequency radio waves, radio stations, or mobile phones. Electromagnetic waves are classified according to frequency, such as radio waves, microwaves, X-rays, and gamma rays. Sunlight is also a form of EM energy, but visible light is only a tiny portion of the electromagnetic spectrum (Figure 2.1) [1]. New technological products cause the formation of electromagnetic radiation intensively in daily life. In the field of health, security systems have become connected to products that emit electromagnetic waves to facilitate people's lives and provide

comfort, high voltage lines, TV and computers, FM and TV transmitters, microwave ovens, mobile phones, wireless phones, satellite antennas and transmit antennas, radar antennas. However, while increasing living standards, electromagnetic pollution also is rising as electromagnetic radiation. In the last part of the 20th century, a significant scientific and technological development led to an increase in the use of electromagnetic and electrical energy, which caused the emergence and formation of new environmental pollution known as electromagnetic. In recent decades, new sources of electromagnetic pollution have been added to the natural electromagnetic of the earth. These new sources of electromagnetic pollution include cellular communication, radio communication, remote monitoring, and control equipment, household appliances, medical radio

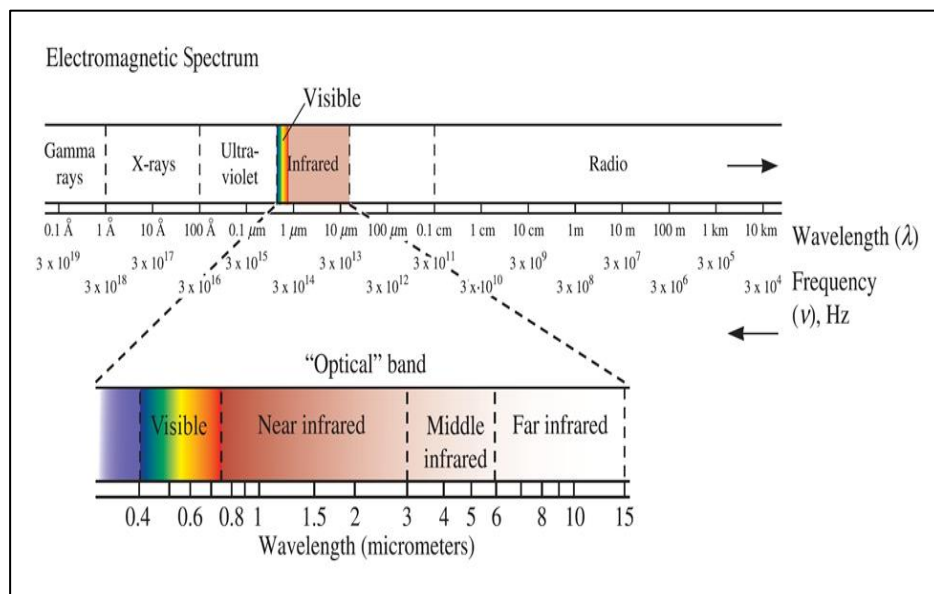


Figure 2.1: Electromagnetic spectrum

engineering and other equipment generate electromagnetic energy into the environment [2-3]. The World Health Organization (WHO) formally introduced the term "global electromagnetic pollution of the environment" in 1995. The organization also listed the issue on the priority environmental concerns list. The World Health Organization (WHO), in collaboration with other international organizations such as the European Committee for Electromagnetic Standardization (CENELEC), the International Commission on Non-Ionizing Radiation Protection (ICNIRP), and the International Radiation Protection Association (IRPA), established the international electromagnetic fields project to investigate the potential health risks associated with technologies that emit electromagnetic fields (EMF). Almost all developed countries

nowadays have national programs for researching the biological effects of electromagnetic interference and ensuring the safety of humans and ecosystems considering the new global electromagnetic factor of environmental pollution. These programs are designed to provide that electromagnetic pollution does not negatively impact the environment [4]. The term "electromagnetic radiation" (EMR) refers to radiation that combines electrical, magnetic, and electromagnetic effects. This type of radiation exhibits a broad spectrum of frequencies and ranges in terms of its levels of intensity. Electromagnetic radiation can be classified based on its natural or artificial origin (technogenic). The electromagnetic field of the earth and the radio waves produced by astronomical objects (sun, galaxies, etc.) are examples of natural fields. Anthropogenic refers to various technical installations used in industry, electronic equipment used in the home and workplace, and different gadgets [5-6]. The interaction between the natural electromagnetic field and the artificial one contributes to the issue of electromagnetic pollution by making it worse. The human body performs its essential functions via various complicated processes, such as intracellular and extracellular electromagnetic interactions [7]. Electromagnetic fields with a frequency over 300 GHz with an energy flux density of around  $0.003 \text{ W/m}^2$  are emitted by the human body. The natural electromagnetic field plays a role in the existence of life on earth; therefore, there is a contradiction between the role of the natural electromagnetic field as a factor in the existence of life on earth and the artificial electromagnetic pollution generated by the human body, which poses a threat not only to human being but also to other living organisms and plants.

Biological objects in the process of evolution have adapted to a certain level of electromagnetic radiation; however, a sharp increase in its level and duration causes a strain on a person's adaptive capabilities, leading to their depletion and irreversible structural changes in the body [8]. Long-term exposure of the human body to microwave radiation has a negative impact and can cause a variety of adverse biological responses, including but not limited to an increase in the overall temperature of the body or of its parts; pain reactions in the brain, eyes, kidneys, stomach, and intestines; decreased physical activity; mental and emotional conditions, etc. Therefore, the solution to the problem of protecting people's health in modern society is directly dependent on ensuring a safe level of electromagnetic radiation (EMR) and strict compliance with sanitary and hygienic standards for microwave-emitting

equipment and devices [9]. Reducing the intensity of electromagnetic radiation to levels below the allowed permissible exposure limit (PEL) is a way to protect the human body from the potentially hazardous effects of this kind of radiation. It is based on providing a threshold for electromagnetic radiation's damaging effects. The maximum permissible level of EMR is the value that does not produce variations in the state of health or disorders to a person when exposed to it every day. The maximum permissible levels are the leading EMR indicators regulated by the authorities' established standards. The limits of the permissible level of exposure to electromagnetic radiation for different frequency ranges of electromagnetic waves according to ICNIRP are given in Table 2.1

Table 2.1: Maximum limits of permissible levels of exposure to electromagnetic radiation [10]

Applies to:	Type of Restriction	Quantity	Part of Body	Value
Occupational exposure	Basic Restriction	J	Central nervous system (includes spinal cord)	$10 \text{ mA m}^{-2}$
	Reference Level	E B Contact current		$10 \text{ kV m}^{-1}$ $500 \text{ }\mu\text{T}$ 1 mA
General public exposure	Basic Restriction	J	Central nervous system (includes spinal cord)	$2 \text{ mA m}^{-2}$
	Reference Level	E B Contact current		$5 \text{ kV m}^{-1}$ $100 \text{ }\mu\text{T}$ 0.1 mA

Another significant issue that arises in connection with electromagnetic radiation is the issue of electromagnetic compatibility, also known as EMC. This issue is currently considered one of the most crucial in the electric power field, both in terms of its theoretical and practical implications. The relevance of this issue is on par with that of other well-known issues, such as the environment, energy security, and energy efficiency [11]. Failure to comply with EMC rules may have significant repercussions in various spheres of human activity. These repercussions can range from a reduction in the quality of the functioning of technological equipment to false operations and failure. For a long time, the EMC issue was ignored; nevertheless, when interference started causing widespread problems in financial systems, it became clear that

something needed to be done. As a result, directive 336 EU 89 was adopted, which required the European union member states to build a certification system and implement criteria for electromagnetic compatibility [12]. As a direct consequence, it has been illegal in Europe since 1996 to sell technical products that do not have a certificate proving that they comply with electromagnetic compatibility regulations [13]. By decision No. 879 of the Directorate-General for Taxation and Customs Union dated December 9, 2011, the technical regulation of the Customs Union TR CU 020/2011, "Electromagnetic compatibility of technical means," was adopted. This regulation applies to technical devices put into circulation in the familiar customs territory of the Customs Union that can cause electromagnetic interference and (or) the quality of functioning of which depends on the impact of external electromagnets [14].

In conclusion, electromagnetic radiation is an essential component of human existence; yet it is also an environmental risk that contributes significantly to the degradation of the ecosystem. In this regard, the issues of protection of biological and technological from the potentially harmful effects of electromagnetic radiation (EMR) are of undeniable scientific and practical significance.

## 2.2 Loss mechanism in electromagnetic wave

The main reason for the decrease in the EMR energy upon entry and propagation in a radio-absorbing material is the processes of polarization, conduction, and magnetization [15, 16].

The process of polarization is more susceptible to materials related to dielectrics, which act as matrices in RAM. According to theoretical concepts of physics of dielectric materials. In the structure of dielectrics, there are charged particles and positively and negatively charged ions. When the material is exposed to an external electric field, positive charges are oriented in the direction of the electric field vector, and negative charges are oriented in the opposite direction; thus, electronic, ionic, and dipole polarizations can occur in the material. The loss of energy of a high-frequency electromagnetic field in dielectrics is relaxation loss due to inelastic polarization [17]. The inelastic type of polarization includes dipole relaxation ion-relaxation and structural polarizations. The dipole is characterized by the orientation of dipolar molecules in the direction applied electric field, and the polarization process takes

place in a short time of  $10^{-2} - 10^{-10}$  s; this leads to a lag time of the relaxation process with the change in the applied external electromagnetic field, which oscillates with the frequency of the corresponding radio bands. Ion-relaxation polarization is observed in amorphous structures (glasses, ceramics, etc.) and inorganic crystalline dielectrics with loosely packed structures. Structural polarization is observed in composite materials and dielectrics containing conductive and semiconducting inclusions or layers with different conductivity. Losses of electromagnetic energy of resonant absorption occur when the frequency of the electric field approaches the frequencies of natural oscillations of electrons or ions [18]. In the structure of conductors, free electrons that have lost a strong bond with their atom can convert the energy penetrating the material because of the action of an external electromagnetic field into the kinetic energy of their directed motion. Energy losses inside the conductor are associated with electrical resistance arising from electron-phonon interaction, that is, during the scattering of electrons by defects in the crystal lattice and thermal vibrations of the lattice

The behavior of the material in the presence of an external electromagnetic field is described by the major electrophysical parameters:

1. Complex values of the permittivity ( $\varepsilon$ ) and permeability ( $\mu$ ):

$$\varepsilon = \varepsilon' - i\varepsilon'' \quad (2.1)$$

$$\mu = \mu' - i\mu'' \quad (2.2)$$

Where  $\varepsilon'$  and  $\mu'$  are the real parts of the permittivity and permeability, respectively;  $\varepsilon''$  and  $\mu''$  are the imaginary parts of permittivity and magnetic permeability, respectively.

2. Tangents of dielectric and magnetic losses:

$$\tan\delta\varepsilon = \frac{\varepsilon''}{\varepsilon'} \quad (2.3)$$

$$\tan\delta\mu = \frac{\mu''}{\mu'} \quad (2.4)$$



The wave equations describe the propagation of EMW deep into the material for the strength of the electric (E) and magnetic (H) fields:

The phase constant (k') and absorption coefficient (k'') are the real and imaginary parts of the complex wave number and are determined by the main electrophysical characteristics of the material:

$$k = \omega \sqrt{\varepsilon \varepsilon_0 \mu \mu_0} \quad (2.5)$$

$$k = \omega \sqrt{\frac{\varepsilon \varepsilon_0 \mu \mu_0}{2} \left[ \sqrt{1 + \frac{\sigma^2}{(\omega \varepsilon \varepsilon_0)^2} + 1} \right]} \quad (2.6)$$

$$k = \omega \sqrt{\frac{\varepsilon \varepsilon_0 \mu \mu_0}{2} \left[ \sqrt{1 + \frac{\sigma^2}{(\omega \varepsilon \varepsilon_0)^2} - 1} \right]} \quad (2.7)$$

When an electromagnetic wave is incident on an interface between media, the reflection from the interface (material surface) is observed due to the difference in the wave impedances of the free space and the material. Wave impedance (Z) is the ratio of the coupled transverse components of the electric and magnetic fields with the direction of propagation of the electromagnetic wave.

$$Z = \frac{|E|}{|H|} = \sqrt{\frac{\varepsilon \varepsilon_0}{\mu \mu_0}} = \frac{\omega \mu \mu_0}{K} = \frac{K}{\omega \varepsilon \varepsilon_0} \quad (2.8)$$

In the case of the dielectric material, the equation changes to:

$$Z = Z_0 \sqrt{\frac{\mu'}{\varepsilon' (1 - i \tan(\delta))}} = Z_0 \sqrt{\frac{\mu'}{\varepsilon'} \left( 1 - i \frac{\tan(\delta)}{2} \right)} \quad (2.9)$$

In the conductor materials case, the equation changes to:

$$Z = Z_0 \sqrt{\frac{\mu'}{\epsilon'(1 - i \tan(\delta))}} = (1 + i) \sqrt{\frac{\omega \mu \mu_0}{2\delta}} \quad (2.10)$$

The Fresnel formulae can be used to obtain the amplitude values of the reflection and transmission coefficients at the interface by knowing the values of the wave resistances of the media in which the electromagnetic wave propagates. E and H are both perpendicular to the propagation direction. Their orientation to the plane of incidence is arbitrary, affecting the reflection and refraction of the wave. Perpendicular and parallel polarizations are often considered. Since the standard reflection coefficient is the most accessible criterion for evaluating RAM, there is no difference between perpendicular and parallel components. Fresnel's equations that are used for this case are:

$$r_E = \frac{Z_2 - Z_1}{Z_2 + Z_1} = -r_H \quad (2.11)$$

$$t_E = \frac{2Z_2}{Z_2 + Z_1} = \frac{Z_2}{Z_1} t_H \quad (2.12)$$

Where:

- $r_E$  and  $r_H$  are the amplitude reflection coefficients of the electric and magnetic components, respectively
- $t_E$  and  $t_H$  are the amplitude transmission coefficients of the electric and magnetic components, respectively.

In the general case, the structure of the wave process includes an incident one, reflected from the interface between the media, and a refracted one and propagated deep into the material. The amount of energy transferred through a unit of surface, perpendicular to the direction of energy propagation, per unit of time is determined by the Poynting vector [19]. Therefore, when considering fields that change according to a harmonic law, it is correct to use characteristics averaged over time for waves propagating in absorbing media; the Poynting vector has the following formula:

$$\bar{S} = x_0 \frac{E_m^2}{2|Z|} e^{-2k'x} \cos\varphi_z \quad (2.13)$$

$$\varphi_z = \frac{k''}{k'} \quad (2.14)$$

Where  $\varphi_z$  The Independent variable of wave resistance represents the phase lag between magnetic field electric.

The law of conservation of energy, in this case, is expressed by the following equation:

$$x_0(\bar{S}_i + \bar{S}_r) = x_0\bar{S}_t \quad (2.15)$$

The energy values for reflection coefficients ( $\Gamma$ ) and transmission (T) are determined by the following expressions:

$$\Gamma = \frac{\bar{S}_r}{\bar{S}_i} \quad (2.16)$$

$$R = \frac{\bar{S}_t}{\bar{S}_i} \quad (2.17)$$

The energy and amplitude reflection and transmission coefficients are linked through the transformation formulas:

$$R = |r_E^2| \quad (2.18)$$

$$R = |r_E^2| \quad (2.19)$$

The reflection and transmission coefficients can be determined in terms of the complex refractive index:

$$R = |r^2| = |r_0^2| \frac{1 + \exp(-4\beta) - 2\cos(2\alpha) \exp(-2\beta)}{|r_0|^4 \cdot \exp(-4\beta) + 1 - 2 \cos(2\alpha - 2\varphi) |r_0|^2 \exp(-2\beta)} \quad (2.20)$$

$$\Gamma = \frac{1 + |r_0|^4 - |r_0|^2 \cos\varphi}{|r_0|^4 \cdot \exp(-4\beta) + 1 - 2 \cos(2\alpha - 2\varphi) |r_0|^2 \exp(-2\beta)} \exp(-2\beta) \quad (2.21)$$

These equations are the basis of calculation methods for the development of multilayer materials with given frequency characteristics of the reflection coefficient

## 2.3 Radar-absorbing material

A radar is a system that works with electromagnetic radiation to determine and recognize objects' location, distance, and speed by using radio waves. The Radar Principle of operation is shown in Figure 2.2. Radar transmitters send out electromagnetic waves, and when they hit an object in the visible range, waves are reflected on the radar receiver again for interpretation [20]. The radar system is a significant threat to aircraft. Since World War II, radar absorption technology has attracted much consideration as a possible way of reducing this threat. RADAR is an acronym for Radio Detection And ranging coined by United States Navy in 1940. Many different methods can be taken to protect biological and technological objects from the harmful effects of electromagnetic radiation (EMR), and these methods can be conditionally categorized into organizational or engineering and technical. Organizational methods such as protection by distance (location at the maximum allowable distance from the EMR source); time protection, protection by quantity (the intensity level of EMR should be minimum as possible); protection by quality Engineering and technical methods the use of unique protective materials, use of individual and collective protective equipment and designs improvement [21-22].

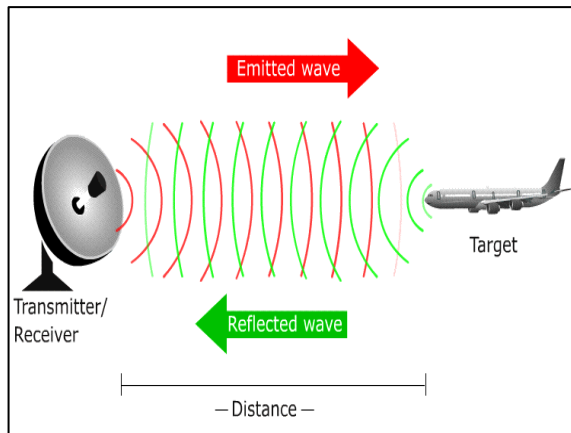


Figure 2.2: Explanation of the Radar Principle [23]

Engineering and technological methods, in particular, the discovery and construction of unique protective materials for shielding, are the most important in scientific research and practical application. In most cases, two different forms of shielding are considered: protecting EMR sources from people and shielding people from EMR sources. Only feasible at the stage of product development or design to include unique protective materials against the magnetic field produced by industrial frequencies. Earlier research on absorbing material began in the 1930s [24]. In 1936 the first patent appeared for the wave-absorbing material in the Netherlands. This absorber was a quarter-wave resonant material; carbon black was used for dissipation, and titanium dioxide due to its excellent permittivity in thickness reduction [25]. Iron, steel, copper, brass, and aluminum are among the metals used as radar absorbers for EMI shielding in microwave frequency bands.

In 1945 radar-absorbing material was used for military purposes, and in the 1950s, the first production of radar-absorbing materials for commercial purposes started [26]. Since then, several studies have been carried out to improve and design a material with minimum reflection loss by using different materials with various methods. However, the absorption of electromagnetic radiation mainly relies on attenuation within the materials. They are three different mechanisms by which the intensity of electromagnetic decreases (Figure 2.3). Absorption of the wave as it travels through the material, the reflection of the incident wave, and multiple internal reflections of the waves. Skin depth is the factor that determines the distance that a wave must propagate within the material before its amplitude and mainly depends on incident wave frequency [27]. An excellent electric conductor material has zero skin depth. In

other words, electric conductor materials have a higher ability to absorb electromagnetic waves. Usually, the absorbing material is designed with materials with absorption, low density, wide frequency range and thickness, and even good mechanical properties. Polymer composites reinforced with dielectric and magnetic fillers are widely used and incorporated as radar-absorbing material. In other words, radar-absorbing materials consist of a combination of materials in such a way that the loss of reflection is as low as possible in a wide frequency range by mixing polymeric matrix reinforced with absorbers, such as ferrites, carbon, iron, cobalt, copper, etc. particles. Because of their excellent dielectric and magnetic properties, ferrites are considered great magnetic substrates for electromagnetic wave absorbers, but they are costly. Therefore, many studies have been conducted to prepare polymer-based composites reinforced with magnetic materials to investigate the effect of reinforcements concentration on the radar-absorbing properties.

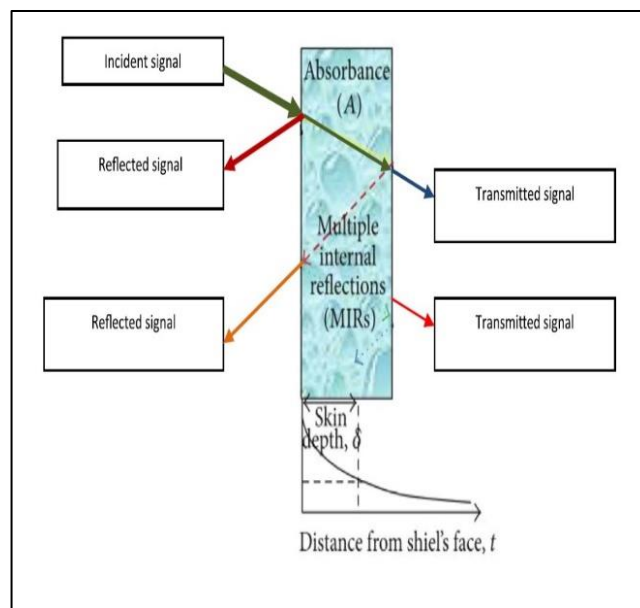


Figure 2.3: Mechanisms of interaction between the intensity waves and material [27]

Atay and Celik [28] studied the effects of barium hexaferrite-reinforced polymer composites on radar absorption performance. Three different amounts of barium hexaferrite were used (5%,10%, and 20%). It has been claimed that the absorption properties increased consistently with increasing barium hexaferrite content. However, the highest absorbing value observed was 12.13%. Abbas et al. [29] investigated the absorption properties of ferrite-polymer composites reinforced with different amounts of ferrite in the 8.2-12.4 GHz frequency range. The results showed that the absorption

properties are improved with increasing ferrite amount. For example, the minimum reflection loss was -24,5 dB at 12 GHz, showed by composite with 80 wt—% of ferrites.

Atay [30] investigated the dependence of barium hexaferrite particle size on absorption properties. Atay pointed out that decreasing the particle size of hexaferrite improves the absorption properties of the material even with a low amount of it.

Some researchers designed a multilayer absorbing structure as a possible way to improve absorption properties. Deng et al. [31] designed a multilayer structure using different concentrations of graphite powder and manganese dioxide. Structures with two and three layers were prepared. Absorption properties were analyzed, and it was found that the average absorption of double-layer samples in the 8-18 GHz frequency range is -12.3 dB. The 3-layer sample absorption peak is -18 dB. Kim [32] used carbon nanocomposites as radar-absorbing material with double layers structure. E glass-epoxy composite reinforced carbon black, carbon nanofibers, and carbon nanotubes were used to prepare double layers structure. The first layer of the structure was pure E glass-epoxy composite laminates, and the second layer was carbon nanocomposite laminates reinforced with carbon black, carbon nanofibers, and carbon nanotubes. It was reported that a significant absorbing performance was obtained. Das et al. [33] studied the absorption properties of double-layer radar-absorbing materials based on barium hexaferrite, doped barium hexaferrite, TiO<sub>2</sub>, and conducting carbon black. The first layer was 30% hexaferrite and 10% titanium dioxide, while the second was 30% hexaferrite and 10% conducting carbon black embedded in the chloroprene matrix. The resulting material showed a reflection loss of -32 dB at 10 GHz observed for the double-layer absorber-based barium hexaferrite, whereas -29 dB at 11 GHz for the doped barium hexaferrite absorber. Teber et al. [34] designed radar-absorbing structures using polymeric polyacrylonitrile (PAN) fabrics as a host matrix for magnetic metal nanoparticles (cobalt and nickel) with relative concentrations of nickel and cobalt at various coating times. The PAN samples with the shortest coating time showed the best return losses, less than -20 dB return loss over a moderate bandwidth.

Lee et al. [35] used rice husk to prepare absorber material as the rice husk is an agricultural waste and 37% of it is carbon. Therefore, rice husk was also mixed with carbon nanotubes for comparison. The authors concluded that the absorption

properties of rice husk mixed with carbon nanotube absorbers were higher than rice husk absorbers in the frequency range of 12.4 to 18 GHz.

Recently, there has been a suggestion to use radar-absorbing materials to prevent interference effects in many electronic devices Hunjra et al. [36]. In addition, wind turbine blades could also affect radar systems near airports and military bases by causing false signals. To eliminate this effect, some researchers proposed using radar-absorbing materials in the wind blade structures to shield and prevent interference effects [37,38,39].

Although the literature abounds with studies aimed at manufacturing material with higher absorbing properties, there is still a need to improve the reduction in reflection using simple and practical technology.

## 2.4 Absorber materials

### 2.4.1 Barium hexaferrite

Barium hexaferrite is an important permanent ferrimagnetic ceramic that attracted much interest and intensive research conducted in recent years due to its high saturation magnetization, excellent chemical stability, high coercive force, wear resistance, strong magneto crystalline anisotropy field, high Curie temperature, good corrosion resistivity, etc. Barium hexaferrite is usually used as electromagnetic wave absorbers and in chip inductors and microwaves. Various techniques for synthesizing barium hexaferrite have been suggested, such as the sol-gel method [40], a hydrothermal method [41], chemical precipitation [42], and the molten salt method [43], etc. All these methods involve two fundamental processes: mixing raw materials either mechanically or chemically and then heat treatment of the mixture at high temperatures between 700 to 1400 °C. Due to the high temperatures, the barium hexaferrite grain size in most cases is greater than 50 nm.

The chemical precipitation process and the sol-gel method of preparing have been used successively to synthesize barium hexaferrite with excellent magnetic properties, high purity, ultrafine, and good dispersion. The molten salt method has been widely used for synthesizing barium hexaferrite because it has a low synthesis temperature, and no



mechanical grinding is needed. This route is based on providing a molten salt environment to react with raw material, which is much easier than a solid-state reaction. However, it has been found that the synthesis conditions of several mixed metal oxides in molten salt impact their physical properties. Yoon et al. [44] synthesized barium hexaferrite using molten salt.  $0.8\text{Na}_2\text{SO}_4 + 0.2\text{K}_2\text{SO}_4$  molten salt and  $\text{Fe}_2\text{O}_3$ ,  $\text{BaCO}_3$  were used as starting materials. The reactants and molten salt mixtures have been ball-milled for 6 hours in ethanol. In an alumina crucible, the mixtures were dried and cooled in air. Distilled water was used to wash salt mixtures out to remove the salt anion from the aliquot after the residual powders had dried. Hai-Feng et al. [45] prepared barium hexaferrite using molten salt to study the effects of calcination temperature, molten salt addition,  $\text{Fe}_{3+}/\text{Ba}_{2+}$  molar ratio, and reaction time particle morphology and magnetic properties. Hai-Feng found that the amount of molten salt greatly influences particle morphology, and the  $\text{Fe}_{3+}/\text{Ba}_{2+}$  molar ratio affects magnetic properties. However, using  $\text{BaCO}_3$  as starting material can create  $\text{BaSO}_4$  precipitate by reacting with molten salt, which is not easy to extract and most properly affects the efficiency.

.Many studies have been conducted on synthesizing barium hexaferrite using sol-gel. For example, Li et al. [46] synthesized barium hexaferrite using the sol-gel process. The raw materials were metal nitrates (iron and barium nitrates) and citric acid. First, sufficient quantities of iron nitrate and barium nitrate were dissolved in deionized water to achieve a transparent solution. Citric acid was then added to the solution and stirred for a few minutes. The solution was then heated at 60-80 °C to evaporate the water and held in a furnace at 150 °C for 48 hours. Finally, the dried gel was calcinated in the air at variable temperatures.

Mozaffari et al. [47] found that barium hexaferrite nanopowders can be easily obtained using goethite and barium carbonate as starting materials in the sol-gel combustion technique. Barium hexaferrite nanopowders were prepared by pouring the desired amount of goethite into distilled water. The solution was then stirred and heated. Next, citric acid, a small amount of benzoic, and acid ethylene glycol were added to the solution. Through evaporation of the water and the solution turned into an orange gel. Eventually, the burnt powders were calcinated in the air at 900°C for 5h to get barium

hexaferrite power. The preparation steps of barium hexaferrite using goethite and barium carbonate are shown in Figure 2.5.

Kanagesan et al. [48] synthesized barium hexaferrite using d-fructose as a fuel. Iron (III) nitrate, nonahydrate, barium nitrate, and d-fructose were used as starting materials. First, metal nitrates and D-fructose were dissolved in deionized water, stirred continuously for 2 h to get a solution (sol), and then heated with stirring until it became a sticky liquid gel. Next, the gel was preheated in a convection oven to extract the precursor powder for 2 days. Finally, the precursor calcinated at 900°C for 3 hours to produce hexaferrite barium material. Figure 2.6 summarizes the preparation steps of barium hexaferrite using d-fructose as a fuel.

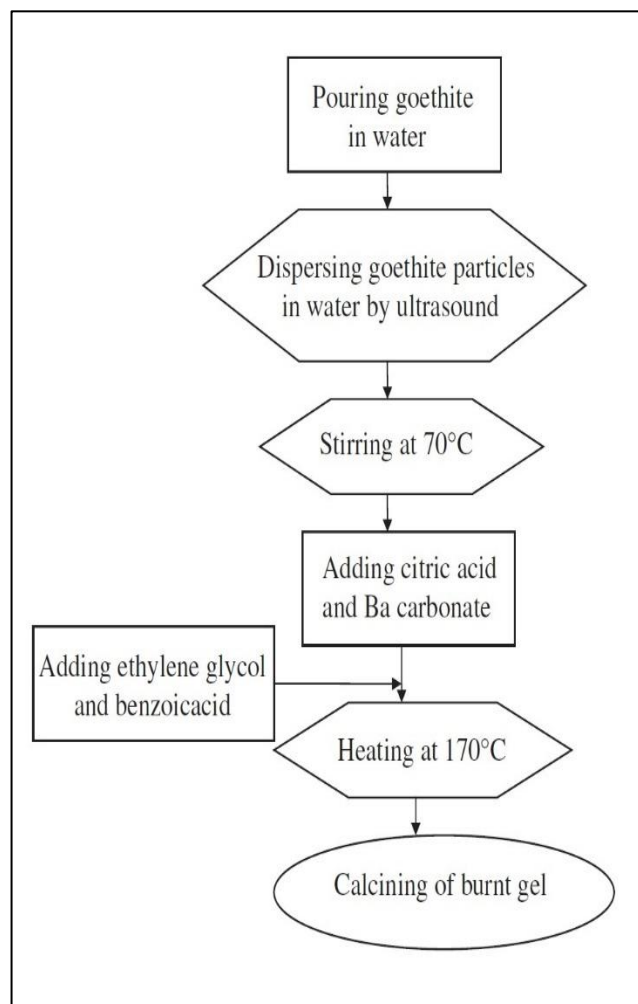


Figure 2.4: Preparation of barium hexaferrite using goethite and barium carbonate  
Coprecipitation can be considered one of the most straightforward techniques to use. However, synthesizing ultra-fine nanosized particles with this technique is still not

easy because of the particle coagulation. Chen et al. [49] synthesized ultrafine particles of barium hexaferrite by Coprecipitation. Polyacrylic acid sodium salt aqueous solution was first prepared by mixing it with water; then, the final solution was combined with an equivalent quantity of aqueous solution comprising barium nitrate. A high concentration of NaOH was added to the solution to ensure the total precipitation of  $Ba_2C$  and  $Fe_3C$  ions by stirring to create the mixed hydroxide precipitate. Precipitates of mixed hydroxide were washed with water twice to remove  $NaCl$  and  $NO_3$  ions, then vacuum-dried; the dried precursor was calcined.

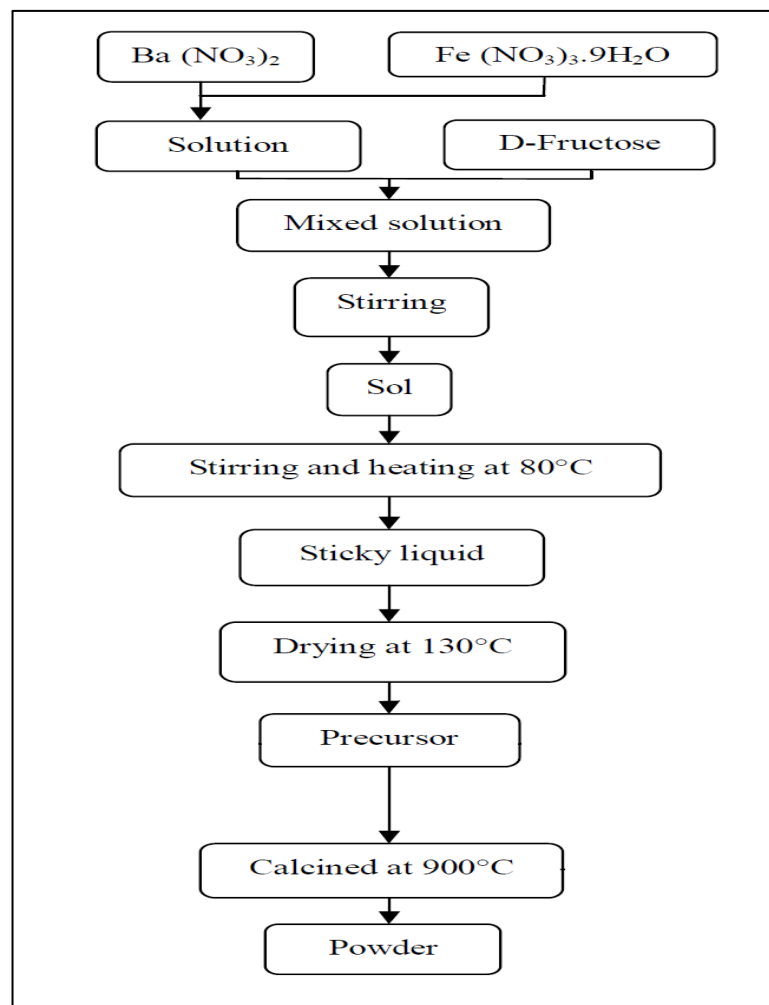


Figure 2.5: Synthesizing of barium hexaferrite using d-fructose

## 2.4.2 Copper

In recent decades, significant progress has been made in producing and researching metal oxide and metal nanoparticles. The production of metal nanoparticles is now one of the most promising research fields. There is significant interest in synthesizing copper powders due to their unique properties, such as catalytic action and antibacterial activity, and the capacity to demonstrate high thermal and electrical conductivity. Copper oxides are among the most promising and widely demanded materials due to their unique properties and affordable prices. Copper powders are used in various applications, including medicine (antibacterial agents), nanocircuits in the electrical sector, flexible electronics and printing, lubricants, antibacterial agents in medicine, and chemical technologies (catalysts). The properties of materials are known to be strongly influenced by their particle properties, such as oxidation rate, size, and ability to agglomerate morphology. Therefore, when synthesizing particles, it is crucial to consider the factors that affect the above parameters; therefore, during the synthesizing process of nanoparticles is essential to consider these parameters. Copper can be synthesized by various methods, including laser ablation [50], chemical vapor deposition [51], thermal decomposition [52], biochemical synthesis (green synthesis) [53,54], radiolysis [55], and chemical reduction [56,57]. However, due to the high oxidation rate, only a few synthesis methods can produce stable copper nanoparticles. The chemical reduction method is the most often used method for producing stable colloidal dispersions of copper because of its simplicity, economical, and ease of controlling the size and shape of the particles. This method has many drawbacks, including wide size distribution and the aggregative instability of the synthesized NPs. To obtain the copper powder, Khanna et al. [58] used a system consisting of an aqueous solution of copper (II) chloride, a pH regulator, and a reducing agent (hydrazine) in the presence of micelles of a surfactant sodium dodecyl sulfate (SDS). Many parameters affect the formation of copper NPs in redox reactions, such as temperature, the nature and concentration of the reducing agent, the presence and stabilizing agents, the nature of the solvent, and pH.

### 2.4.3 Cobalt oxide

Cobalt oxide powder,  $\text{Co}_3\text{O}_4$ , has various applications in various industries, including anode materials for rechargeable lithium-ion batteries, catalysts, gas sensors, and magnetic materials, including data storage devices. These are only a few of the many uses for cobalt oxide. Cobalt oxide is an essential p-type magnetic semiconductor with a spinel crystal structure. This structure is based on a close-packed cubic lattice of oxide ions, in which Co (II) ions occupy the tetrahedral centers and Co (III) ions occupy the octahedral centers. Therefore, cobalt oxide is a p-type material. Particle size and the characteristics of  $\text{Co}_3\text{O}_4$  are exceptionally strongly related to each other. The synthesis of  $\text{Co}_3\text{O}_4$  can be obtained in methods such as electrochemical oxidation, chemical vapor deposition (CVD), hydrothermal, sol-gel, precipitation, and microwave treatment. It is worth mentioning that properties such as particle size, shape, and degree of crystallinity are directly related to the synthesis method. However, preparing nanocrystalline  $\text{Co}_3\text{O}_4$  is sometimes difficult and complex [60]. Therefore, the precipitation of salts is one of the most prevalent methods for cobalt oxide synthesizing. Figure 2.7 represents the cobalt steps' basic synthesizing process using precipitation.

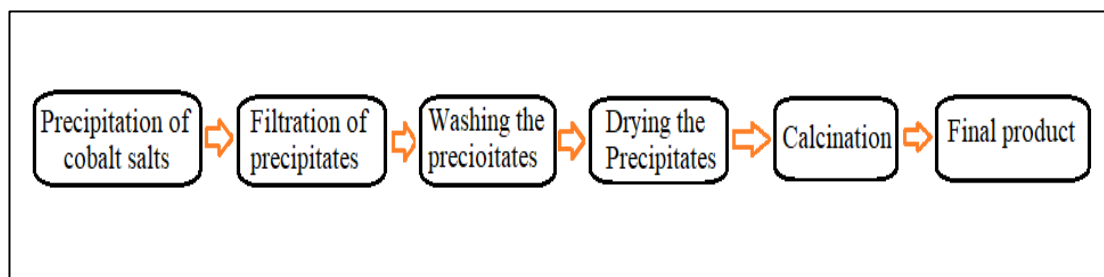


Figure 2.6: Basic synthesizing process of cobalt steps using the precipitation method

The sol-gel process is one of the most promising methods for synthesizing cobalt oxide. This process can be carried out under ideal conditions in terms of the efficacy of manipulating the product's properties, energy costs, and production process. The possibility of changing the conditions of the process (temperature, pH, the ratio of components, their concentration, aging time, etc.) allows for controlling the phase composition, size, and shape of the forming particles in a wide range. This method is quite effective for obtaining highly dispersed powders. However, currently, there is a

lack of information in the published articles on cobalt oxide synthesizing using the sol-gel method. The sol-gel process, in most cases, is based on the creation of joint complex compounds of cobalt with organic molecules and organic ingredients; most often, citric acid is used (citrate method). The formation of a complex leads to the production of a sol as a product of the reaction. After being synthesized, the sol is converted into a gel, which is then calcined to produce the final product and remove any organic compounds. Propionic and lauric acids are sometimes used in place of citric acid [60, 61].

## 2.5 Sol-gel process

Sol-gel is also an of the most successful chemical methods of synthesizing thin films and nanostructured materials. The sol-gel method has been intensively studied since the mid-1940s; however, it was not widely developed until the end of the 20th century[62]. Usually, this process involves the transformation of the precursor solution into an inorganic solid “sol.” Various forms, such as thin films, fibers, and powders, can be made with the sol process. The sequence and number of stages of the process and the methodology are determined by the purpose of the material being synthesized. For instance, different drying conditions make it possible to obtain both dense xerogel-based and highly porous aerogel-based materials [63].

The wide application of sol-gel synthesis in science and technology is due to many advantages of this method compared to the traditional way of synthesis materials. The main advantages of the sol-gel method are the high degree of homogeneity in a multicomponent system, the ability to control the particle size and pore structure, stoichiometric composition, and the possibility of obtaining non-crystalline systems [64]. Moreover, the sol-gel method's most significant advantage is its mechanical properties, allowing it to obtain fibers, needles, films, and composites deposited on a substrate [65].

Generally, the sol-gel method is a set of stages, including the preparation of a precursor solution, conversion into a sol, and then into a gel due to hydrolysis and condensation processes, subsequently aging, drying, and finally, the calcination of the final product. However, recently in the literature, sols have been divided into colloidal (particles form the solid dispersed phase) and polymeric (formed based on branched

macromolecules) [66]. Figure 3 shows a diagram illustrating the evolution of the material structure at various stages of the sol-gel synthesis [67]. In the first stage, the formation of separate colloidal solid nuclei with a size exceeding the critical in the solution occurs. For the formation of separate solid colloidal nuclei, the solution must be a supersaturated component, i.e., its concentration exceeded the solubility limit. After forming particle nuclei in the solution, the growth occurs by dissolving smaller particles with higher surface energy. This stage determines the morphology and phase composition of the final products [68]. In the sol formation, the size distribution of particles is determined by the duration of nucleation. As a rule, the size of crystals increases with increasing reaction time and temperature. However, particle growth processes can be controlled by changing the chemical composition and pH of the solution and introducing special chemical additives [69].

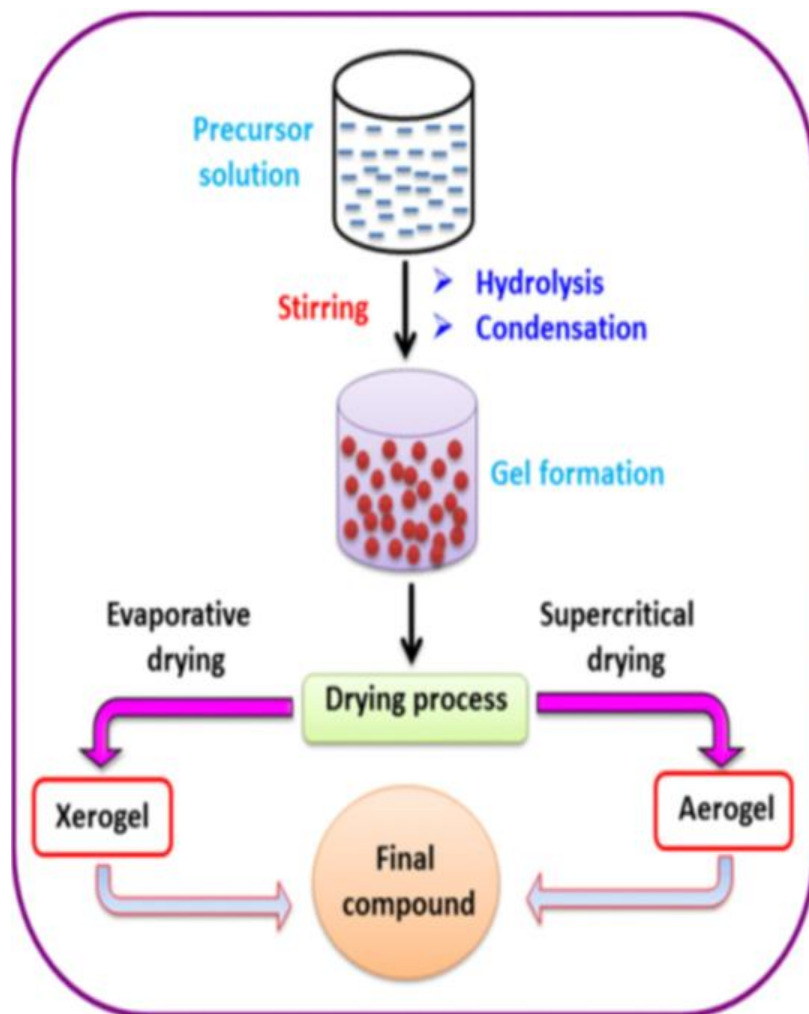


Figure 2.7: Sol-gel preparation steps.

In many cases, adding several modifying components to the composition is necessary to obtain a homogeneous and stable film-forming solution [70]. These components may have different functional purposes. Thus, the additional solvents reduce the volume concentration of particles, slowing down the aggregation processes and increasing the gel formation time. In addition, surfactants contribute to stabilizing the colloidal solution by being adsorbed on the surface of the formed nanoparticles.

The second stage is the formation of the gel from a colloidal solution and is by destabilization, and usually is carried out by changing the pH of the colloidal solution. During the formation of the gel, colloidal particles join together, and the solution loses fluidity [71]. The duration of the transformation from sol to gel is determined by the conditions of the process and can range from a few seconds to months.

The third stage is the drying gels stage to remove the liquid that fills the space between the particles. At this stage, the initially mechanically fragile raw gel undergoes enormous shrinkage and acquires a solid state [72]. The drying of the gel is the most crucial stage in synthesizing monolithic materials, enormous stresses arise in the drying of monolithic gel, and cracking and destruction of monolithic samples occur. As a result of intensive research, theoretical models and practical technological methods have been created and developed to describe the evolution of a monolithic gel during drying and produce a defect-free monolithic sample [73]. Adding drying control chemical additives (DCCA) helps reduce the gel structure stress during drying, thereby protecting it from cracking and ensuring the integrity of products. Some organic amines and amides (formamide, dimethylformamide, and others) are often used as DCCAs [74]. During the heat treatment of the dried material, the complete thermal decomposition of DCCA and the removal of gaseous residues occurs.

The final stage is the calcination of dried gel to remove the residual organic components and strengthen the material's structure. The dried gels are usually calcined with a slow increase in temperature to avoid cracking of the sol-gel material.

It is possible to achieve a reduction in energy consumption and a high degree of purity of products at all synthesis stages with a minimum cost and obtain a single-phase crystal structure with a high degree of perfection, strictly stoichiometric composition, and the absence of impurity phases [75].



The sol-gel is the basis of the latest nano technologies for producing light mixing rods, ceramic ultrafiltration membranes, optical and anticorrosive coatings, photographic materials, fine abrasives, and other materials with unique properties and a controlled structure [76].

# Chapter 3

## Experimental

### 3.1 Materials

Polyester resins were supplied by Verpol Boya and used as a matrix in this study to fabricate composite samples. Sigma Aldrich supplied Iron (III) nitrate nonahydrate  $\text{Fe}(\text{NO}_3)_3 \cdot 9\text{H}_2\text{O}$ , barium nitride  $\text{Ba}_3\text{N}_2$ , and ethylene glycol. Copper (II) sulfate pentahydrate  $\text{CuSO}_4 \cdot 5\text{H}_2\text{O}$ , starch, ascorbic acid, citric acid, sodium hydroxide NaOH and cobalt (II) nitrate hexahydrate  $\text{Co}(\text{NO}_3)_2 \cdot 6\text{H}_2\text{O}$  were ordered from Feta Educational Tools Center (Edulab). All chemicals have been used directly at analytical reagent grade without further purification.

### 3.2 Production of fillers

#### 3.2.1 Barium hexaferrite powders $\text{BaFe}_{12}\text{O}_{19}$

Barium hexaferrite powders were synthesized by the sol-gel method described in section 2.5. Iron nitride, Barium nitride, and citric acid were starting materials. First, an appropriate amount of Iron(III) nitrate nonahydrate  $\text{Fe}(\text{NO}_3)_3 \cdot 9\text{H}_2\text{O}$  and barium nitride  $\text{Ba}_3\text{N}_2$  in a molar ratio of 12 were dissolved in deionized water to get a clear solution. Then citric acid was added to the prepared aqueous solution and stirred for 30 minutes. Next, the solution evaporated to dryness by heating at 80 °C on a hot plate with continuous stirring. The solution was turned into a sticky liquid, forming a gel after evaporation of the water. Next, the gel was held in an oven at 200 °C for 12 h. Finally, the dried gel was calcined at 850 °C for 1 hour. The calcination temperature was estimated from TG-DTA analysis of the dried gel. Figure 3.1 shows the syncretization steps of barium hexaferrite.



Figure 3.1: Synthesis steps of barium hexaferrite

### 3.2.2 Copper-copper oxide powder

The copper oxide powder was synthesized by the chemical reduction method using copper (II) sulfate pentahydrate and starch as starting materials. The preparation process started with adding copper (II) sulfate pentahydrate solution into an appropriate amount of starch (1.2 %) solution with vigorous stirring for 30 min, and the color of the solution changed to pale blue, as shown in Figure 3.2 a. In the second step, a small amount of ascorbic acid solution was added to the synthesis solution under continuous rapid stirring. Subsequently, sodium hydroxide solution was slowly added to the prepared solution to promote the rate of the reduction process with constant stirring and heating at 80 °C for two hours (Figure 3.2b). After completion of the reaction, the precipitates were separated from the solution by filtration and washed with deionized water and ethanol to take out the excessive starch bound with the powder (Figure 3.2c). The synthesized copper oxide powder is shown in Figure 3.2d

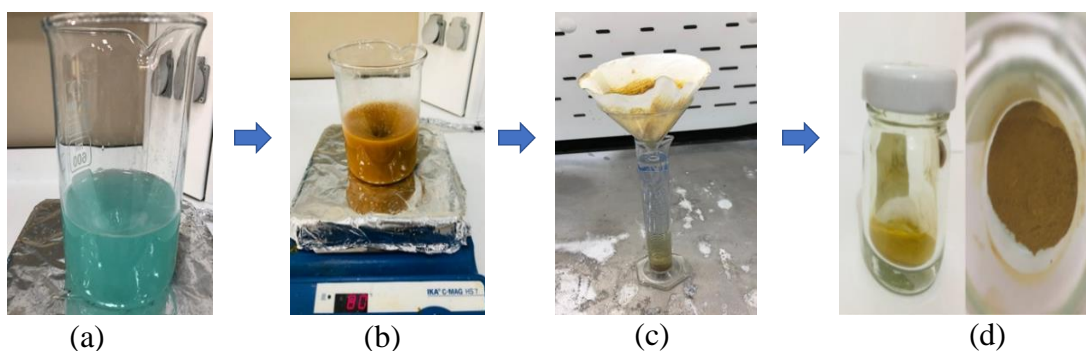


Figure 3.2: Synthesis steps of copper powder

### 3.2.3 Cobalt oxide

The cobalt oxide nanoparticles were synthesized by the sol-gel method. Cobalt (II) nitrate hexahydrate and ethylene glycol were precursor and solvent. The synthesis procedure was started by adding the cobalt (II) nitrate hexahydrate into the ethylene glycol dissolvent with a 1:3 ratio. The solution was then stirred vigorously for two hours until the complete dissolution of the solid at room temperature. Next, the solution was evaporated to dryness by heating at 90 °C on a hot plate with continuous stirring until the solution turned into a gel. Then the gel was held in an oven at 120 °C for 4 hours. The dried gel was calcined at 700 °C for one hour. The cobalt oxide powder after calcination is shown in Figure 3.3



Figure 3.3: Synthesized cobalt oxide powder

## 3.3 Preparation of composite Samples

The proposed RAMs in this study are based on three-layered material, with each layer consisting of polyester-based composite material reinforced powders. The design is similar to a sandwich structure with two layers and a layer between them. For instance, the first sample consists of two layers of  $\text{BaFe}_{12}\text{O}_{19}$  and a layer of  $\text{Co}_3\text{O}_4$  between them, and the second one consists of two layers of  $\text{Co}_3\text{O}_4$  and a layer of  $\text{BaFe}_{12}\text{O}_{19}$  between them. Similarly, the procedure continued for other samples.

Improving absorption by increasing the thickness of structures is not always an acceptable solution. Therefore, the thickness of each layer is kept at 1.5 mm; thus, the total thickness of the samples is 4.5 mm. However, composites were developed with weight fractions (filler wt/polyester wt) of 50%, 25%, 15%, 10%, and 5%.

The manufacturing process started with polyester resin blended with each filler, barium hexaferrite, cobalt oxide, and copper-copper oxide separately at the required proportion in glass beakers using a mechanical stirrer for 2 to 3 minutes to get a homogeneous slurry. However, preparing one layer over the other was necessary to obtain a good interface between the layers. Therefore, the fabrication sequence is as follows: the first layer was placed in the mold, and after a complete hardening of the first layer, the second layer was applied, and finally, the third layer, the preparation step, is shown in Figure 3.4. The prepared samples were coded as RA1, RA2, RA3, RA4, RA5, RA6, and RA7 (Figure 3.5). The structure design and thickness of the layers are summarized in Table 3.1.

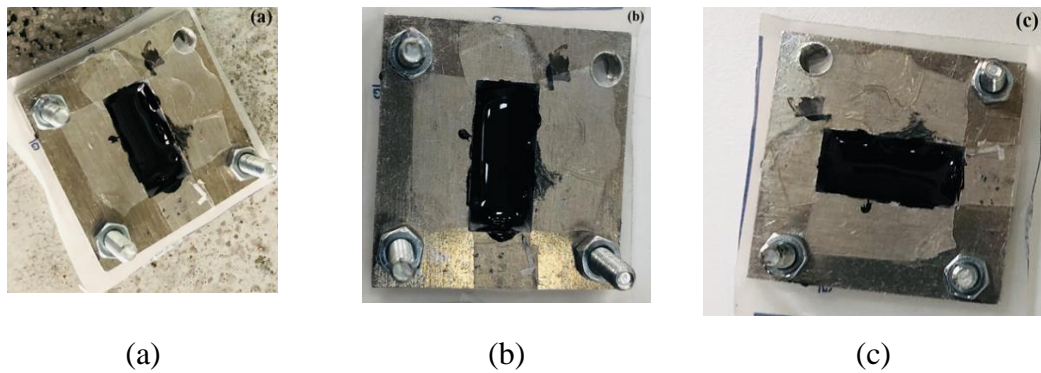


Figure 3.4: RAM's preparation steps after placing; a) the first layer, b) the second layer, and c) the third layer

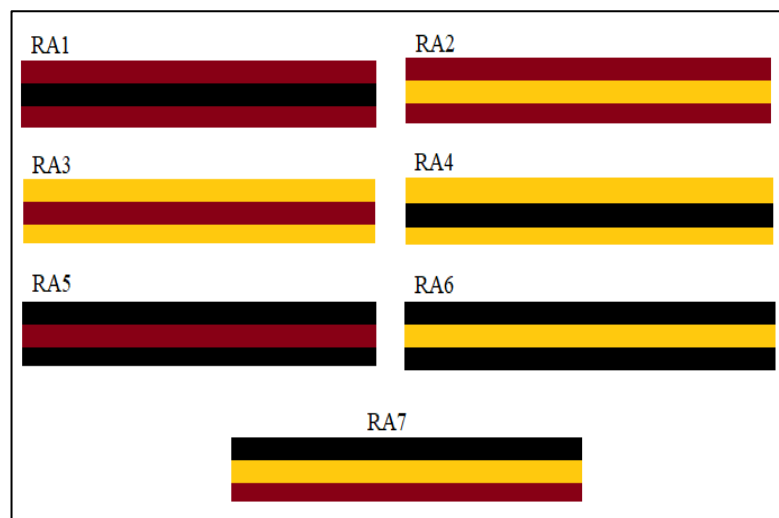


Figure 3.5: RAM samples

Table 3.1: Design and composition and layer thickness of composites

Code	Structure design			Thickness (mm)
	1 <sup>st</sup> layer	2 <sup>nd</sup> layer	3 <sup>rd</sup> layer	
RA1	5% BaFe <sub>12</sub> O <sub>19</sub>	5% Co <sub>3</sub> O <sub>4</sub>	5% BaFe <sub>12</sub> O <sub>19</sub>	4.5
	10% BaFe <sub>12</sub> O <sub>19</sub>	10% Co <sub>3</sub> O <sub>4</sub>	10% BaFe <sub>12</sub> O <sub>19</sub>	4.5
	15% BaFe <sub>12</sub> O <sub>19</sub>	15% Co <sub>3</sub> O <sub>4</sub>	15% BaFe <sub>12</sub> O <sub>19</sub>	4.5
	25% BaFe <sub>12</sub> O <sub>19</sub>	25% Co <sub>3</sub> O <sub>4</sub>	25% BaFe <sub>12</sub> O <sub>19</sub>	4.5
	50% BaFe <sub>12</sub> O <sub>19</sub>	50% Co <sub>3</sub> O <sub>4</sub>	50% BaFe <sub>12</sub> O <sub>19</sub>	4.5
RA2	5% BaFe <sub>12</sub> O <sub>19</sub>	5% Cu <sub>2</sub> -Cu	5% BaFe <sub>12</sub> O <sub>19</sub>	4.5
	10% BaFe <sub>12</sub> O <sub>19</sub>	10% Cu <sub>2</sub> -Cu	10% BaFe <sub>12</sub> O <sub>19</sub>	4.5
	15% BaFe <sub>12</sub> O <sub>19</sub>	15% Cu <sub>2</sub> -Cu	15% BaFe <sub>12</sub> O <sub>19</sub>	4.5
	25% BaFe <sub>12</sub> O <sub>19</sub>	25% Cu <sub>2</sub> -Cu	25% BaFe <sub>12</sub> O <sub>19</sub>	4.5
	50% BaFe <sub>12</sub> O <sub>19</sub>	50% Cu <sub>2</sub> -Cu	50% BaFe <sub>12</sub> O <sub>19</sub>	4.5
RA3	5% Cu <sub>2</sub> -Cu	5% BaFe <sub>12</sub> O <sub>19</sub>	5% Cu <sub>2</sub> -Cu	4.5
	10% Cu <sub>2</sub> -Cu	10% BaFe <sub>12</sub> O <sub>19</sub>	10% Cu <sub>2</sub> -Cu	4.5
	15% Cu <sub>2</sub> -Cu	15% BaFe <sub>12</sub> O <sub>19</sub>	15% Cu <sub>2</sub> -Cu	4.5
	25% Cu <sub>2</sub> -Cu	25% BaFe <sub>12</sub> O <sub>19</sub>	25% Cu <sub>2</sub> -Cu	4.5
	50% Cu <sub>2</sub> -Cu	50% BaFe <sub>12</sub> O <sub>19</sub>	50% Cu <sub>2</sub> -Cu	4.5
RA4	5% Cu <sub>2</sub> -Cu	5% Co <sub>3</sub> O <sub>2</sub>	5% Cu <sub>2</sub> -Cu	4.5
	10% Cu <sub>2</sub> -Cu	10% Co <sub>3</sub> O <sub>4</sub>	10% Cu <sub>2</sub> -Cu	4.5
	15% Cu <sub>2</sub> -Cu	15% Co <sub>3</sub> O <sub>4</sub>	15% Cu <sub>2</sub> -Cu	4.5
	25% Cu <sub>2</sub> -Cu	25% Co <sub>3</sub> O <sub>4</sub>	25% Cu <sub>2</sub> -Cu	4.5
	50% Cu <sub>2</sub> -Cu	50% Co <sub>3</sub> O <sub>4</sub>	50% Cu <sub>2</sub> -Cu	4.5
RA5	5% Co <sub>3</sub> O <sub>2</sub>	5% Cu <sub>2</sub> -Cu	5% Co <sub>3</sub> O <sub>4</sub>	4.5
	10% Co <sub>3</sub> O <sub>2</sub>	10% Cu <sub>2</sub> -Cu	10% Co <sub>3</sub> O <sub>4</sub>	4.5
	15% Co <sub>3</sub> O <sub>2</sub>	15% Cu <sub>2</sub> -Cu	15% Co <sub>3</sub> O <sub>4</sub>	4.5
	25% Co <sub>3</sub> O <sub>2</sub>	25% Cu <sub>2</sub> -Cu	25% Co <sub>3</sub> O <sub>4</sub>	4.5

	50% $\text{Co}_3\text{O}_2$	50% $\text{Cu}_2\text{-Cu}$	50% $\text{Co}_3\text{O}_4$	4.5
RA6	5% $\text{Co}_3\text{O}_2$	5% $\text{BaFe}_{12}\text{O}_{19}$	5% $\text{Co}_3\text{O}_4$	4.5
	10% $\text{Co}_3\text{O}_2$	10% $\text{BaFe}_{12}\text{O}_{19}$	10% $\text{Co}_3\text{O}_4$	4.5
	15% $\text{Co}_3\text{O}_2$	15% $\text{BaFe}_{12}\text{O}_{19}$	15% $\text{Co}_3\text{O}_4$	4.5
	25% $\text{Co}_3\text{O}_2$	25% $\text{BaFe}_{12}\text{O}_{19}$	25% $\text{Co}_3\text{O}_4$	4.5
	50% $\text{Co}_3\text{O}_2$	50% $\text{BaFe}_{12}\text{O}_{19}$	50% $\text{Co}_3\text{O}_4$	4.5
RA7	50% $\text{Cu}_2\text{-Cu}$			4.5
	50% $\text{BaFe}_{12}\text{O}_{19}$			4.5
	50% $\text{Co}_3\text{O}_2$			4.5

---

## 3.4 Characterization

### 3.4.1 X-ray diffraction analysis

The phase composition of the samples was determined by X-ray diffraction (XRD) analysis using a Panalytical Empyrean X-ray diffractometer with Bragg-Brentano focusing (Figure 3.6), CoK $\alpha$ -radiation and graphite monochromatic on diffracted beam. X-ray spectra measured in the  $2\theta$  range of 5–90°. Qualitative phase analysis was performed using Xpert Highscore Plus software. X-ray analysis is a method for studying the structure of a substance by distribution in space and intensities of X-ray radiation scattered on the analyzed sample [77]. The technique is based on the interaction of X-rays with the electrons of matter, which results in X-ray diffraction [78]. The diffraction pattern depends on the wavelength of the X-rays used and the structure of the sample [79]. The source of X-rays is an X-ray tube with an anode made of metal, which gives the characteristic X-ray radiation of the K-series. Typically, an anode made of metals (Cr, Fe, Co, Ni, Cu, Mo) is used with characteristic radiation with wavelengths from 2.29 to 0.705 Å. In 1913, W. L. Bragg proposed an interpretation of the appearance of diffraction rays in a crystal [80]. Bragg showed that any of the diffractive rays could be considered as a reflection of the incident ray from one of the systems of crystallographic planes and developed an equation (3.1) that can

be considered as a basic equation underlying the method of X-ray phase analysis to explain how crystal faces appear to reflect X-rays at certain angles of incidence (Figure 3.7) [81].

$$n\lambda=2d\sin\theta \quad (3.1)$$

XRD analysis is performed by measuring the intensities of as many diffraction reflections as possible, which can be obtained from the crystal at a given radiation wavelength and all possible orientations of the sample. The diffraction pattern is recorded on photographic film in an x-ray goniometer [82]. Moreover, it is possible to directly measure the intensity of diffraction reflections using proportional, scintillation, and other X-ray counters [83]. X-ray goniometers take a series of X-ray patterns to have a complete set of reflections [84]. On each of them, diffraction reflections are recorded on the Miller indices. Miller indices of which certain restrictions are imposed are recorded on different X-ray patterns. Databases contain X-ray diffraction patterns of many compounds used as a "fingerprint" to identify the phases present in the sample [85].



Figure 3.6: Panalytical Empyrean X-ray diffractometer



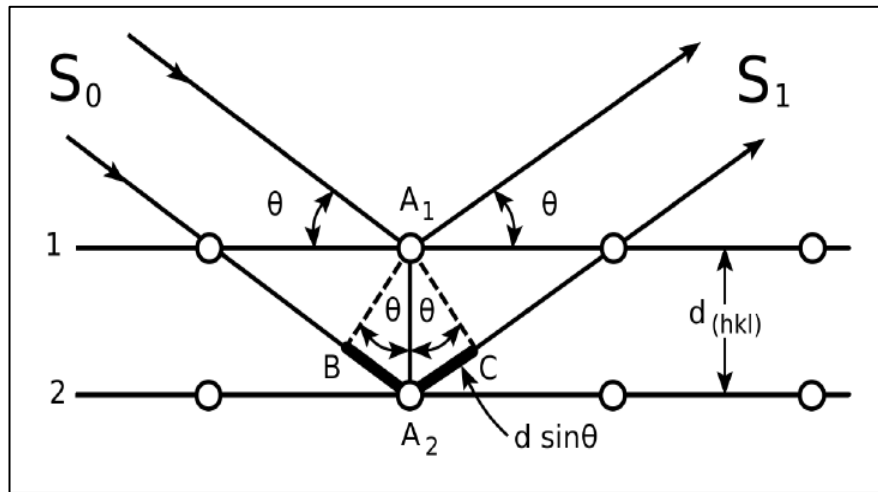


Figure 3.7: Bragg's equation of diffraction [86]

### 3.4.2 Scanning electron Microscopy

Scanning electron microscopy was used to characterize microstructures. The analysis was carried out using sigma 300VP from a Carl Zeiss scanning electron microscope coupled with smart X-ray energy dispersive microanalysis system with a nitrogen-free detector X-max 50 Standard, silicon drift-detecting element active area of 30 mm<sup>2</sup>, the resolution on the line Mn K $\alpha$  - 129 (Figure 3.8).

The electron microprobe analysis uses characteristic x-ray radiation resulting from the excitation of atoms by an electron beam (electron probe) [87]. This probe can be focused using electronic lenses, allowing the determination of the composition of micro-sites or the elements in the microstructure of an alloy [88]. The depth of penetration of the electron beam into the sample surface for precious metals at a voltage of 20 kV is about 0,1-0,3 micrometers [89]. The qualitative elemental composition of micro volumes is determined by comparing the observed wavelengths of the emitted radiation with standards incorporated in the analyzer. In addition, quantitative analysis was performed based on differences in intensity of the strongest lines of the K-L-series of the characteristic radiation of the element [90].



Figure 3.8: Sigma 300VP from Carl Zeiss scanning electron microscope

### 3.4.3 Particle Size Analysis

The Mastersizer Hydro 3000 (Figure 3.9) was used to measure the size of particles based on the Mie scattering theory. The mastersizer hydro uses the laser light diffraction method to determine the particle size distribution based on the analysis of the light scattering profile that occurs when a collimated laser beam illuminates a particle [91]. This method allows measuring particles from 0.1  $\mu\text{m}$  to 8.0 mm. The sample dispersed in a liquid or gas at the required concentration is exposed to laser irradiation. The interaction of the incident light beam and particles of the dispersed phase leads to a light scattering profile with different light intensities at different angles and is measured by a multi-element detector [92]. Numerical values representing the light scattering profile are recorded, and these values are mathematically converted using an optical model into fractions of the total volume of individual size classes, thus forming the volume distribution of particles by size [93].



Figure 3.9: Master Sizer Hydro 3000

### 3.4.4 Thermal analysis

Thermal analysis is a series of analytical techniques by which a material's physical and chemical properties are measured as a dynamic function of temperature [94]. The sample temperature or heating time is plotted along the abscissa, and the temperature-dependent quantity is plotted along the ordinate. The graph is called a thermogram. One of the methods of thermal analysis is thermogravimetric analysis (TGA), which makes it possible to obtain data on the change in the mass of a sample during uniform heating or cooling of the material under study, as well as during isothermal annealing at different temperatures [95]. In addition, differential scanning calorimetry (DSC) measures the differential heat flux and allows you to obtain qualitative and quantitative data on exothermic and endothermic processes. The combination of these methods makes it possible to determine the mass fractions of adsorbed, thermal stability, oxidizable substances, the characteristics of phase transitions, thermal effects, and other parameters [96].

In this work, the determine the phase formation temperature, barium hexaferrite, and cobalt oxide samples were subjected to complex thermal analysis, thermogravimetry (TG), and differential scanning calorimetry using a DSC-TGA thermal analyzer TA SDT Q600 (Figure 3.10) was carried out in an argon medium. The heating rate was 10°C/min. from room temperature to 950°C.



Figure 3.10: TA SDT Q600 Thermal analysis

### 3.4.5 Vibrating Sample Magnetometer (VSM)

A Vibrating Sample Magnetometer (VSM) was used to measure the magnetic properties of the materials. At room temperature, magnetic properties were measured using Dexion Magnet VSM 550 (Figure 3.11). The vibrating magnetometer is a device that has a high level of sensitivity and can determine the magnetic properties of a wide variety of magnetic materials [97]. These magnetic materials include paramagnets, magnetic powders, thin films, soft magnetic materials, permanent magnet materials, and high-temperature superconductors. When the sample starts to vibrate, a magnetic field generates around it, and the field can be analyzed as it changes with time [98].



Figure 3.11: Dexion Magnet VSM 550

The degree of magnetization is determined by software, which uses the magnetizing force, the rate of vibration of the sample, data from the probe that measures the

sample's magnetism, and the value of the magnetic field resulting from the vibration [99]. The software then converts the changes in the signal into a graph of induced magnetic flux density values versus magnetic field strength, referred to as a hysteresis loop (Figure 3.12) [100]. Hysteresis loops provide many essential values, such as Saturation magnetization ( $M_s$ ), remanent magnetization ( $M_r$ ), and coercivity ( $H_c$ ) which is the field at which the sign of the magnetization change occurs.

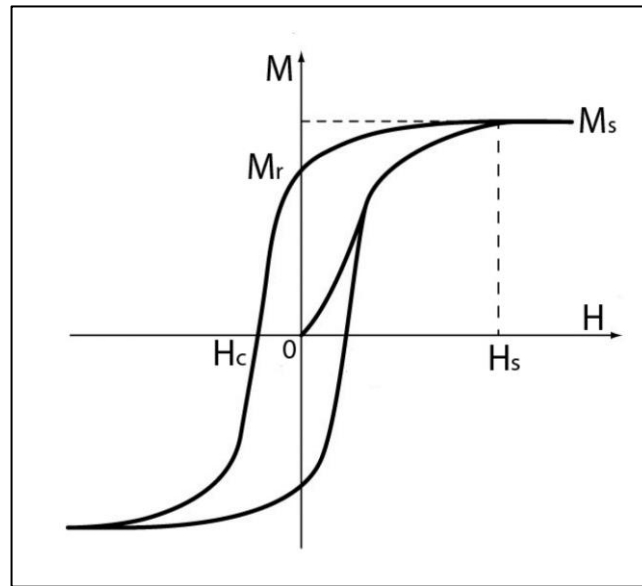


Figure 3.12: Schematic showing a typical magnetic hysteresis loop

### 3.4.6 Microwave Network Analyzer

Microwave Network Analyzer was used to measure the microwave properties of the materials. The measurement of magnetic properties was carried out by Agilent Technologies / PNA-L – N5230C 550 (Figure 3.13) at room temperature. A Vector network analyzer is a device to measure the absorption and reflection of microwaves from various materials, such as structural elements of aircraft or missiles, special coatings, and paints, and also measures the characteristics of active and passive radio devices, such as attenuators, amplifiers, filters, antennas, feeders, waveguides, frequency converters and many other components used in various circuits [101]. The vector network analyzer measures the transmission characteristics of a signal through a sample being tested and the reflection characteristics of a signal from its ports [102]. These characteristics are called S-parameters. For two-port vector network analyzer devices, the first port's reflection is called  $S_{11}$ , the forward transmission is called  $S_{21}$ ,

the reverse transmission is called  $S_{12}$ , and the second port's reflection is called  $S_{22}$  (Figure 3.14). Each S-parameter contains the amplitude-frequency (AFC) and phase-frequency (PFC) characteristics of the sample being tested in the corresponding directions. Parameters measured with a VNA can be shown in many ways, including SWR or return loss, Smith charts, amplitude, and phase [103]. The network analyzer applies a sinusoidal signal to the tested sample and measures the signal that is reflected and transmitted through the sample [104]. The amplitude and phase of both reflected and transmitted signals will differ from the applied sinusoidal signal. A network analyzer is called a network analyzer when it only measures amplitude and a vector when it measures both amplitude and phase [105]. Almost all current network analyzers are vector because vector analyzers provide the most comprehensive measurements of the sample being tested within a particular frequency range [106].



Figure 3.13: Agilent Technologies / PNA-L – N5230C

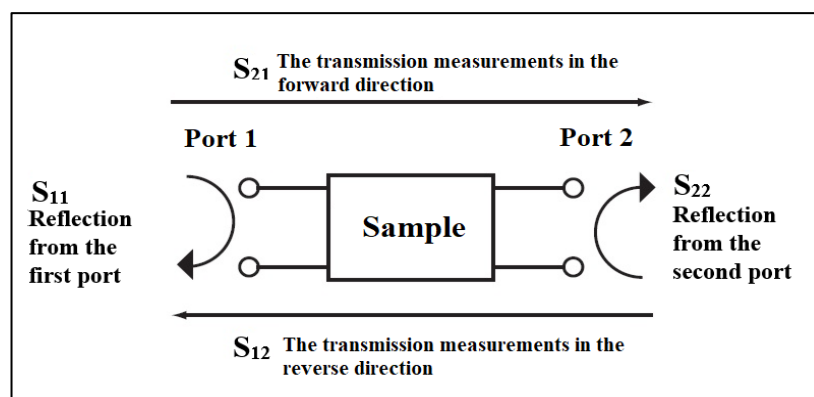


Figure 3.14: S-parameters [107]

A simplified illustration of the VNA's operation in forward transmission mode can be seen in Figure 3.15. A sinusoidal signal with a specified amplitude and phase is applied to the tested sample. The amplitude and phase of the signal will change after it has passed through the sample being tested. The amplitude and phase detector also indicates how much the measured signal differs from the reference one. As a result, the samples' properties can be determined at a single frequency [108]. The VNA adjusts the frequency of the reference signal repeatedly within the specified limits over a range of frequencies measurement

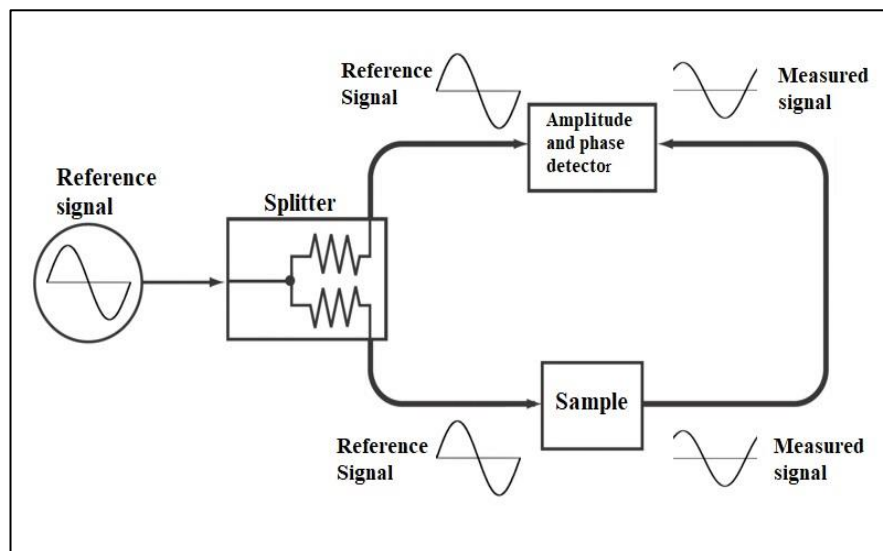


Figure 3.15: Simplified diagram of a vector network analyzer in forward transmission mode S1 [109]

# Chapter 4

## Results and discussion

### 4.1 Phase analysis

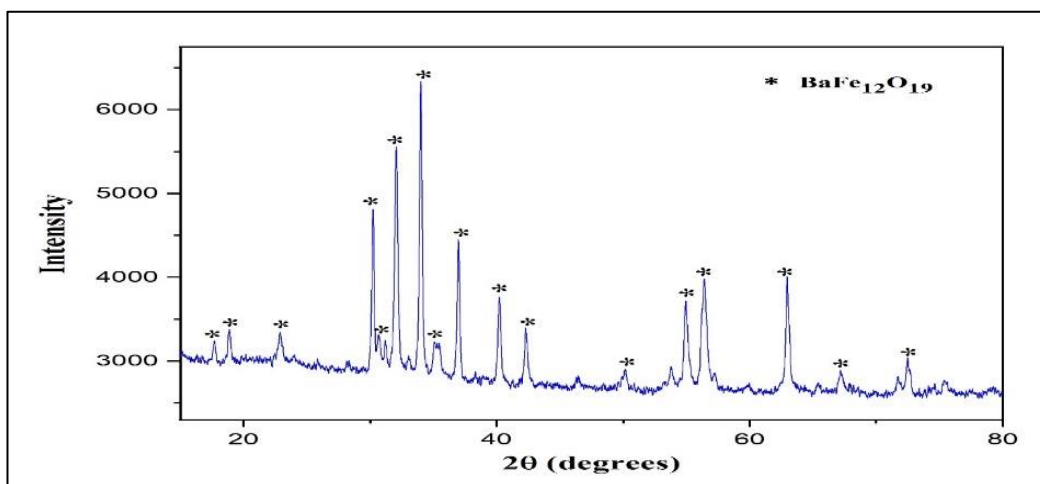
X-ray diffraction (XRD) was conducted to identify phases in the material (Figure 4.1). XRD diffraction patterns for XRD patterns of the synthesized  $\text{BaFe}_{12}\text{O}_{19}$  powder can be seen in Figure 4.1a shows it is a single-phase product with only sharp diffraction peaks characteristic of crystalline material. All diffraction peaks are typical to the reference indexed as barium hexaferrite corresponding to JCPDS card no. 00-007-0276, and no impurity or other phases were detected. Therefore, this result is in good agreement with the reported in the previous studies [110,111,112].

Figure 4.1b shows the XRD pattern of synthesized cobalt oxide  $\text{Co}_3\text{O}_4$ . The XRD pattern is compatible with the standard spectrum of  $\text{Co}_3\text{O}_4$  (JCPDS card no.00-042-1467), and no impurity-related peaks are detected, indicating that  $\text{Co}_3\text{O}_4$  is the dominant compound and pure  $\text{Co}_3\text{O}_4$  was successfully synthesized. Furthermore, it is in agreement with previous studies, which show that the low ratio between precursor and dissolvent leads to the formation of  $\text{Co}_3\text{O}_4$  occurred rather than  $\text{CoO}$  [113,114].

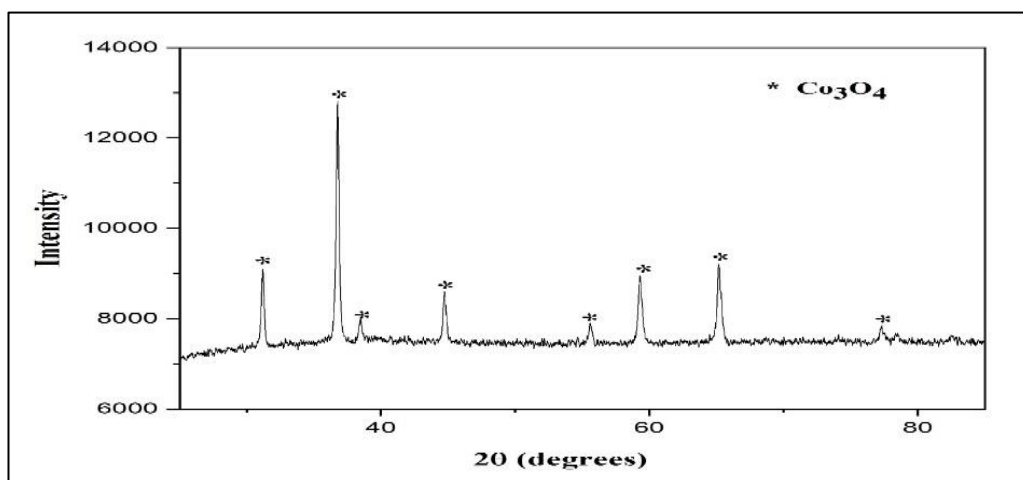
The XRD diffraction pattern showed the presence of two crystalline phases, metallic  $\text{Cu}$  and cuprous  $\text{Cu}_2\text{O}$  (Figure 4.1c), formed by the reaction of copper (II) sulfate pentahydrate complex with ascorbic acid and sodium hydroxide. XRD pattern revealed that copper powders formed the formation of copper due to electrolysis, and  $\text{Cu}^{3+}$  ions form metallic copper by exchanging electrons with neutral  $\text{H}$ .  $\text{Cu}_2\text{O}$ , on the other hand, is the oxidation of  $\text{Cu}^{3+}$  ions that exists in the environment and is not fully reduced, due to  $\text{NaOH}$  included in the system. It is also hypothesized that adding the sodium hydroxide causes the formation of  $\text{Cu}(\text{OH})_2$ , which subsequently produces the  $\text{Cu}_2\text{O}$



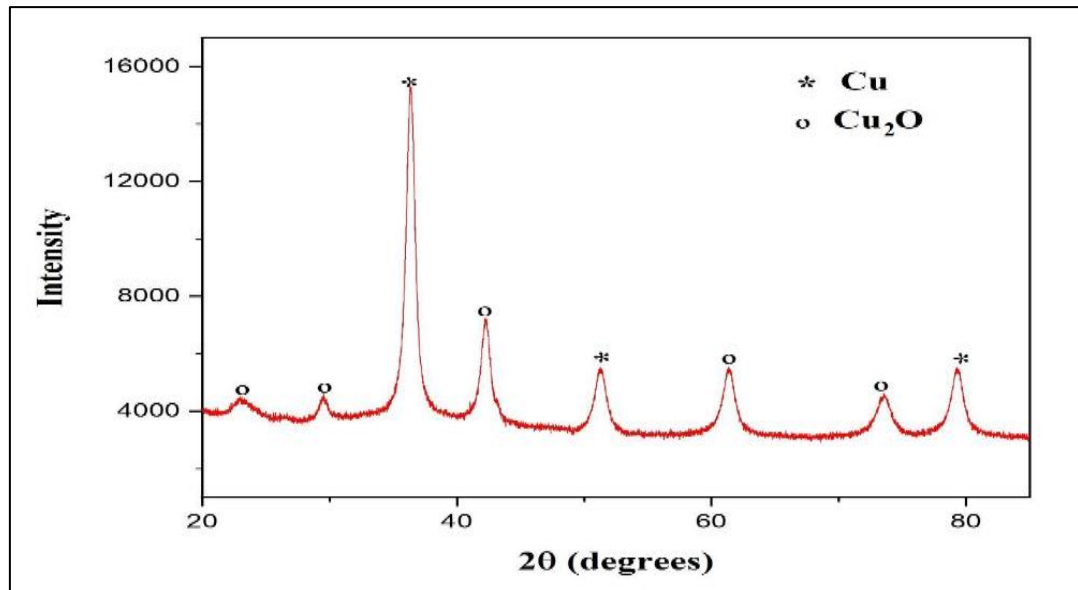
phase upon reduction. Therefore, it is reasonable to assume that it is extremely difficult to completely convert stable copper (II) sulfate pentahydrate to copper particles using ascorbic acid and sodium hydroxide, and only a combination of copper and copper oxide can be produced. This indicates that the copper phase will eventually transform into copper oxide if left in the air for much longer. Luna et al. [115] made a similar observation and also showed that Cu particles cannot be synthesized by reducing Cu ions with ascorbic acid in an aqueous media without inert gas protection. However, possible. All peaks of copper and cuprous oxide  $\text{Cu}_2\text{O}$  were observed, and no peak was attributable to potential impurities. Furthermore, as copper and copper oxide have an excellent absorbing properties in microwave frequencies, it was found that formed powder is an excellent alternative material.



(a)



(b)

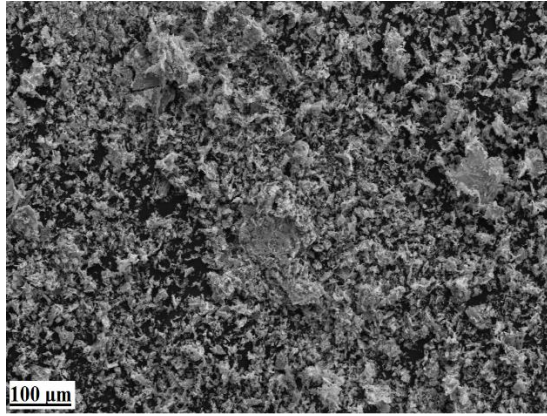


(c)

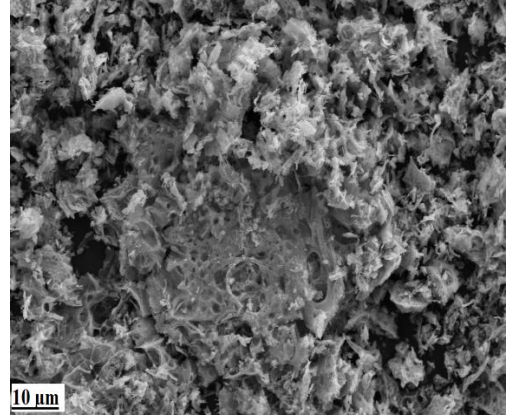
Figure 4.1: XRD pattern of a) barium hexaferrite, b) cobalt oxide, c) Cu and Cu<sub>2</sub>O

## 4.2 Scanning electron microscope

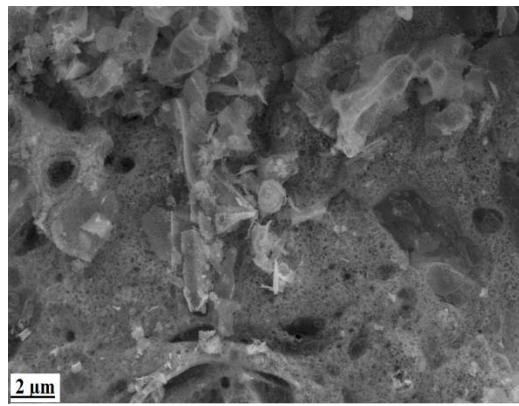
SEM micrographs provided reliable information about particle sizes and shapes. SEM images of the barium hexaferrite are shown in Figure 4.2. The micrographs were taken at magnifications of 250 x, 1.0 kx, and 5.0 kx. The SEM image show micro-size particles of barium hexaferrite of different sizes and shapes are distributed and agglomerated. According to Asiri et al. [116], the agglomerates are mainly due to magnetic dipole-dipole interaction between particles; moreover, a few large particles or agglomerates in a sample cannot undesirably impact the microwave absorption properties [104]. SEM images (Figure 4.3) of cobalt oxide show that the powder mainly consists of different shapes of particles with microparticles. All obtained Co<sub>3</sub>O<sub>4</sub> powders were hollow microspheres with a diameter of 0.5 to 10 μm. Generally, the synthesis method and chemical parameters significantly impact the powder's morphology. However, increasing the calcination temperature usually changes particle morphology in the sol-gel process. High temperatures can produce activation energies, increasing the growth rate and, therefore, grain size forming a bigger particle [117]. However, the morphology is quite similar to the one obtained by [118]. SEM images of copper oxide in Figure 4.4 demonstrates the dispersion of spherical-shaped particles or a shape close to spherical, almost with a wide particle size distribution. Also, synthesized powders are characterized by a tendency to form agglomerates.



(a)

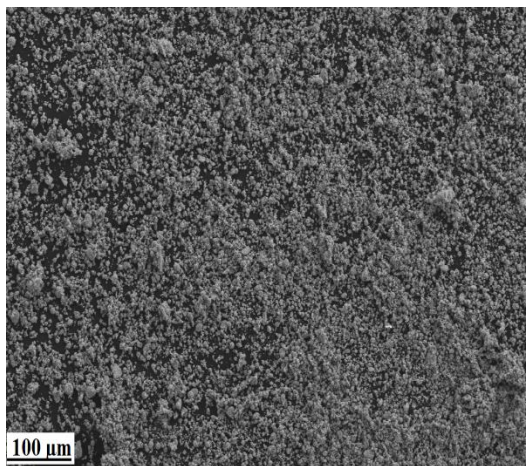


(b)

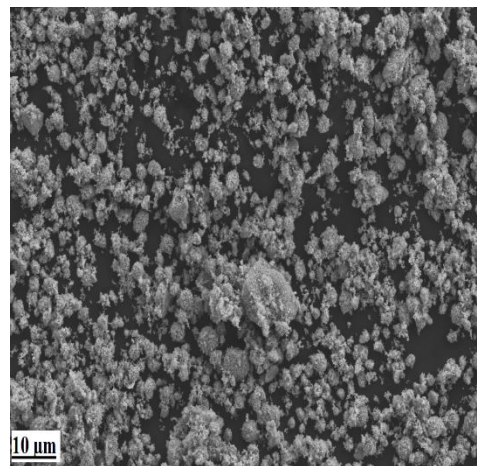


(b)

Figure 4.2: SEM images of barium hexaferrite (a) 250 x (b) 1.00 kx (c) 5 kx magnifications

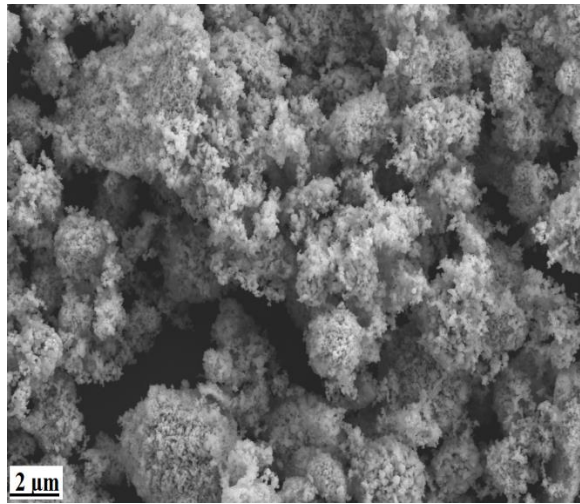


(a)



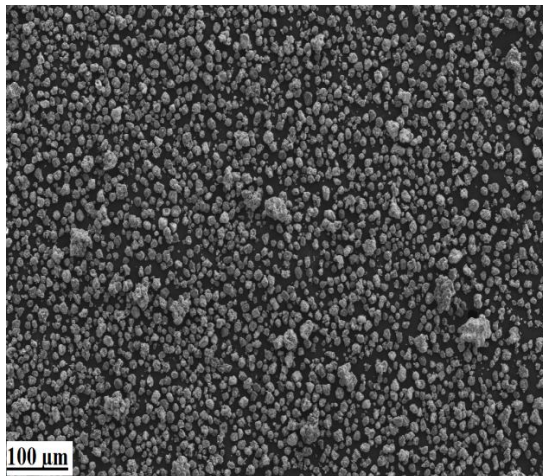
(b)



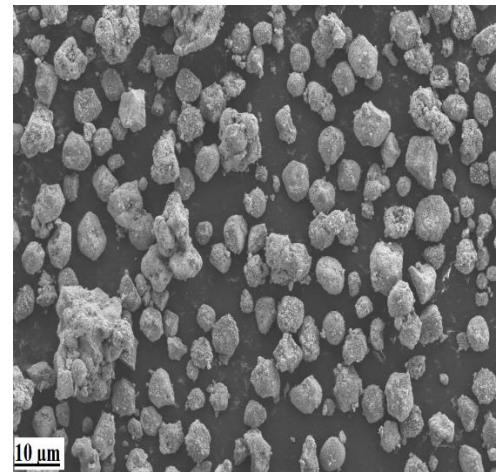


(c)

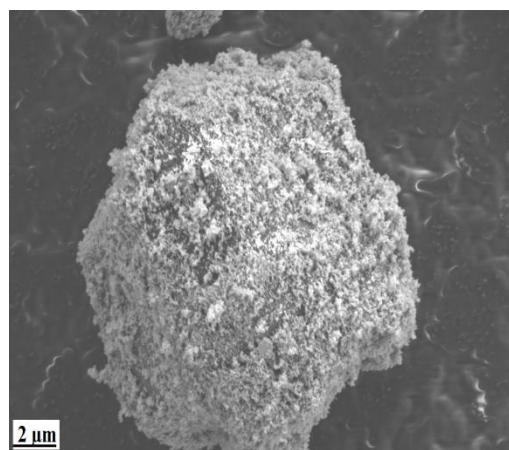
Figure 4.3: SEM images of cobalt oxide (a) 250 x (b) 1.00 kx (c) 5 kx magnification



(a)



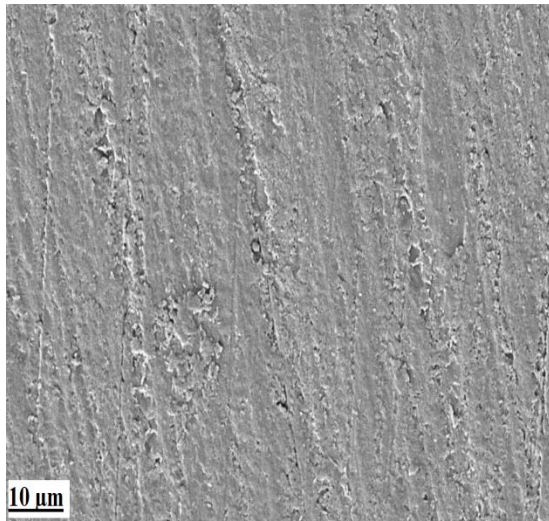
(b)



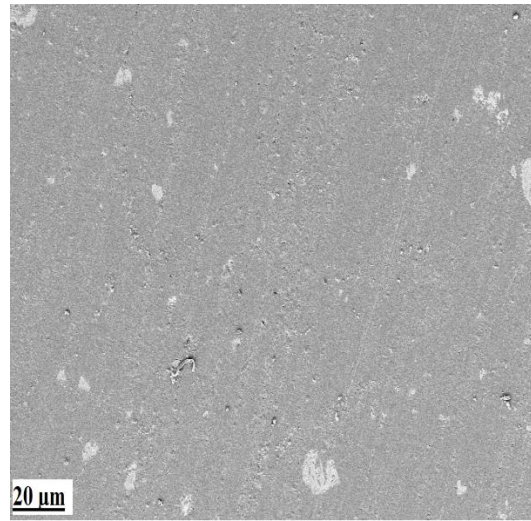
(c)

Figure 4.4: SEM images of copper-copper oxide (a) 250 x (b) 1.00 kx (c) 10 kx magnifications

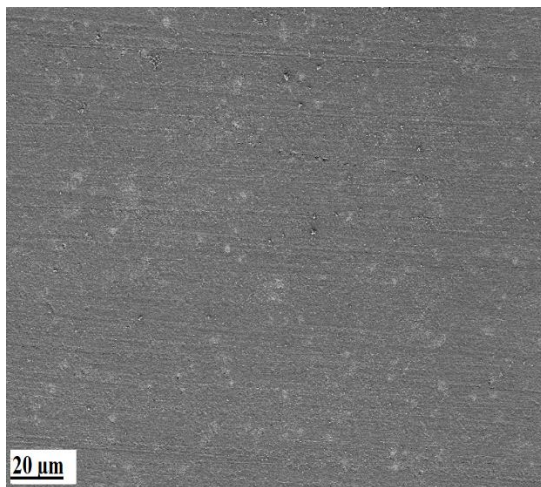
When mixing a powder filler with polystyrene, there are problems of uniform distribution of the filler, the particles of which are distributed in the polystyrene both in the form of individual particles and of agglomerates, which, in turn, leads to material inhomogeneity and affect the nonlinearity of radar absorbing characteristics. SEM images of composites are shown in Figure 4.5. It can assume that the reinforcement particles are well distributed in the composite throughout the entire matrix. The reinforcing powder must be distributed uniformly in the polyester matrix to achieve high absorbing characteristics because inhomogeneities contribute to the formation of micro defects in the composite, which significantly reduces strength and worsens absorbing ability since this class of materials is characterized by a higher radio absorption coefficient per unit weight.



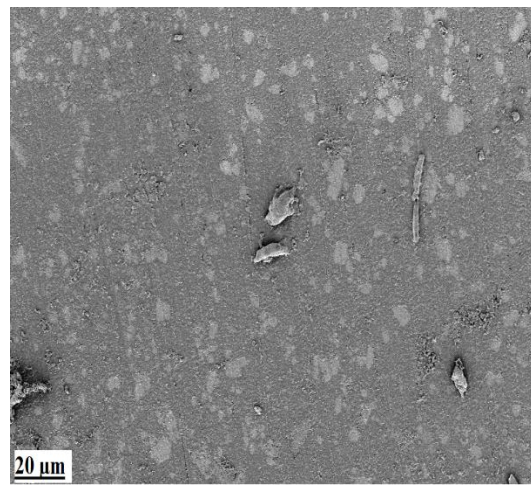
(a)



(b)



(c)



(d)



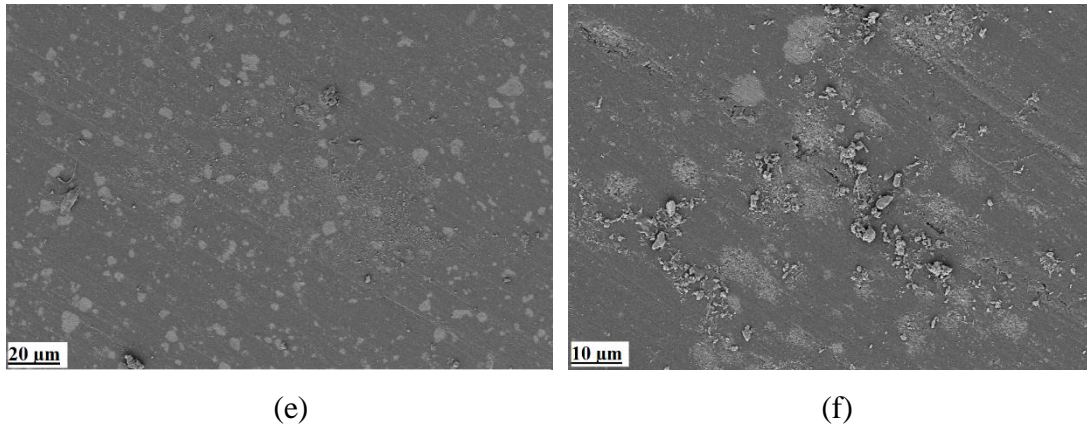


Figure 4. 5 SEM images of; a) RA2 5%, b) RA3 10%, c) RA4 10% ,d) RA5 25% , e) RA5 50% and f) RA6 25%

The cross-section SEM images of RA2 50%, RA4 25%, RA5 15%, and RA6 25% samples are shown in Figure 4.6. The cross-section SEM images showed flat interfaces between the layers, irregularities were practically not observed, and layers were well joined. However, preparing the composites one layer over the other is considered to be the reason for obtaining a good interface between the layers.

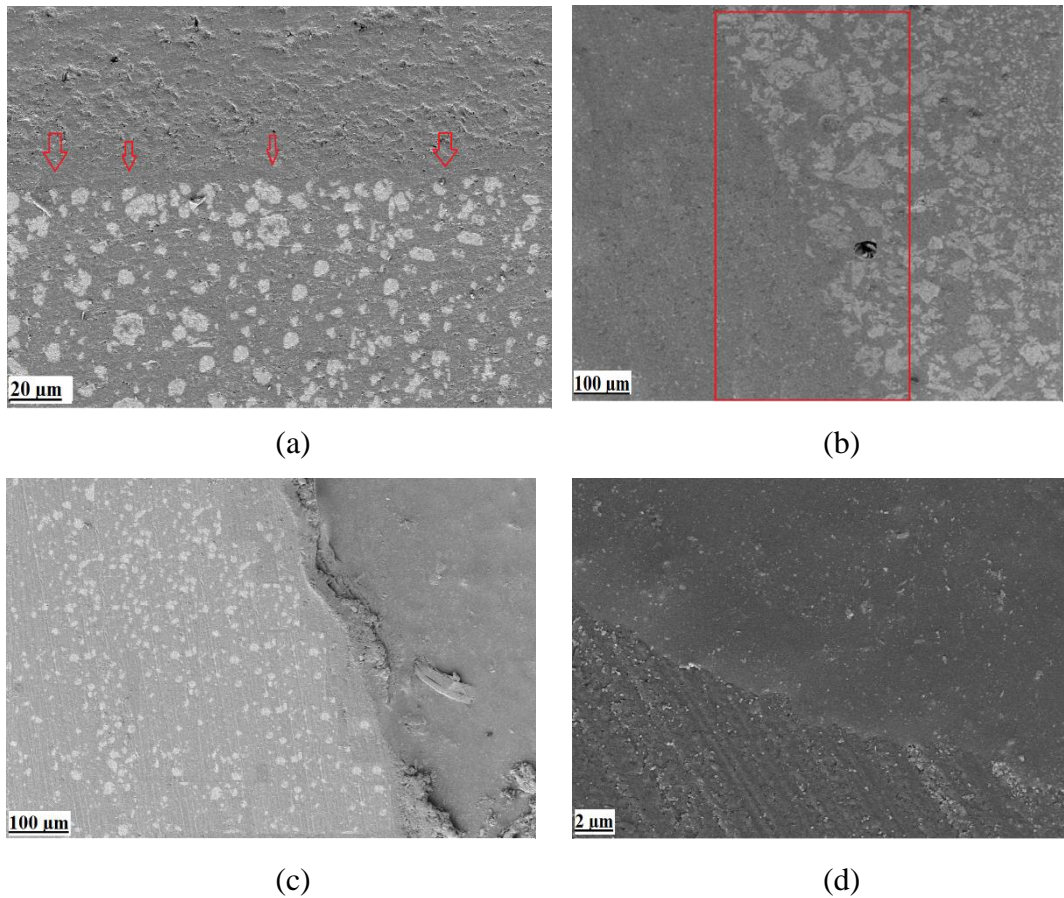
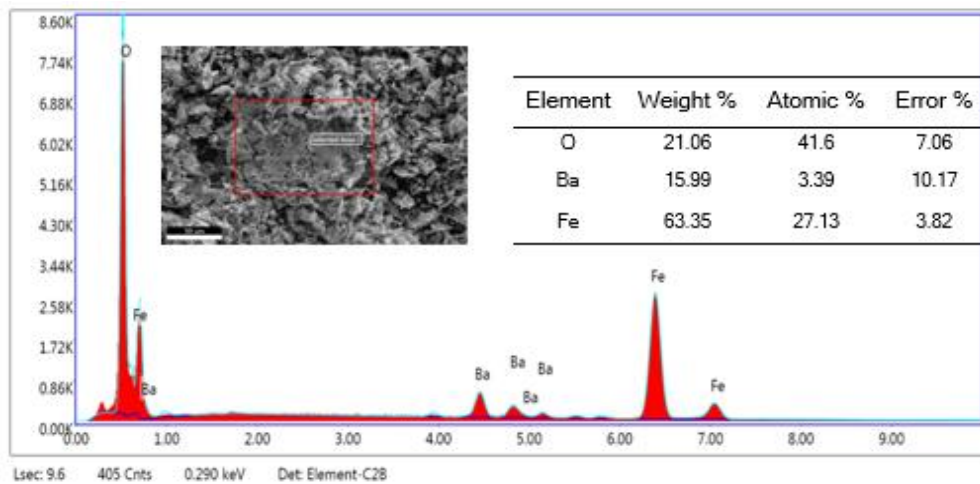


Figure 4.6: SEM image of a) RA5 50%, b) RA3 15%, c) RA1 25% and d) RA6 25% sample cross-section

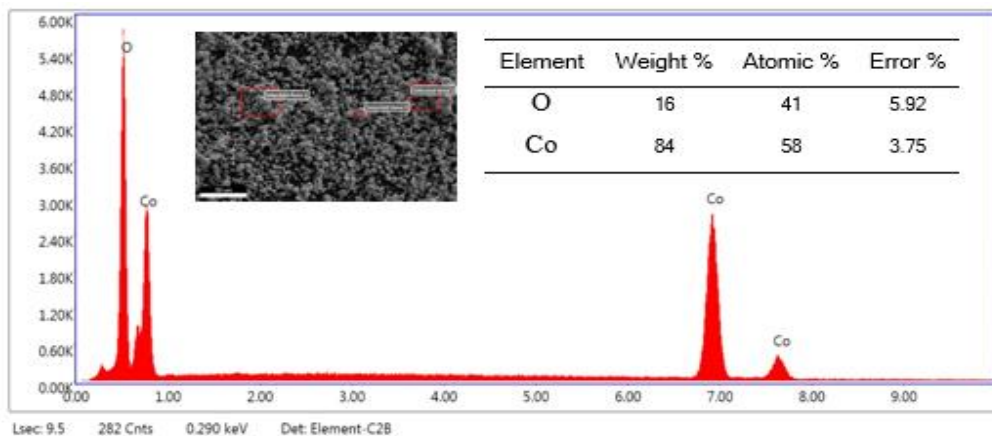
### 4.3 The energy dispersive X-ray (EDX)

The energy dispersive X-ray (EDX) analysis was conducted to confirm the elemental composition. (EDX) analysis of barium hexaferrite and the relative atomic and weight abundance of Ba, Fe, O, Ti, and C are presented in is shown in Figure 4.7a. The EDX spectrum confirms the presence of Ba, Fe, and O. EDX analysis of cobalt oxide and the relative atomic and weight abundance of Co, O is presented in Figure 4.7b. The EDX spectrum confirms the presence of only two elements, Co and O; no other elements were detected, confirming XRD results.

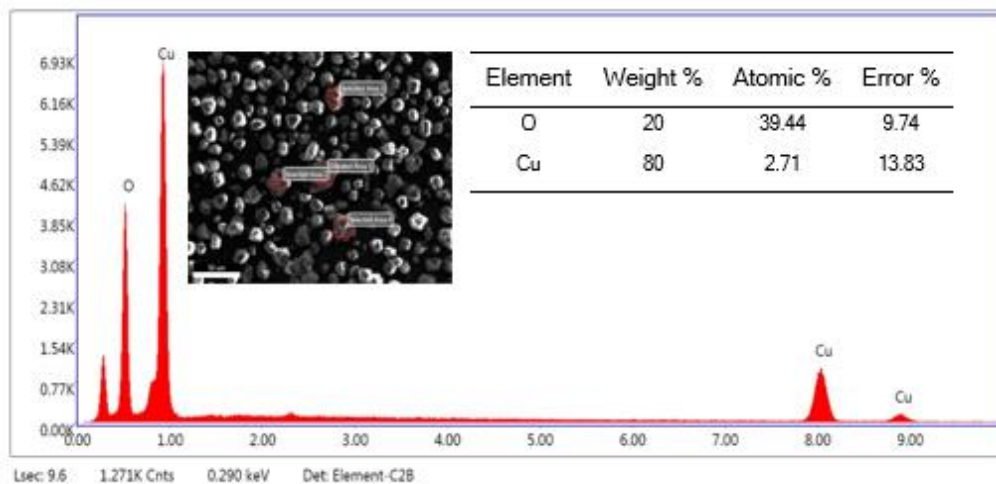
EDX analysis of Cu and Cu<sub>2</sub>O The relative atomic and weight abundance of Cu and O are presented in Figure 4.7c.



(a)



(b)



(c)

Figure 4.7: EDX spectrum of a) barium hexaferrite, b) cobalt oxide, c) Cu and Cu<sub>2</sub>O

## 4.4 Particle analysis

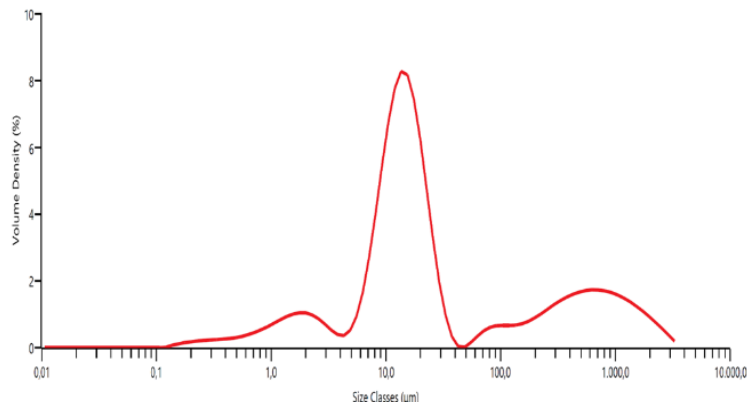
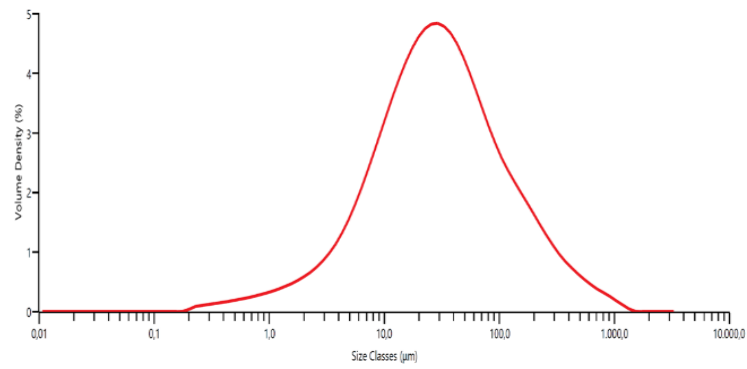
Figure 4.8a shows the particle distribution of barium hexaferrite. Average particle sizes of barium hexaferrite vary mainly in the range from 10 to 100  $\mu\text{m}$  the smallest fixed particles have a size of 10  $\mu\text{m}$ , and the largest was about 504  $\mu\text{m}$ . The average particle size is quite large compared to other works that used the same approach [110,119]. This could be attributed to the calcination temperature as the particle size highly depends on the calcination temperature and milling time which is pointed out by Junliang et al. [120].

Particle size distribution of cobalt oxide powder showed that 4.87% of particles have a size from 0.1 to 4  $\mu\text{m}$  and 76% from 4-40  $\mu\text{m}$  (Figure 4.8b). The large scatter is associated with the tendency for particle agglomeration during synthesis. The Sol-gel method is quite effective for obtaining highly dispersed powders. However, currently, there is a lack of information in the published articles on synthesizing cobalt oxide using the sol-gel method. Therefore, the observations in this study cannot be compared to the previous studies. However, Dippong et al. [121] suggested that the cobalt nitrate and ethylene glycol molar ratio is more likely to impact the particle size.

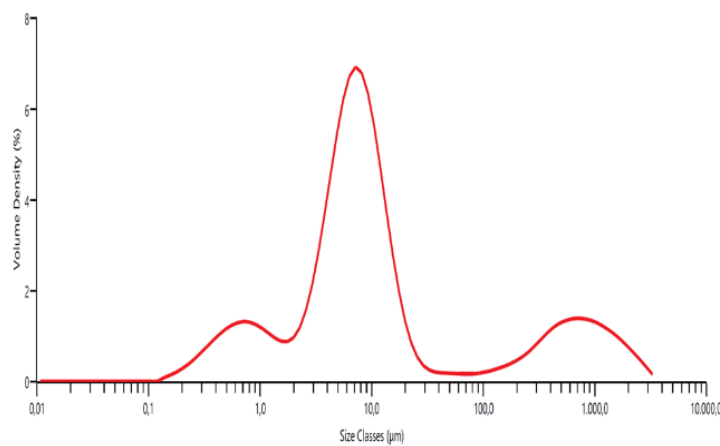
The copper-copper oxide particle size distribution ranges from 0.1 to 10 (Figure 4.8c). The synthesizing conditions of the process (temperature, the ratio of components, and



their concentration.) allow controlling the particles' size and shape. However, the obtained particle size is small compared to the work reported by Khan et al. [122].



(b)



(c)

Figure 4.8: Particle size distribution of a) barium hexaferrite, b) cobalt oxide and c) Cu and Cu<sub>2</sub>O

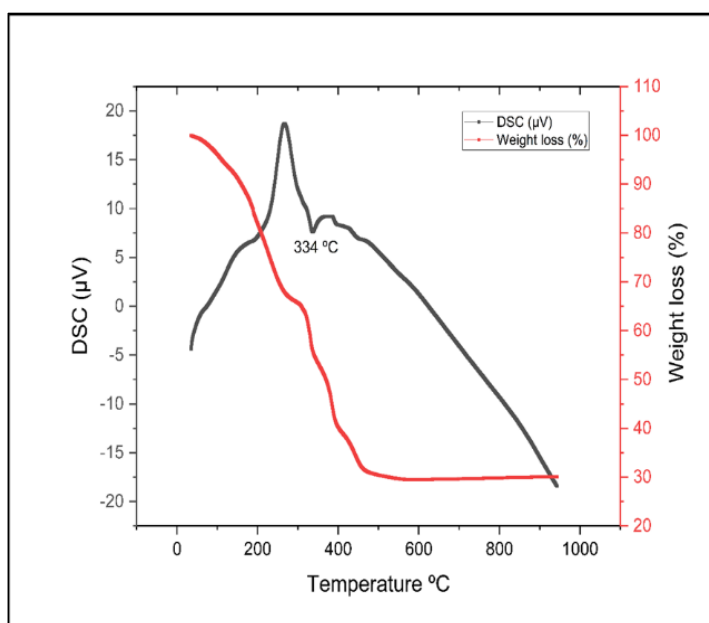
## 4.5 Thermal analysis

The thermogravimetric analysis was carried out to study the phase formation temperature of synthesized powders. The TGA/DTA curves for the nitrate–citrate dried gel are presented in Figure 4.9a. The mass loss was mainly in the temperature range of 35 – 495 °C, which corresponds to a strong exothermic peak and endothermic on the DSC curve at 285.31°C and 159.71°C respectively, and this could be attributed to the reaction of nitrates with citric acid and removal of residual water—related to the decomposition reaction of the carboxyl group. Moreover, from 450°C to 950°C, the weight of the dried gel was not recorded in the TGA curve and remained reasonably constant afterward, indicating that the chemical reaction had been completed during the combustion reaction without considerable formation of other phases [123]. The total weight loss of the two steps is about 70.28%, similar to the observation reported by Mali and Ataie [124], where a total mass loss of 70.52% was reported. The results of the X-ray phase analysis confirm the data obtained. Therefore, barium hexaferrite samples were calcined at a temperature above 500°C.

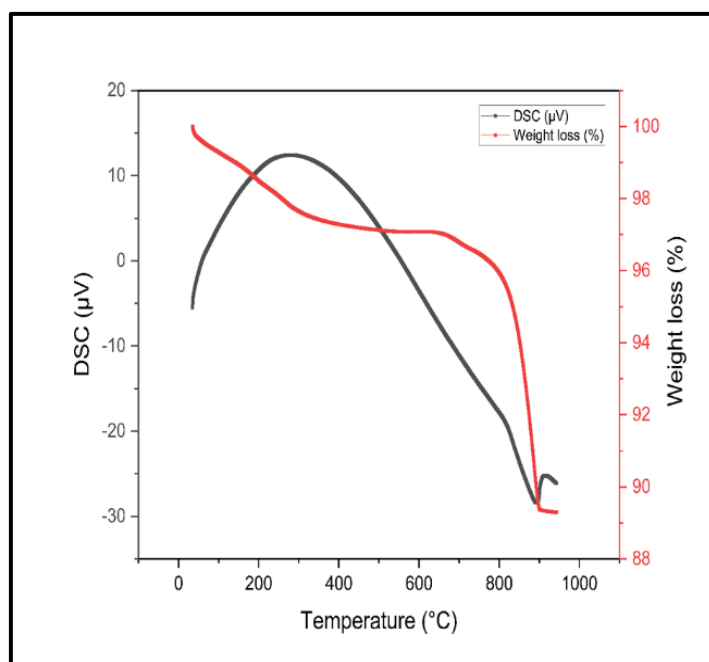
TGA/DSC analysis of copper-copper oxide is shown in Figure 4.9b. According to the result, the decomposition of the sample begins at a temperature above 300 °C, and the endothermic peak in the DSC curve at 900 °C corresponds to the oxidation process, which is much close to that of reported copper structures [125]. Usually, the oxidation process of copper powder begins at room temperature and accelerates when the temperature rises over 250 °C. However, the oxidation process continued until 902 °C, indicating that copper powder was not wholly oxidized and no significant change was observable afterward. Therefore, it is quite difficult to predict or interpret, much more regarding the reactions in the system [126].

Furthermore, the TGA/DSC curve for dried cobalt oxide gel presented in Figure 4.9c shows that the weight loss can be differentiated into three regions. A weight loss of 11.6 % was detected in the first region from 0°C to 197.34 °C. An apparent weight loss of 49.77% in the TGA curve was observed in the second stage from 297.34 °C to 348.56 with an exothermic peak at 252.8 °C in the DSC curve, which corresponds to the decomposition reaction of the complex through an intramolecular redox process of  $\text{Co}(\text{NO}_3)_2$  and  $\text{C}_2\text{H}_6\text{O}_2$ . Finally, a weight loss of 17.87% in the TGA curve was

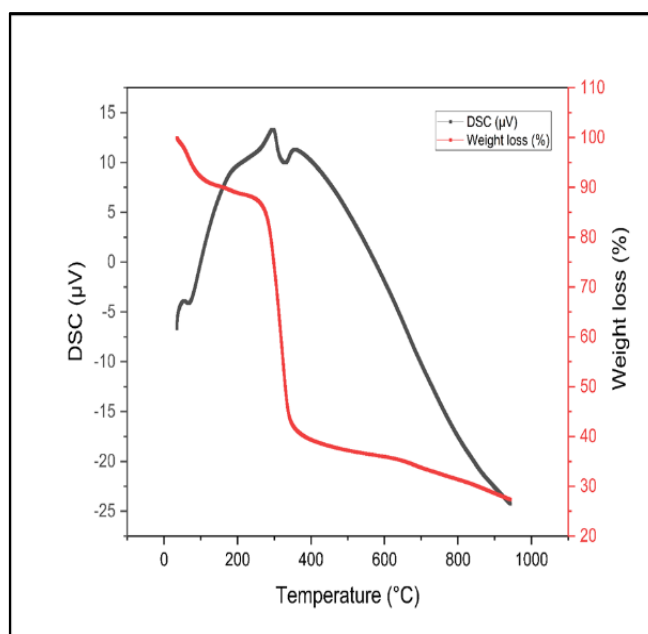
observed in the third stage between 348.5 °C and 960 °C, and one weak endothermic peak appeared at 397.37 °C in the DSC curve, which was due to the further combustion of the of unreacted residues. Notwithstanding, the precise reaction is unknown, and intermediates and gaseous products have not been explicitly identified, but the result agrees with previous studies' data [127.128]. The weight of the dried gel was not decreased in the TGA curve when the temperature was higher than 452 °C.



(a)



(b)



(c)

Figure 4.9: TGA/DSC curve of a) barium hexaferrite, b) cobalt oxide, and c) Cu - Cu<sub>2</sub>O

## 4.6 Vibrating Sample Magnetometer (VSM)

Room temperature hysteresis loops of barium hexaferrite, cobalt oxide, and copper powder are shown in Figure 4.10. The results from the hysteresis loops indicated that only barium hexaferrite was magnetically soft when an external field was applied and exhibited strong ferromagnetism behavior at room temperature. The saturation magnetization  $M_s$  value of barium hexaferrite under a field of 10 kOe was 54 emu/g. Despite the average particle size of barium hexaferrite in this work being quite large compared to the reported in the literature, the observed  $M_s$  value does not significantly differ from the reported values in the previous studies using different synthesizing approaches. A similar observation was made by Shepherd [129], which confirms that saturation magnetization is mainly unaffected by particle size. However, according to Xu et al. [130], the magnetic properties of the powders are influenced significantly by calcination temperature. Due to the fact that calcination temperature has a significant effect on the morphology and phases of the synthesized powder.

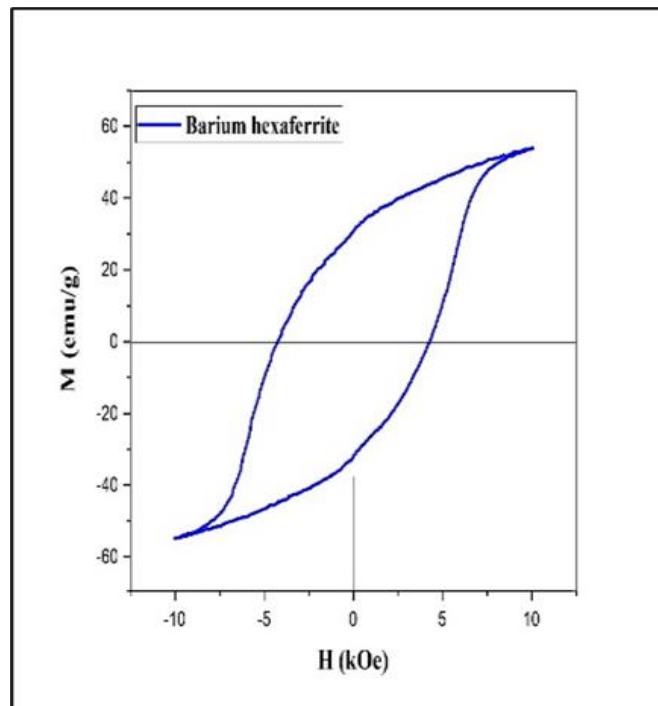
Furthermore, the coercivity value 4298 Oe was observed for barium hexaferrite, which is as much as 20% smaller than those reported values in the previous studies [131, 132,

133]. This can be explained as an effect of many factors. Shalini et al. [134] argued that the composition, crystal structure, shape and size of the grains, and inter-granular interactions affect the coercivity of the powder.

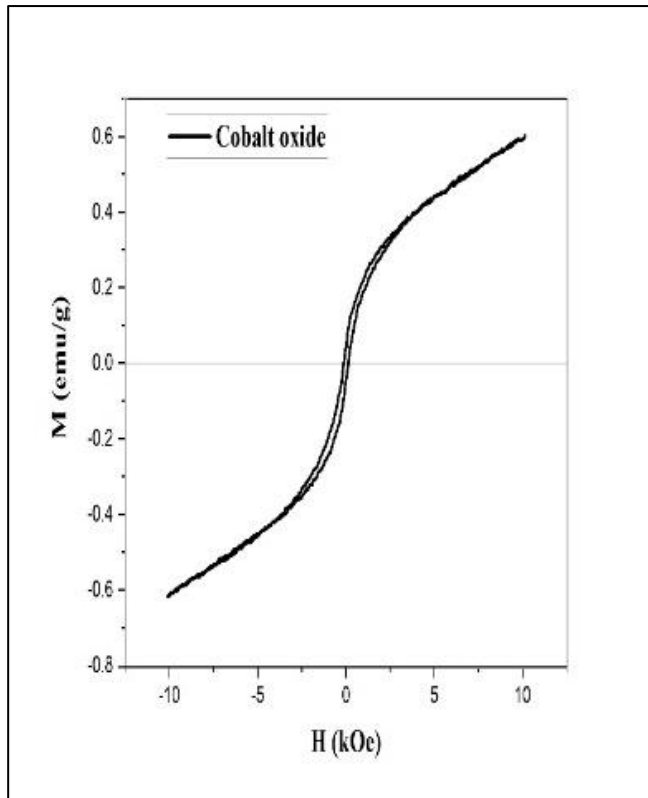
On the other hand, the saturation magnetization and coercivity for cobalt oxide  $C_3O_4$  were found to be 0.60 emu/g and 131 Oe, respectively. The observed values of cobalt oxide are comparable to the reported values in the literature [135,136,137]. Although there has been extensive research on  $C_3O_4$ , studies on its critical magnetic behavior are still controversial. However, the magnetic properties highly depend on particle size, structure, and morphology [138]. In addition, the calcination temperature plays an important role. The saturation magnetization ( $M_s$ ), and coercivity ( $H_c$ ), decrease as the calcination temperature increases.

Copper-copper oxide Cu-Cu<sub>2</sub>O sample showed a weak ferromagnetic behavior with a saturation magnetization and coercive of 0.40 emu/g and 0.4.38 Oe, respectively. No magnetic saturation of the powder was observed. The low magnetization of the Cu-Cu<sub>2</sub>O sample could be attributed to the presence of two diamagnetic phases [139].

The values of saturation magnetization ( $M_s$ ), coercivity ( $H_c$ ), and remnant magnetization ( $M_r$ ) determined from hysteresis loops are presented in Table 4.1



(a)



(b)

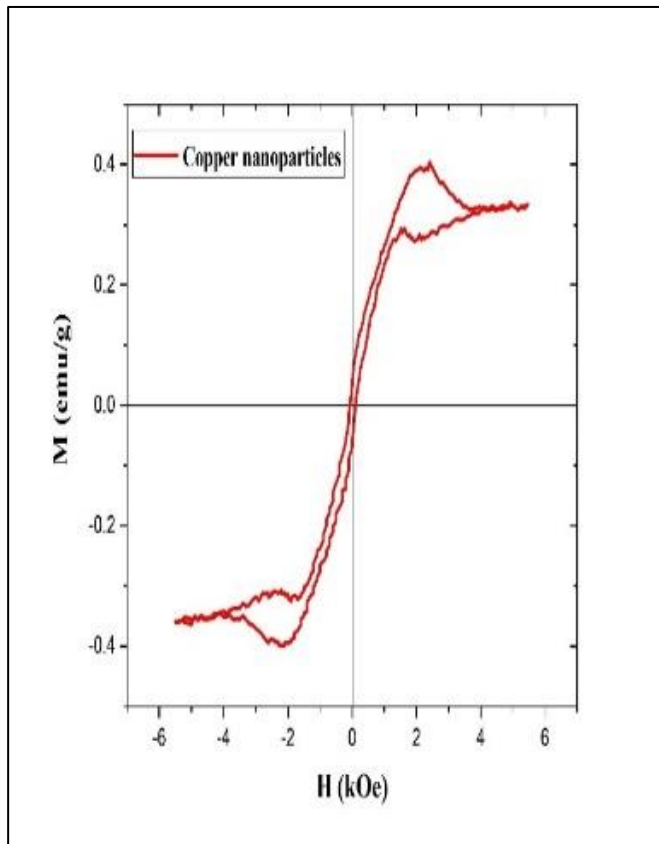


Figure 4.10: Magnetic hysteresis loop of a) barium hexaferrite, b) cobalt oxide, and c) Cu and Cu<sub>2</sub>O.

Table 4.1: Magnetic properties of the synthesized samples

Sample	$M_s$	$H_c$	$M_r$	$M_r/M_s$
Copper-Copper oxide	0.40	107.38 Oe	0.04	0.095
Cobalt oxide	0.60	131.86 Oe	0.04	0.068
Barium hexaferrite	54	4298 Oe	30.79	0.570

## 4.7 Density of composites

Since the purpose of this study is to manufacture lightweight RAMs, it was necessary to calculate the density of the produced composites. Furthermore, density is crucial in controlling the manufacturing process and cost to determine the intended application. Moreover, RAMs must meet the requirements for density and size in addition to the required reflection coefficient values

The density of the produced composites was calculated using the weight and dimensions of the samples (Without considering the pores) by applying the following formula:

$$\rho = m/v \quad (3.1)$$

It is worth mentioning that only the samples with a 50% concentration density were taken into consideration. Hence, the increase in the amount of dispersed phase causes an increase in the density of the composite. However, the calculated density of each composite is presented in Table 4.2.

Table 4.2: Density of composites.

Sample	Weight (dB)	Density (g/cm <sup>3</sup> )
RA1	1.614	1.280
RA2	1.874	1.478
RA3	1.867	1.488
RA4	1.441	1.143
RA5	1.544	1.225
RA6	1.674	1.328

The average density of the composites is between 1.14 and 1.4 g/cm<sup>3</sup>, which indicates that the produced RAMs are lightweight, although the concentration of dispersed phase is significant. Generally, the density of composite material depends on the type of dispersed phase, shape, particle size, and packing density. The literature is replete with studies on producing lightweight radar-absorbing materials, but none has reported the value of the density. Consequently, it is difficult to directly compare the data obtained in this study with the previous studies. However, according to Kumar and Singh [140], the average density of multilayer radar-absorbing material is between 1.5 to 3.5 g/cm<sup>3</sup>.



## 4.8 Microwave network analyzer

The reflection loss RL values of the composites were measured in different frequency ranges (8-12 GHz), and the frequency and effective band gaps that could be used as potential radar absorbers of each composite were determined. According to the literature, the -10 dB RL value corresponds to 90% absorbance [141]. The frequency dependence of the reflection loss of the composite samples showed an interference-absorbing type. The absorption of electromagnetic waves in this material is based on the phenomenon of mutual compensation of the incident and the reflection from the material. An increase in filler content over 15% in all samples leads to an increase in the reflection loss. The frequency dependence of reflection loss for RA1 are shown in Figure 4.11. The RA1 50% wt. demonstrated a minimum reflection loss of -27.3 dB (99.99 percent absorption) at 10.72 GHz and an effective absorption bandwidth of 2.34 GHz (reflection loss >-10 dB, 90% absorption) over a frequency range of 9.66 to 12 GHz. A reflection loss of -21.32 dB at 9.55 GHz was observed in the RA1 25 wt.% sample, whereas the response bandwidth was. Reflection loss R.L for RA2 is shown in Figure 4.12. The RA2 50% wt. demonstrated a minimum reflection loss of -37.82 dB (99.99 percent absorption) at 11.20 GHz and an adequate absorption bandwidth of 2.34 GHz (reflection loss >-10 dB, 90% absorption) over a frequency range of 9.66 to 12. A reflection loss of -21.32 dB at 9.55 GHz was observed in the RA2 25 wt.% sample. At the same time, the response bandwidth was 2.7 GHz, with a frequency bandwidth ranging from 9.18 to 11.88 GHz—additionally, RA2 15wt.% showed a reflection loss of -16.94 at 12 GHz with a bandwidth of 0.82 GHz (reflection loss < -10 dB). Only RA2 5wt.% exhibits a low reflection loss of less than -10 dB over all frequencies. Both RA1 and RA2 samples consist of two layers of barium hexaferrite; however, RA2 showed a minimum reflection loss of -37.82 dB compared to -27.3 dB for RA1, and the reason for that is thought to be due to the structural polarization, which can be observed in multi-layers composite materials with dielectrics and semiconducting or layers with different conductivity. Losses of electromagnetic energy of resonant absorption occur when the electric field frequency approaches the frequencies of natural oscillations of electrons or ions to magnetic. Figure 4.13 shows the Reflection loss R.L for RA3. the peak value for RA3 50% is -29.33 dB at 10.75 GHz, and the effective bandwidth is 1.87 GHz (10.2–11.90 GHz). A multi-peak radar-absorbing feature was observed in the frequency range of 8 GHz to 12 GHz for RA3

25%, compared to the only one absorbing peak in RA3 50% in the same frequency range. As a result of the frequency dependency of microwave reflectivity, the multi-peak property is critical for broad bandwidth absorption.

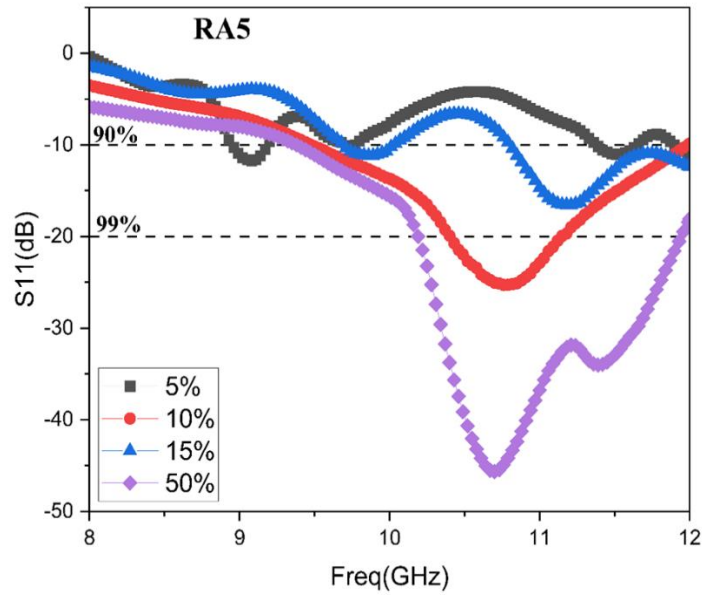


Figure 4.11: Reflection loss of RA1 as a function of frequency

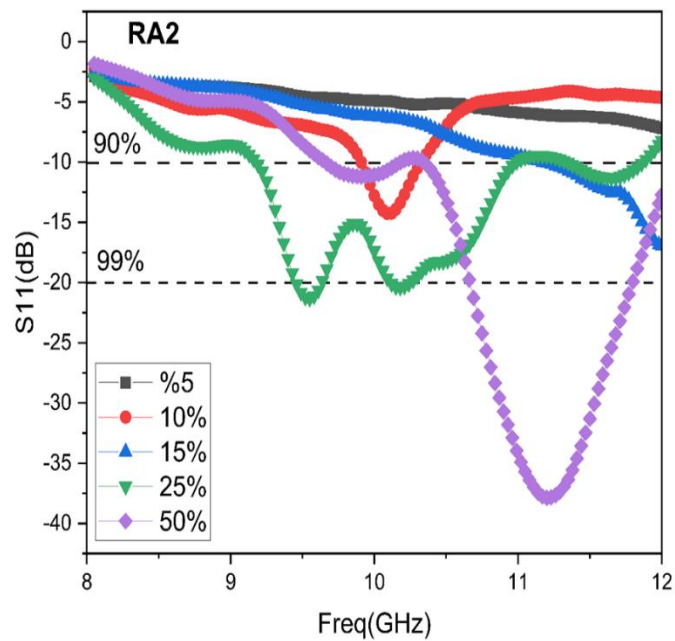


Figure 4.12: Reflection loss of RA2 as a function of frequency

RA3 25 wt.% exhibited a minimum R.L of -17.64 dB at 10.76 GHz and good absorption performance at frequencies higher than 11 GHz. The effect of microwave absorption is not obvious in RA3 5%. The bandwidth (reflection loss  $>-10$  dB, 90% absorption) for RA3 5% is 0 GHz. However, the RA4 50% wt. showed a minimum reflection loss close to RA3 50% of -29.82 dB at 11.20 GHz, as seen in Figure 4.14, and an effective absorption bandwidth of 2.34 GHz (reflection loss  $>-10$  dB, 90% absorption) over a frequency range of 9.66 to 12. A reflection loss of -21.32 dB at 9.55 GHz was observed in the RA4 25 wt.% sample; in comparison, the response bandwidth was 2.7 GHz, with a frequency bandwidth ranging from 9.18 to 11.88 GHz.

Additionally, RA4 15wt.% showed a reflection loss of -16.94 at 12 GHz with a bandwidth of 0.82 GHz (reflection loss  $<-10$  dB). Only RA2 5wt.% exhibits a poor reflection loss of less than -10 dB over all frequencies. It can be observed that the minimum value of R.L was not exceeded -30 dB in two layers of copper-copper oxide samples when the content was 50%. The electrically conductive material can be beneficial for microwave absorption; however, the presence of copper oxide in the powder affected the overall absorption properties of the samples.

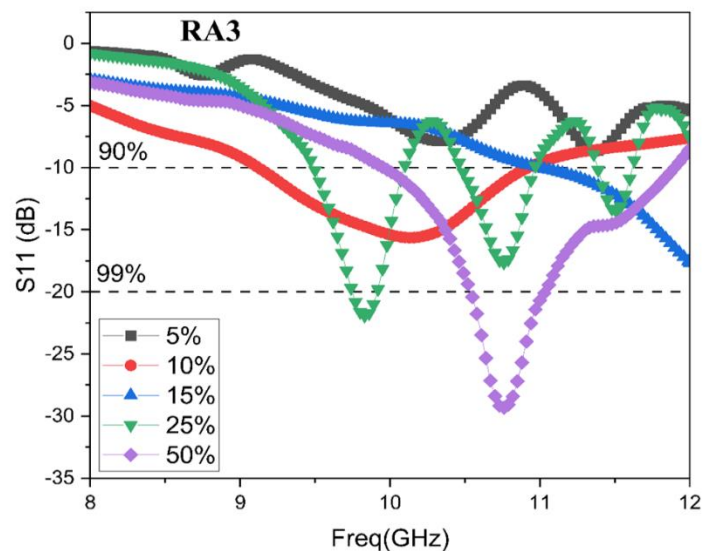


Figure 4.13: Reflection loss of RA3 as a function of frequency

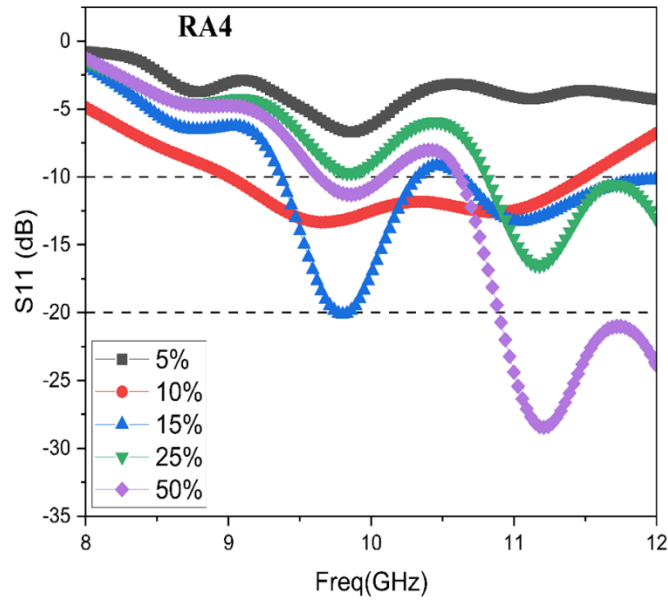


Figure 4.14: Reflection loss of RA3 as a function of frequency

High absorption was observed in the sample with two layers of cobalt oxide. RA5 50% wt showed the highest absorption peaks based on the results of the reflection loss shown in Figure 4.15 with a minimum reflection loss of  $-45.68$  dB at 10.80 GHz with a bandwidth of 2.63 GHz. Compared to other samples with the same weight content, RA5 5wt.% exhibits a good reflection loss of less than  $-11.82$  dB at 11.51 GHz. A reflection loss of  $-25.32$  dB at 10.77 GHz was observed in the RA5 10 wt.% sample, and the response bandwidth was 2.51 GHz, with a frequency bandwidth ranging from 9.18 to 11.88 GHz—additionally, RA5 15wt.% showed a reflection loss of  $-15.97$  at 12 GHz with a bandwidth of 1.19 GHz. Generally, according to the nature of interaction with electromagnetic fields, radar-absorbing material can be divided into two main groups: dielectric and ferromagnetic. Dielectrics only have electric losses, while ferromagnetic materials have electrical and magnetic losses. The high absorption of the RA5 sample was attributed to combining a conductive filler (Cu-Cu<sub>2</sub>O) and a magnetic semiconductive filler (cobalt oxide).

The microwave absorption mechanism is explained as an effect of magnetic loss, dielectric loss, and different reactions. The polarization relaxation and interfacial polarization are the primary causes of solid dielectric loss, while the natural resonance and the eddy current effect are major causes of magnetic loss [142]. Furthermore,

cobalt oxide plays a significant role, bringing dielectric loss and strengthening polarization. Meanwhile, the excellent conductivity of Cu-Cu<sub>2</sub>O increases dipole moment and encourages polarization and relaxation processes. Moreover, the multilayered structure of the samples may develop various reactions of incident microwaves, which could also improve the microwave absorbing properties.

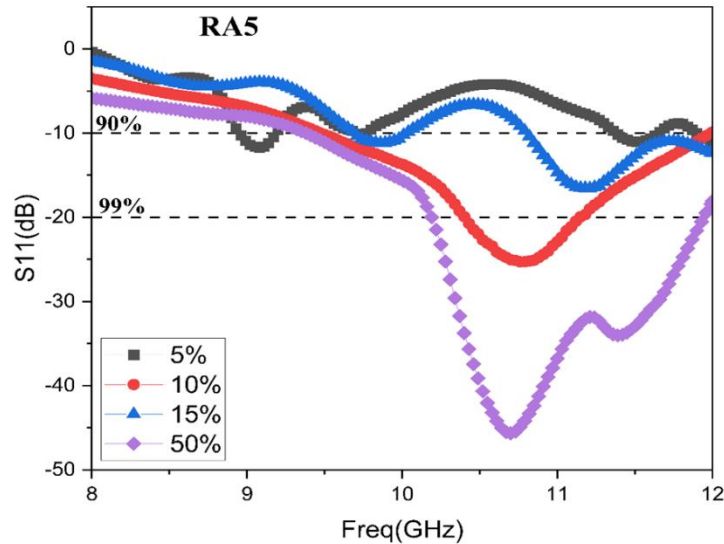


Figure 4.15: Reflection loss of RA5 as a function of frequency

The frequency dependence of the reflection loss for the RA6 (Figure 4.16) showed that the minimum reflection loss values shifted to higher frequencies with increasing the concentration of reinforcements. For instance, the minimum reflection loss values were observed in the sample RA6 50 wt.% with -29.62 dB at 11.73 GHz. On the other hand, on RA6 5wt.%, the reflection loss starts to appear at higher frequencies.

The frequency dependence of the reflection loss for the RA6 (Figure 4.16) showed that the minimum reflection loss values shifted to higher frequencies with increasing the concentration of reinforcements. For instance, the minimum reflection loss values were observed in the sample RA6 50 wt.% with -29.62 dB at 11.73 GHz. On the other hand, on RA6 5wt.%, the reflection loss starts to appear at higher frequencies.

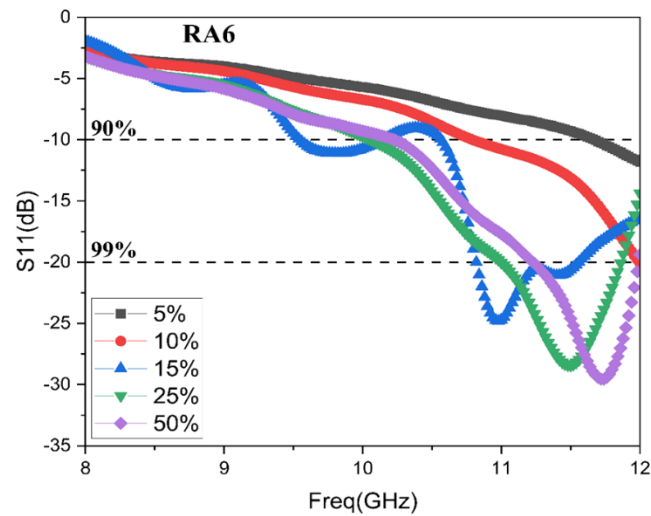


Figure 4.16: Reflection loss of RA6 as a function of frequency

Table 4.2 summarizes the comparative results of reflection loss values and corresponding bandwidths

Table 4.3: Summaries of reflection loss values

Sample	Frequency (GHz)	Reflection loss (dB)	Bandwidth (under $-10$ dB)
RA1	10.72	-27.3 dB	2.37
RA2	11.20	-37.82	2.34
RA3	10.75	-29.33	1.87
RA4	11.20	-29.82	2.34
RA5	10.80	-45.68	2.63
RA6	11.73	-29.62	1.78

As seen in Figures 4.17, 4.18, 4.19, 4.20, and 4.21, RA5 composites showed a strong absorption ability in all samples with different reinforcements. Furthermore, a strong absorption ability is due to the reason mentioned earlier and the homogeneous dispersion of the reinforcements throughout the matrix material. A material's radar-absorbing properties depend on the distribution of powders in the matrix and the magnetic and dielectric properties [143]. The obtained results indicate that the RA5 samples have excellent microwave absorbing properties in a wide frequency range

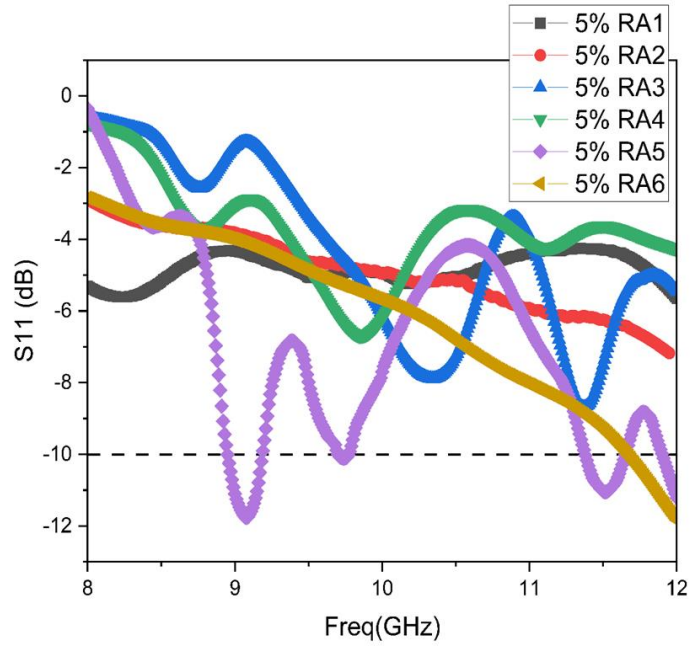


Figure 4.17: Reflection loss of 5% composites as a function of frequency

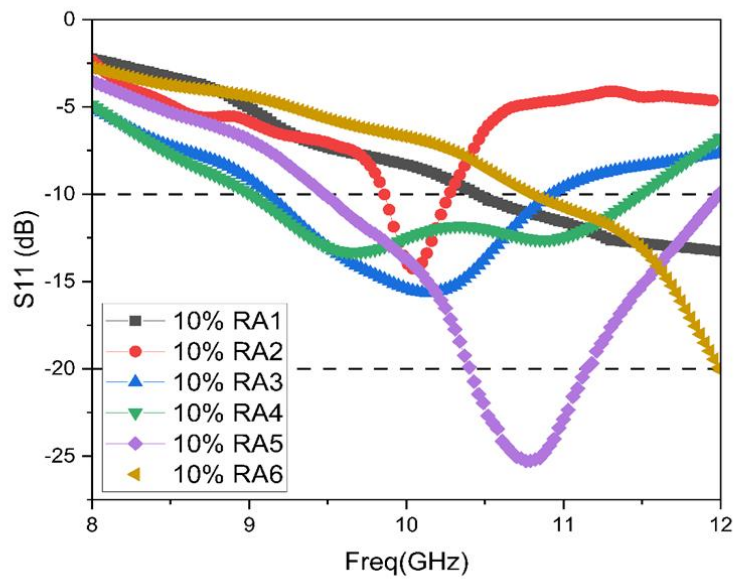


Figure 4.18: Reflection loss of 10% composites as a function of frequency

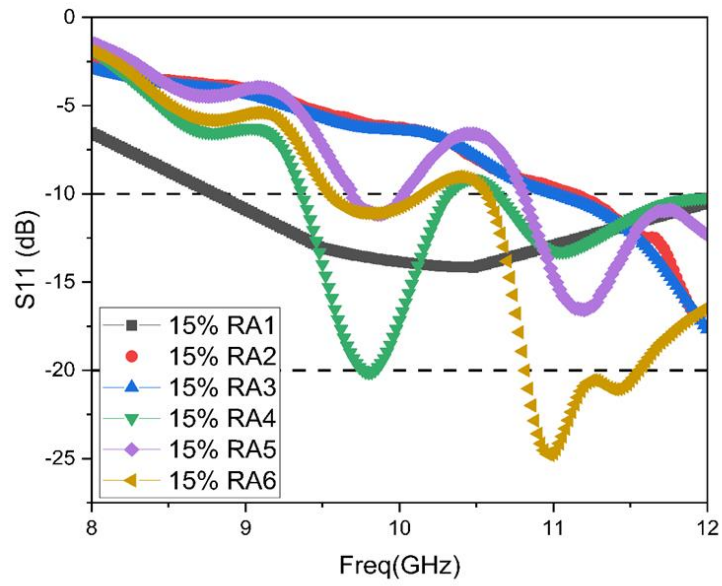


Figure 4.19: Reflection loss of 15% composites as a function of frequency

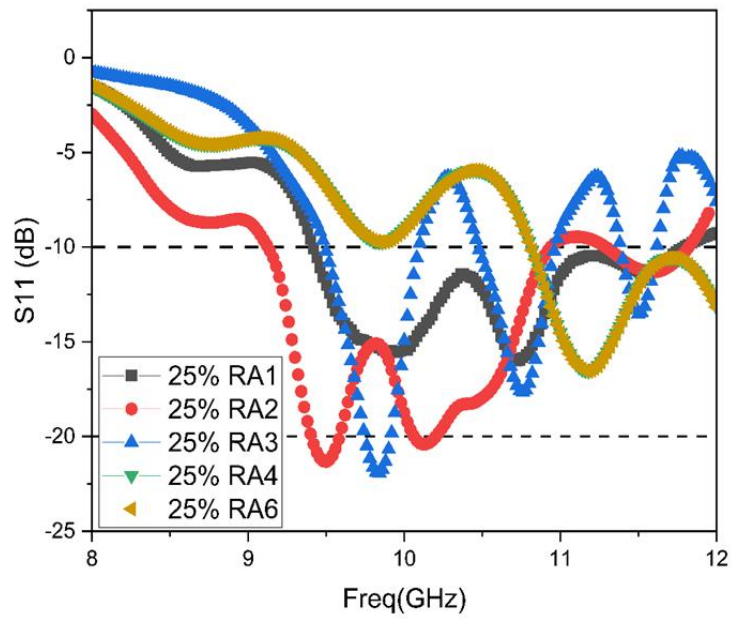


Figure 4.20: Reflection loss of 25% composites as a function of frequency



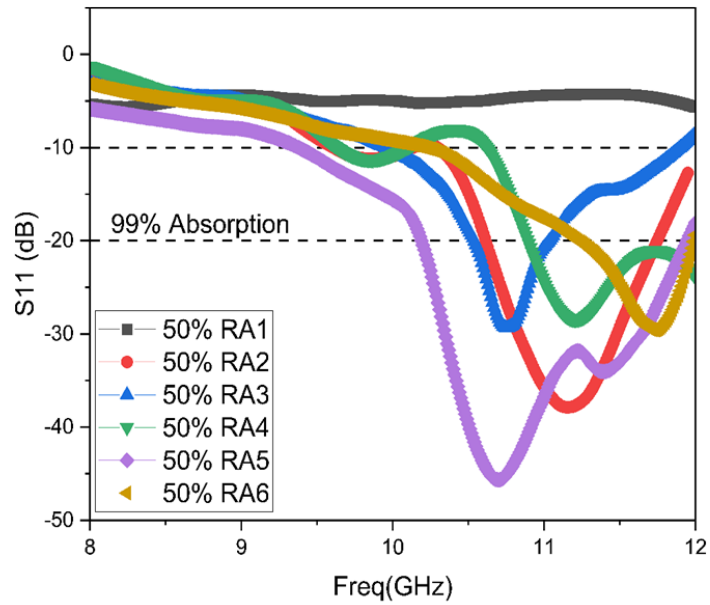


Figure 4.21: Reflection loss of 50% composites as a function of frequency

For comparison, the radar absorption properties of composites containing 50% BaFe<sub>12</sub>O<sub>19</sub>, Cu<sub>2</sub>-Cu, and Co<sub>3</sub>O<sub>4</sub> were also studied and shown in Figure 4.22. Although barium hexaferrite is well known as a promising material for radar absorbing, it was found that the 50% Cu<sub>2</sub>-Cu composite has the highest absorption peaks in this work as the particle size is less than 10 μm compared to the other two. It can be argued that the reinforcement's particle size directly affects the composite's radar properties since the surface area of the reinforcement increases with decreasing the particle size surface area, which increases the electromagnetic wave contact points [144]. Thus, decreasing particle size increases the interaction points with electromagnetic wave interactions. The minimum reflection loss value for the 50% Cu<sub>2</sub>-Cu sample was around -23.88 dB at 11.27 GHz. Dielectric loss contributed to the electromagnetic loss for the Cu<sub>2</sub>-Cu sample, while for the BaFe<sub>12</sub>O<sub>19</sub> and Co<sub>3</sub>O<sub>4</sub>, the effect of magnetic loss was dominant. In general, good electromagnetic wave absorption results from an effective balance between a material's permittivity and permeability, which means that the sample with Cu<sub>2</sub>-Cu shows a good electromagnetic wave absorption.

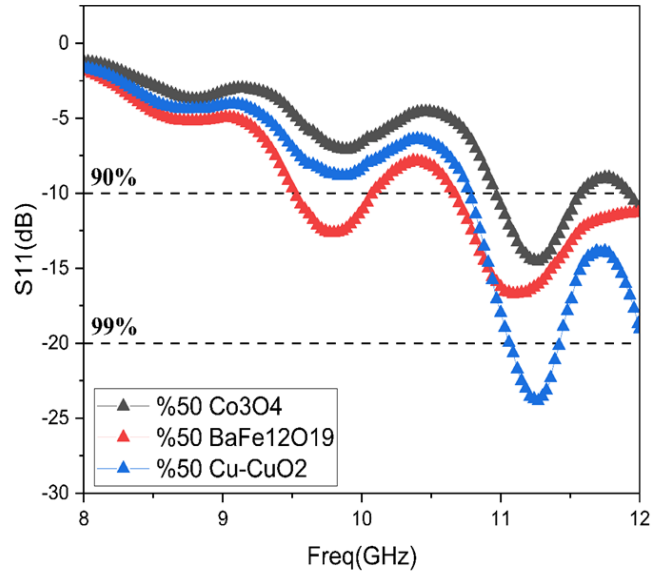


Figure 4.22: RL of composites containing 50% of BaFe<sub>12</sub>O<sub>19</sub>, Cu<sub>2</sub>-Cu, and Co<sub>3</sub>O

Based on the analysis of frequency dependences, the most effective absorption is possessed by sample RA5 50 wt.% while samples with a 5% weight fraction have poor reflection loss. In general, although the increase in reinforcements weight fraction improves the reflection loss performance, the high reinforcement content reduces the polymer matrix's mechanical properties and increases the porosity. With increasing reinforcements content, the absorption values of the composites increase, but the effective bandwidth decreases—nevertheless, the content of less than 10 wt. % is not advisable due to a decrease in the efficiency of radar absorption. On the other hand, reflection loss at 5% in all samples is quite difficult to interpret, much more in terms of the effects of the reinforcements, as the RL values were identical in all samples.

The obtained in this study are consistent with Zhang et al. [145], Li et al. [146], and Liu et al. [147] results. Zeng et al. found that the reflection loss of multilayer material based on copper oxide/cobalt/carbon with 4 mm thickness depends on the number of layers and filler content, which confirms that the values of the reflection loss of the material depend on the content of filler. A similar observation was also made by Tang et al. [148], where an improvement in electromagnetic wave absorption properties of M-type barium ferrite powders modified with polyaniline was reported. Tang et al.

found that the microwave absorption properties of composites increased with polyaniline and M-type barium ferrite content, which is quite similar to this work.

In contrast, the study by Feng et al. [149] indicated that an increase in carbonyl iron content reduces the minimum reflection loss and shifts the frequency. The reason for this is attributed to the fact that the size distribution of reinforcement particles. This suggests that the particle size distribution influences the absorption property besides the reinforcement concentration. Xiang et al. [150] also indicated that the finely dispersed particles have significant effects and lead to an increase in the efficiency of absorption of electromagnetic

Notwithstanding, the average particle sizes of barium hexaferrite vary mainly in the range from 10 to 100  $\mu\text{m}$  which is quite large compared to other works using the same synthesizing approach; the 50% -BaFe<sub>12</sub>O<sub>19</sub> composite showed a better reflection loss compared to work done by Ghasemi et al. [151] and Xu et al. [152]. This difference may be attributed to the morphology and size distribution of reinforcement particles being significantly different from the previous studies. These factors can noticeably affect the effective absorption properties of composite materials, as mentioned earlier.

However, the high absorption of the RA5 sample is attributed to combining a conductive filler (Cu-Cu<sub>2</sub>O) and an excellent dielectric property of cobalt oxide. Jun et al. [153] observed a similar minimum RL value of -42.7 dB for a layer of 4 mm thickness in a multilayer composite of copper oxide/cobalt/carbon. The incident electromagnetic wave is partially reflected from the first layer's surface and scattered according to the absorber's working principle. By matching the wave impedances of the absorber and the electromagnetic wave propagation, it is possible to reduce the amount of reflected energy. The second layer absorbs electromagnetic wave energy because copper oxide has excellent dielectric properties. Using metal oxides (copper and cobalt oxide) as filler makes a good connection between the electric and magnetic fields. Such a connection can help reduce the level of reflection of electromagnetic waves. The advantage of metal oxides is the possibility of increasing the effective magnetic permeability without using a heavy magnetic material. Previous studies on magnetic and dielectric permittivity and absorbing properties of cobalt oxide and copper oxide composites support the findings of this study.

Moreover, the Intense absorption observed in RA2 is mainly due to natural ferromagnetic resonance by barium hexaferrite. This result is similar to Handoko et al. study [154]. The dipole relaxation model of polarization can describe the frequency dependencies. However, the absorption of radar and the frequency can be changed by doping barium hexaferrite with various elements Al and others, which leads to changes in the internal magnetic fields of the material [155,156]. It was found that absorption of electromagnetic was achieved at a lower content of additive in doped barium hexaferrite powders of various sizes of fine particles with a wide size distribution.

Despite the wide range of radar absorption materials, one of the main drawbacks is the complex production technology. For instance, Sun et al. [157] reported an absorption performance of -42 dB in copper-cobalt-nickel ferrite/graphene oxide/polyaniline composites when the filler content was 40 % with a thickness of 3 mm. However, problems of uniform distribution of the filler's distribution in the polyaniline, both in the form of individual particles and agglomerates, led to the material inhomogeneity and affected the microwave absorbing characteristics. Wu et al. [158] used carbon nanotubes and cobalt oxide hybrid composite with 60 wt.% and 40 wt.% content in epoxy resin. A minimum RL value of - 31.5 dB was achieved at just 2 mm thickness. Nevertheless, the high point of the procedure described in this study is a simple method; moreover, Wu et al. reported that the material cost was relatively high.

In addition, compared to the reflection loss reported by Parsian et al. [159] and Mosleh et al. [160], it was observed that this study's findings show better RL values. In addition, the expensive materials and complex preparation technology make this study's proposed method more technologically advantageous.

Furthermore, the main advantage of obtained composites absorbing is multilayer with a thickness of less than 4 mm, and a minimum reflection loss of -45.68 dB was achieved. Most studies reported minimum reflection loss values of multilayer materials with thicknesses between 8-12 mm [161,162,163]. Radar absorbing materials (RAMs) are heavy when thickness increases, so their use in electromagnetic protection technology is limited. For example, Shyr et al. [164] prepared a microwave-absorbing material based on a mixture of polyester and steel fibers. The material consists of 11 layers with a total thickness of 23-25 mm and provides a reflection coefficient of less than -20 dB. However, practical use for this material is impossible

due to its unacceptable thickness. Generally, high additive content (30% and above) negatively affects homogeneous dispersion and mechanical properties of the polymer matrix; however, a maximum of 50% additives was used in this study as additives homogeneously distributed in the matrix. It suggested that using ferrites and metal oxides as radar-absorbing material to fabricate a flexible structure, the total thickness of the product should not exceed 8–10 mm. Considering that in a structural radar absorbing material with an electrically conductive filler, energy absorption is exclusively associated with electrical losses, to achieve the specified values of the reflection coefficient of an electromagnetic wave, it is necessary to increase the concentration of the filler.

In general, although the increase in reinforcements weight fraction improves the reflection loss performance, high reinforcement content reduces the mechanical properties of the polymer matrix and increases the porosity. Furthermore, with increasing reinforcements content, the absorption values of the composites increase, but the effective bandwidth decreases. Thus, it is evident that today not only the problem of creating materials that are effective in radio absorption but also efficient and cost-effective in terms of the technology used for their manufacture is equally relevant.

# Chapter 5

## Conclusion

This work aimed to produce and develop flexible multilayer radio-absorbing materials with significant electrophysical properties for protecting humans and other biological and technical objects from the effects of electromagnetic radiation in the radio frequency range.

The three reinforcement materials, barium hexaferrite, cobalt oxide, and copper-copper oxide, were successfully synthesized in the first part of the work. First, barium hexaferrite powder was synthesized by the sol-gel method using Iron nitride, barium nitride, and citric acid. Next, copper-copper oxides were synthesized by the chemical reduction method using copper (II) sulfate pentahydrate, ascorbic acid solution, and sodium hydroxide. Finally, cobalt oxide nanoparticles were synthesized by sol-gel method using cobalt (II) nitrate hexahydrate and ethylene glycol.

VSM results show that barium hexaferrite and cobalt oxide samples exhibited superparamagnetic behavior at room temperature, while copper oxide showed diamagnetic behavior. XRD patterns of synthesized samples have a high degree of congruence with those of the JCPDS cards in the literature. There was no secondary impurity phase found.

Particle analysis revealed that average particle sizes of synthesized barium hexaferrite were mainly in the range from 10 to 100  $\mu\text{m}$ . In addition, the synthesized cobalt oxide and copper-copper oxide particle sizes were 4-40  $\mu\text{m}$  and 0.1-10, respectively.

Three-Layer RAMs were prepared in a polyester resin matrix in the second part. A two-step procedure was used to prepare the three-layer RAMs. In the first stage of the process, barium hexaferrite, cobalt oxide, and copper-copper oxide were mixed with polyester resin in the following weight fractions: 50%, 25%, 15%, 10%, and 5% (wt./wt.). In the second step, seven different structures were designed.

SEM images of composites showed that the synthesized powders were generally homogeneously distributed throughout the entire matrix; partial agglomerations were detected in some areas of some samples.

RAMs were measured in the radio frequency range by using a network analyzer. The reflection loss (RL) test findings showed that the microwave absorption of RAMs increased as the weight fractions increased. The investigation of the radar characteristics revealed that the sample RA5 50 weight percent, composed of two layers of cobalt oxide and one layer of copper-copper oxide, had the most efficient absorption. At a frequency of 10.25 GHz, the reflection loss reached a maximum value of -45 dB. Based on these results, it can be concluded that RA5 composites can be a good candidate for radar-absorbing material.

# References

- [1] Askeland, D. R., Phulé, P. P., Wright, W. J., & Bhattacharya, D. K. (2003). *The science and engineering of materials*.
- [2] Habash, R. W. Y. (2010). Environmental and human impact of electromagnetic energy: views toward technology and risk. *energy & environment*, 21(2), 107–113. <http://www.jstor.org/stable/43734901>
- [3] Moupfouma, F., Klim, Z., & Skorek, A. (2013). Electromagnetic Protection Hazards on Composite versus Metallic Aircraft. *SAE International Journal Of Aerospace*, 6(2), 441-446. doi: 10.4271/2013-01-2157
- [4] Bystrov, R., Dmitriev, V., Potapov, A., Perunov, Y., & Cherepenin, V. (2014). Electromagnetic systems and means of deliberate impact on physical and biological objects. *Radioelectronics. Nanosystems. Information Technologies.*, 129-169. doi: 10.17725/rensit.0006.201412a.0129
- [5] Yazar, M. (1979). Civilian EMC Standards and Regulations. *IEEE Transactions On Electromagnetic Compatibility*, EMC-21(1), 2-8. doi: 10.1109/temc.1979.303789
- [6] Jackson, G. (1990). Setting the standards. *The European EMC Directive*. *IEE Review*, 36(4), 143. doi: 10.1049/ir:19900059
- [7] Guidelines for Limiting Exposure to Electromagnetic Fields (100 kHz to 300 GHz). (2020). *Health Physics*, 118(5), 483-524.
- [8] Habash, r. (2019). *Electromagnetic fields and radiation*. [s.l.]: crc press.
- [9] Institute of Electrical and Electronics Engineers. (2010). *IEEE recommended practice for measurements and computations of electric, magnetic, and electromagnetic fields with respect to human exposure to such fields, 0 Hz to 100 kHz*. New York.
- [10] Swanson, J. (2016). *Power-frequency EMF Exposure Standards applicable in Europe and elsewhere [Ebook]* (p. 1). Retrieved from <https://> Matulík, M. (2016). *Bio-*
- [11] *Electromagnetic compatibility* (1st ed.). LAP LAMBERT Academic Publishing. [/www.emfs.info/wp-content/uploads/2015/07/standards-table-August-2016.pdf](http://www.emfs.info/wp-content/uploads/2015/07/standards-table-August-2016.pdf)



- [12] Rozorinov, H., Hres, O., Rusyn, V., & Shpatar, P. (2020). Environment of electromagnetic compatibility of Radio-Electronic Communication Means. *Informatyka, Automatyka, Pomiary w Gospodarce i Ochronie Środowiska*, 10(1), 16–19. <https://doi.org/10.35784/iapgos.917>
- [13] Sakharov, K. Y., Parfenov, Y. V., Zdukhov, L. N., Titov, B. A., & Turkin, V. A. (2012). The present state and problems of standardization in the protection of the civil infrastructure from powerful electromagnetic influences. *Measurement Techniques*, 55(2), 183–188. <https://doi.org/10.1007/s11018-012-9938-6>
- [14] Jackson, G. (2016). Setting the standards. *The European EMC Directive*. *IEE Review*, 36(4), 143. doi: 10.1049/ir:19900059
- [15] Murugan, M., & Kokate, V. K. (2009). Microwave absorbing polymer composites. *2009 International Conference on Emerging Trends in Electronic and Photonic Devices & Systems*. <https://doi.org/10.1109/electro.2009.5441100>.
- [16] Zakharychev, E.A., Ryabov, S.A., Zefirov, V.L. et al. Development of polymer radio-absorbing materials with carbon nanotubes for extremely high frequency range. *Inorg.Mater. Appl. Res.*4, 405–409(2013).
- [17] Huitema, L., & Monediere, T. (2012). Dielectric materials for compact dielectric resonator antenna applications. *Dielectric Material*. <https://doi.org/10.5772/50612>.
- [18] Landau LD, Bell JS, Kearsley MJ, Pitaevskii LP, Lifshitz EM, Sykes JB. *Electrodynamics of continuous media*. elsevier; 2013 Oct 22.
- [19] Wei H, Zhang Z, Hussain G, Zhou L, Li Q, Ostrikov KK. Techniques to enhance magnetic permeability in microwave absorbing materials. *Applied Materials Today*. 2020 Jun 1;19:100596.
- [20] Kingsley S, Quegan S. *Understanding radar systems*. SciTech Publishing; 1999.
- [21] Bibikov S, Prokof'Ev M. Composite materials for some radiophysics applications. *InMetal, Ceramic and Polymeric Composites for Various Uses* 2011 Jul 20. IntechOpen.
- [22] Maity S, Singha K, Debnath P, Singha M. Textiles in electromagnetic radiation protection. *Journal of Safety Engineering*. 2013;2(2):11-9.
- [23] Vasilev, D. (n.d.). Animated explanation of the Radar Principle. *Short & Medium Range Radars for Training and Civil Aviation*. Retrieved October 18, 2022, from <https://www.skyradar.com/blog/radar-principle> Applications" *Open Chemistry*, vol. 17, no. 1, 2019, pp. 865-873. <https://doi.org/10.1515/chem-2019-0100>

- [24] Vinoy, K. J. and R. M. Jha, "Trends in radar absorbing materials technology," *Sadhana*, Vol. 20, 815–850, 1995.
- [25] Vorst André Vander, Rosen, A., & Kotsuka, Y. (2006). *Rf/microwave interaction with biological tissues*. Hoboken (NJ). Wiley
- [26] Gaylor, K. (1989). *Radar absorbing materials: mechanisms and materials*. Maribyrnong, Vic. DSTO Materials Research Laboratory.
- [27] Idris FM, Hashim M, Abbas Z, Ismail I, Nazlan R, Ibrahim IR. Recent developments of smart electromagnetic absorbers-based polymer-composites at gigahertz frequencies. *Journal of Magnetism and Magnetic Materials*. 2016 May 1; 405:197-208.
- [28] Atay, H. Y., & Çelik, E. (2013). Barium hexaferrite reinforced polymeric dye composite coatings for radar absorbing applications. *Polymer Composites*, 35(3), 602–610.
- [29] Abbas, S., Dixit, A., Chatterjee, R., & Goel, T. (2007). Complex permittivity, complex permeability and microwave absorption properties of ferrite–polymer composites. *Journal of Magnetism and Magnetic Materials*, 309(1), 20–24.
- [30] Atay, H. Y (2016). A comparison on radar absorbing properties of nano and microscale barium hexaferrite powders reinforced polymeric composites *Mugla Journal of Science and Technology*, Vol 2, No 1, 88-92, 2016.
- [31] Deng JL, Feng B. Absorbing Properties of Composite Material Plates of Multi-layer Absorbing Structure. In *Advanced Materials Research 2011* (Vol. 287, pp. 9-14). Trans Tech Publications Ltd.
- [32] Kim, J.-B. (2012). Broadband radar absorbing structures of carbon nanocomposites. *Advanced Composite Materials*, 21(4), 333–344.
- [33] Das S, Nayak GC, Sahu SK, Routray PC, Roy AK, Baskey H. Microwave absorption properties of double-layer RADAR absorbing materials based on doped Barium Hexaferrite/TiO<sub>2</sub>/conducting carbon black. *Journal of Engineering*. 2014 Sep 17;2014.
- [34] Teber A, Unver I, Kavas H, Aktas B, Bansal R. Knitted radar absorbing materials (RAM) based on nickel–cobalt magnetic materials. *Journal of Magnetism and Magnetic Materials*. 2016 May 15;406:228-32.
- [35] Lee, Y. S., Malek, M. F. B. A., Cheng, E. M., Liu, W. W., You, K. Y., Iqbal, M. N., Mohd Fariz Bin Haji Abd Malek. (2013). Experimental Determination of The Performance of Rice Husk Carbon Nanotube Composites for Absorbing Microwave

Signals in The Frequency Range Of 12.4-18 GHz. Progress in Electromagnetics Research, 140, 795–812.

[36] Hunjra, M., Fakhar, M., Naveed, K., & Subhani, T. (2016). Polyurethane foam-based radar-absorbing sandwich structures to evade detection. *Journal of Sandwich Structures & Materials*, 19(6), 647–658.

[37] Kim JB, Lim DW. Reduction of radar interference – stealth wind blade structure with carbon nanocomposite sheet. *Wind Energy* 2013.

[38] Jang, H. K., Choi, W. H., Shin, J. H., Song, T. H., Kim, J. K., Kim, C. G., Lim, D. W. (2011). Radar absorbing structure with periodic pattern surfaces for wind turbine blades Proceedings in 18TH International Conference on Composite Materials. Jeju Island, Korea.

[39] Tennant A, Chambers B. Signature management of radar returns from wind turbine generators. *Smart Mater Struct* 2006;15(2):468–72.

[40] Lucchini, E., Meriani, S., Delben, F. et al. A new method for low temperature preparation of barium hexaferrite powders. *J Mater Sci* 19, 121–124 (1984).

[41] Chen, M., Fan, R., Liu, G. F., Wang, X. A., & Sun, K. (2015). Magnetic Properties of Barium Ferrite Prepared by Hydrothermal Synthesis. *Key Engineering Materials*, 655, 178–181.

[42] Radwan, M., Rashad, M., & Hessien, M. (2007). Synthesis and characterization of barium hexaferrite nanoparticles. *Journal of Materials Processing Technology*, 181(1-3), 106–109.4

[43] Arendt R H. (1973) The molten salt synthesis of single magnetic domain BaFe<sub>12</sub>O<sub>19</sub> and SrFe<sub>12</sub>O<sub>19</sub> crystals. *Journal of Solid-State Chemistry*, 8(4): 339–347.

[44] Yoon, K.H., Lee, D.H., Jung, H.J. et al. Molten salt synthesis of anisotropic BaFe<sub>12</sub>O<sub>19</sub> powders. *J Mater Sci* 27, 2941–2945 (1992).

[45] Hai-Feng L, Rong-Zhou G, Xiu-Fang L, Wei Y, Xian W, Li- Ren F, Gang H (2011) Molten salt synthesis and magnetic properties of BaFe<sub>12</sub>O<sub>19</sub> hexaferrite. *J Inorg Mater* 26:792–796.

[46] Li, Y., Wang, Q., & Yang, H. (2009). Synthesis, characterization and magnetic properties on nanocrystalline BaFe<sub>12</sub>O<sub>19</sub> ferrite. *Current applied physics*, 9(6), 1375-1380.

[47] Mozaffari, M., Taheri, M., Amighian, J., (2008), Preparation of barium hexaferrite nanopowders by the sol–gel method, using goethite, *J. Magn. Mater.*, 321: 1285-1289.

- [48] Kanagesan, S., Juesurani, S., Velmurugan, R., & Kumar, C. (2010). Synthesis of barium hexaferrite (BaFe<sub>12</sub>O<sub>19</sub>) using D-fructose as fuel. *Journal of Manufacturing Engineering*, 5, 133-136
- [49] Chen, D.-H., & Chen, Y.-Y. (2001). Synthesis of Barium Ferrite Ultrafine Particles by Coprecipitation in the Presence of Polyacrylic Acid. *Journal of Colloid and Interface Science*, 235(1), 9–14.
- [50] Swarnkar RK, Singh SC, Gopal R. Effect of aging on copper nanoparticles synthesized by pulsed laser ablation in water: structural and optical characterizations. *Bulletin of Materials Science*. 2011 Dec;34(7):1363-9.
- [51] Dubois, L. H., & Girolami, G. S. (1992). Metal-organic chemical vapor deposition of copper and copper oxide from copper tert-butoxide. *Chemistry of Materials*, 4(6), 1169–1175. <https://doi.org/10.1021/cm00024a013> 10.1021/jp984163.
- [52] Masoud Salavati-Niasari, Fatemeh Davar, Synthesis of copper and copper(I) oxide nanoparticles by thermal decomposition of a new precursor, *Materials Letters*, Volume 63, Issues 3–4, 2009, P. 441-4434.
- [53] Devi, T. B., & Ahmaruzzaman, M. (2018). Green synthesis of silver, copper and iron nanoparticles: Synthesis, characterization, and their applications in wastewater treatment. *Green Metal Nanoparticles*, 441–466. <https://doi.org/10.1002/9781119418900.ch13>
- [54] Zain, N. M., Stapley, A. G. F., & Shama, G. (2014). Green synthesis of silver and copper nanoparticles using ascorbic acid and chitosan for antimicrobial applications. *Carbohydrate Polymers*, 112, 195–202. <https://doi.org/10.1016/j.carbpol.2014.05.081>
- [55] Bakar, A., Güven, O., Zezin, A. A., & Feldman, V. I. (2014). Controlling the size and distribution of copper nanoparticles in double and triple polymer metal complexes by X-ray irradiation. *Radiation Physics and Chemistry*, 94, 62–65.
- [56] Dung Dang, T. M., Tuyet Le, T. T., Fribourg-Blanc, E., & Chien Dang, M. (2011). The influence of solvents and surfactants on the preparation of copper nanoparticles by a chemical reduction method. *Advances in Natural Sciences: Nanoscience and Nanotechnology*, 2(2), 025004. <https://doi.org/10.1088/2043-6262/2/2/025004>
- [57] Wang, L. N., Li, M. Y., & Zeng, Q. X. (2012). Synthesis of copper nanoparticles by chemical reduction method and its influential factors. *Advanced Materials Research*, 627, 804–808.

- [58] Khanna P.K., S. Gaikwad, P.V. Adhyapak, N. Singh, R. Marimuthu, Synthesis and characterization of copper nanoparticles, *Materials Letters*, Volume 61, Issue 25, 2007, P. 4711-4714
- [59] Yang, H. Mechanochemical synthesis of cobalt oxide nanoparticles / H. Yang // *Materials Letters*. – 2004. – 58(3-4). – 387-389.
- [60] Janjua, Muhammad Ramzan Saeed Ashraf. "Synthesis of Co<sub>3</sub>O<sub>4</sub> Nano Aggregates by Co-precipitation Method and its Catalytic and Fuel Additive
- [61] Dippong T, Goga F, Avram A. Influence of the cobalt nitrate: Ethylene glycol molar ratio on the formation of carboxylate precursors and cobalt oxides. *Studia Universitatis Babes-Bolyai. Chemia*. 2017 Jan 1;62(3):165-77.
- [62] Orcel G, Hench LL. Use of a Drying Control Chemical Additive (DCCA) in the Sol-Gel Processing of Soda Silicate and Soda Borosilicates. In *Proceedings of the 8th Annual Conference on Composites and Advanced Ceramic Materials: Ceramic Engineering and Science Proceedings 1984 Jan 1 (Vol. 5, pp. 546-555)*. Hoboken, NJ, USA: John Wiley & Sons, Inc..
- [63] Livage J. Basic principles of sol-gel chemistry. In *Sol-Gel Technologies for Glass Producers and Users 2004 (pp. 3-14)*. Springer, Boston, MA.
- [64] Bokov D, Turki Jalil A, Chupradit S, Suksatan W, Javed Ansari M, Shewael IH, Valiev GH, Kianfar E. Nanomaterial by sol-gel method: synthesis and application. *Advances in Materials Science and Engineering*. 2021 Dec 24;2021.
- [65] Scherer GW. Aging and drying of gels. *Journal of Non-Crystalline Solids*. 1988 Mar 1;100(1-3):77-92.
- [66] Yoldas BE. Monolithic glass formation by chemical polymerization. *Journal of materials science*. 1979 Aug;14(8):1843-9.
- [67] Nistico R, Scalarone D, Magnacca G. Sol-gel chemistry, templating and spin-coating deposition: A combined approach to control in a simple way the porosity of inorganic thin films/coatings. *Microporous and Mesoporous Materials*. 2017 Aug 1; 248:18-29.
- [68] Catauro M, Tranquillo E, Dal Poggetto G, Pasquali M, Dell'Era A, Vecchio Cipriotti S. Influence of the heat treatment on the particles size and on the crystalline phase of TiO<sub>2</sub> synthesized by the sol-gel method. *Materials*. 2018 Nov 24;11(12):2364.

- [69] Lakshmi BB, Patrissi CJ, Martin CR. Sol– gel template synthesis of semiconductor oxide micro-and nanostructures. *Chemistry of Materials*. 1997 Nov 18;9(11):2544-50.
- [70] Yilmaz E, Soylak M. Functionalized nanomaterials for sample preparation methods. In *Handbook of Nanomaterials in analytical chemistry* 2020 Jan 1 (pp. 375-413). Elsevier.
- [71] Mackenzie JD. Applications of the sol-gel process. *Journal of Non-Crystalline Solids*. 1988 Mar 1;100(1-3):162-8.
- [72] Dehghanhadikolaie A, Ansary J, Ghoreishi R. Sol-gel process applications: A mini-review. *Proc. Nat. Res. Soc.* 2018 Jun 13;2(1):02008-29.
- [73] Attia YA, editor. *Sol-gel processing and applications*. Springer Science & Business Media; 2012 Dec 6.
- [74] Singh LP, Bhattacharyya SK, Kumar R, Mishra G, Sharma U, Singh G, Ahalawat S. Sol-Gel processing of silica nanoparticles and their applications. *Advances in colloid and interface science*. 2014 Dec 1;214:17-37.
- [75] Opuchovic O, Kreiza G, Senvaitiene J, Kazlauskas K, Beganskiene A, Kareiva A. Sol-gel synthesis, characterization and application of selected sub-microsized lanthanide (Ce, Pr, Nd, Tb) ferrites. *Dyes and Pigments*. 2015 Jul 1;118:176-82.
- [76] Schmidt AH. Chemistry of material preparation by the sol-gel process. *Journal of Non-Crystalline Solids*. 1988 Mar 1;100(1-3):51-64.
- [77] Ermrich M, Opper D. *XRD for the analyst. Getting acquainted with the principles*. Second. Panalytical. 2013.
- [78] Smyth MS, Martin JH. x Ray crystallography. *Molecular Pathology*. 2000 Feb;53(1):8.
- [79] Chauhan A, Chauhan P. Powder XRD technique and its applications in science and technology. *J Anal Bioanal Tech*. 2014 Sep 1;5(5):1-5.
- [80] Pope CG. X-ray diffraction and the Bragg equation. *Journal of chemical education*. 1997 Jan;74(1):129.
- [81] Fish PW. Electron diffraction and the Bragg equation. *Physics Education*. 1971;6(1):7.

- [82] Smith F, editor. Industrial applications of X-ray diffraction. CRC press; 1999 Sep 22.
- [83] Jenkins R, Schreiner WN. Considerations in the design of goniometers for use in X-ray powder diffractometers. Powder Diffraction. 1986 Dec;1(4):305-19.
- [84] Kasai N, Kakudo M, Kasai-Kakudo.... X-ray Diffraction by Macromolecules. Tokyo: Kodansha; 2005 Jul 6.
- [85] Gates-Rector S, Blanton T. The powder diffraction file: a quality materials characterization database. Powder Diffraction. 2019 Dec;34(4):352-60.
- [86] “Fall11-11, Crystallography III, X-ray Diffraction.” Fall11-11, Crystallography III, X-ray Diffraction, [www.geo.arizona.edu/xtal/geos306/fall11-11.htm](http://www.geo.arizona.edu/xtal/geos306/fall11-11.htm). Accessed 29 Jan. 2022.
- [87] Zhou W, Apkarian R, Wang ZL, Joy D. Fundamentals of scanning electron microscopy (SEM). In Scanning microscopy for nanotechnology 2006 (pp. 1-40). Springer, New York, NY.
- [88] Akhtar K, Khan SA, Khan SB, Asiri AM. Scanning electron microscopy: Principle and applications in nanomaterials characterization. In Handbook of materials characterization 2018 (pp. 113-145). Springer, Cham.
- [89] Wiesendanger R, Baumeister W. Scanning tunneling microscopy II: further applications and related scanning techniques. Güntherodt HJ, editor. Berlin: Springer-Verlag; 1992.
- [90] Sun D, Siddiqui MO, Iqbal K. Specialty testing techniques for smart textiles. In Smart Textile Coatings and Laminates 2019 Jan 1 (pp. 99-116). Woodhead Publishing.
- [91] Wu Y, Lin Z, Wu X, Cen K. Dual-beam interferometric particle imaging for size measurement of opaque metal droplet. Powder Technology. 2019 Nov 1;356:31-8.
- [922] Barth HG, editor. Modern methods of particle size analysis. John Wiley & Sons; 1984 Sep 11

- [93] Shekunov BY, Chattopadhyay P, Tong HH, Chow AH. Particle size analysis in pharmaceuticals: principles, methods and applications. *Pharmaceutical research*. 2007 Feb;24(2):203-27.
- [94] Coats AW, Redfern JP. Thermogravimetric analysis. A review. *Analyst*. 1963 Jan 1;88(1053):906-24.
- [95] Brown ME, editor. *Introduction to thermal analysis: techniques and applications*. Dordrecht: Springer Netherlands; 2001 Dec 31.
- [96] Gabbott P, editor. *Principles and applications of thermal analysis*. John Wiley & Sons; 2008 Apr 30.
- [97] Gerber JA, Burmester WL, Sellmyer DJ. Simple vibrating sample magnetometer. *Review of Scientific Instruments*. 1982 May;53(5):691-3.
- [98] Burgei W, Pechan MJ, Jaeger H. A simple vibrating sample magnetometer for use in a materials physics course. *American Journal of Physics*. 2003 Aug;71(8):825.
- [99] Antareza MA, Salim C, Mariyanto M, Rochman JP, Lestari W. HYSGUTS: A MATLAB Graphical User Interface (GUI) for hysteresis loop simulation in Vibrating-Sample Magnetometer (VSM) data. In *Journal of Physics: Conference Series* 2022 Jul 1 (Vol. 2309, No. 1, p. 012028). IOP Publishing.
- [100] Arora A. *Optical and electric field control of magnetism* (Doctoral dissertation, Universität Potsdam).
- [101] Rytting DK. Network analyzer accuracy overview. In *58th ARFTG Conference Digest* 2001 Nov 29 (Vol. 40, pp. 1-13). IEEE.
- [102] Kothari A. *A calibration free vector network analyzer*. Missouri University of Science and Technology; 2013.
- [103] Martens J, Judge DV, Bigelow JA. Uncertainties associated with many-port (> 4) S-parameter measurements using a four-port vector network analyzer. *IEEE transactions on microwave theory and techniques*. 2004 May 4;52(5):1361-8.



- [104] Lott U. Measurement of magnitude and phase of harmonics generated in nonlinear microwave two-ports. *IEEE Transactions on Microwave Theory and Techniques*. 1989 Oct;37(10):1506-11.
- [105] Hoffmann K, Skvor Z. A novel vector network analyzer. *IEEE transactions on microwave theory and techniques*. 1998 Dec;46(12):2520-3.
- [106] Phillips PP, Stawarski CA. *Data collection: Planning for and collecting all types of data*. John Wiley & Sons; 2008 Jan 7.
- [107] Rubinstein RY, Melamed B. *Modern simulation and modeling*. New York: Wiley; 1998 Feb.
- [108] Henkel, A., Garade, M., & Team, E. (2019, August 6). Everything RF. everything RF. Retrieved from <https://www.everythingrf.com/community/what-are-s-parameters>
- [109] Hui R, O'Sullivan M. Basic instrumentation for optical measurement. *Fiber Optic Measurement Techniques*. 2009:129-258.
- [110] Junliang L, Yanwei Z, Cuijing G, Wei Z, Xiaowei Y. One-step synthesis of barium hexaferrite nano-powders via microwave-assisted sol-gel auto-combustion. *Journal of the European Ceramic society*. 2010 Mar 1;30(4):993-7.
- [111] Meng YY, He MH, Zeng Q, Jiao DL, Shukla S, Ramanujan RV, Liu ZW. Synthesis of barium ferrite ultrafine powders by a sol-gel combustion method using glycine gels. *Journal of alloys and compounds*. 2014 Jan 15;583:220-5.
- [112] Surig C, Hempel KA, Bonnenberg D. Hexaferrite particles prepared by sol-gel technique. *IEEE Transactions on Magnetics*. 1994 Nov;30(6):4092-4.
- [113] Armelao L, Barreca D, Gross S, Martucci A, Tieto M, Tondello E. Cobalt oxide-based films: sol-gel synthesis and characterization. *Journal of non-crystalline solids*. 2001 Nov 1;293:477-82.
- [114] Barrera E, Viveros T, Avila A, Quintana P, Morales M, Batina N. Cobalt oxide films grown by a dipping sol-gel process. *Thin Solid Films*. 1999 Jun 1;346(1-2):138.

- [115] Luna, I.Z., Hilary, L.N., Chowdhury, A.M.S., Gafur, M.A., Khan, N. and Khan, R.A. (2015) Preparation and Characterization of Copper Oxide Nanoparticles Synthesized via Chemical Precipitation Method. Open Access Library Journal, 2: e1409. <http://dx.doi.org/10.4236/oalib.1101409>.
- [116] Asiri S, Güner S, Demir AY, Yildiz A, Manikandan A, Baykal A. Synthesis and magnetic characterization of Cu substituted barium hexaferrites. Journal of Inorganic and Organometallic Polymers and Materials. 2018 May;28(3):1065-71.
- [117] Iravani S, Varma RS. Sustainable synthesis of cobalt and cobalt oxide nanoparticles and their catalytic and biomedical applications. Green Chemistry. 2020;22(9):2643-61.
- [118] Sardjono SA, Puspitasari P. Synthesis and characterization of cobalt oxide nanoparticles using sol-gel method. In AIP Conference Proceedings 2020 Apr 21 (Vol. 2231, No. 1, p. 040046). AIP Publishing LLC.
- [119] Mohebbi E, Hasani S, Nouri-Khezrabad M, Ziarati A. The effect of agarose agent on the structural, magnetic and optical properties of barium hexaferrite nanoparticles synthesized by sol-gel auto-combustion method. Ceramics International. 2022 Nov 13.
- [120] Junliang L, Wei Z, Cuijing G, Yanwei Z. Synthesis and magnetic properties of quasi-single domain M-type barium hexaferrite powders via sol-gel auto-combustion: Effects of pH and the ratio of citric acid to metal ions (CA/M). Journal of Alloys and Compounds. 2009 Jun 24;479(1-2):863-9..
- [121] Dippong T, Goga F, Avram A. Influence of the cobalt nitrate: Ethylene glycol molar ratio on the formation of carboxylate precursors and cobalt oxides. Studia Universitatis Babeş-Bolyai. Chemia. 2017 Jan 1;62(3):165-77.
- [122] Khan, Ayesha, Audil Rashid, Rafia Younas, and Ren Chong. "A Chemical Reduction Approach to the Synthesis of Copper Nanoparticles." International Nano Letters 6, no. 1 (2015): 21–26. <https://doi.org/10.1007/s40089-015-0163-6>.

- [123] Yue Z, Zhou J, Li L, Zhang H, Gui Z. Synthesis of nanocrystalline NiCuZn ferrite powders by sol–gel auto-combustion method. *Journal of Magnetism and magnetic materials*. 2000 Jan 1;208(1-2):55-60.
- [124] Mali A, Ataie A. Structural characterization of nano-crystalline BaFe<sub>12</sub>O<sub>19</sub> powders synthesized by sol–gel combustion route. *Scripta Materialia*. 2005 Nov 1;53(9):1065-70.
- [125] Liu X, Zhao SF, Shao Y, Yao KF. Facile synthesis of air-stable nano/submicro dendritic copper structures and their anti-oxidation properties. *RSC Advances*. 2014;4(63):33362-5.
- [126] Gryzunova NN, Vikarchuk AA, Gryzunov AM, Romanov AE. COPPER CRYSTALS WITH FRAGMENTED STRUCTURE AND DEVELOPED SURFACE IN TEMPERATURE FIELDS. *Materials Physics & Mechanics*. 2017 Sep 1;32(2).
- [127] Basolo F, Murmann RK, Whitney JE, Rollinson CL. Acidopentamminecobalt (III) salts. *Inorganic Syntheses*. 1953 Jan 1;4:171-6.
- [128] Wendlandt WW. Thermal decomposition of metal complexes—III: Stoichiometry of the thermal dissociation of some hexamminecobalt (III) complexes. *Journal of Inorganic and Nuclear Chemistry*. 1963 May 1;25(5):545-51.
- [129] Shepherd P, Mallick KK, Green RJ. Magnetic and structural properties of M-type barium hexaferrite prepared by co-precipitation. *Journal of magnetism and magnetic materials*. 2007 Apr 1;311(2):683-92.
- [130] Xu G, Ma H, Zhong M, Zhou J, Yue Y, He Z. Influence of pH on characteristics of BaFe<sub>12</sub>O<sub>19</sub> powder prepared by sol–gel auto-combustion. *Journal of Magnetism and Magnetic Materials*. 2006 Jun 1;301(2):383-8.
- [131] Li Y, Wang Q, Yang H. Synthesis, characterization and magnetic properties on nanocrystalline BaFe<sub>12</sub>O<sub>19</sub> ferrite. *Current applied physics*. 2009 Nov 1;9(6):1375-80.
- [132] Yu HF. BaFe<sub>12</sub>O<sub>19</sub> powder with high magnetization prepared by acetone-aided coprecipitation. *Journal of Magnetism and Magnetic Materials*. 2013 Sep 1;341:79-85.

- [133] Zhong W, Ding W, Zhang N, Hong J, Yan Q, Du Y. Key step in synthesis of ultrafine BaFe<sub>12</sub>O<sub>19</sub> by sol-gel technique. *Journal of Magnetism and Magnetic Materials*. 1997 Apr 1;168(1-2):196-202.
- [134] Shalini MG, Subha A, Sahu B, Sahoo SC. Phase evolution and temperature dependent magnetic properties of nanocrystalline barium hexaferrite. *Journal of Materials Science: Materials in Electronics*. 2019 Jul;30(14):13647-54.
- [135] Ullah AA, Amin FB, Hossain A. Tailoring surface morphology and magnetic property by precipitants concentrations dependent synthesis of Co<sub>3</sub>O<sub>4</sub> nanoparticles. *Ceramics International*. 2020 Dec 1;46(17):27892-6.
- [136] Zdorovets MV, Shumskaya AE, Kozlovskiy AL. Investigation of the effect of phase transformations on the magnetic and electrical properties of Co/Co<sub>3</sub>O<sub>4</sub> nanowires. *Journal of Magnetism and Magnetic Materials*. 2020 Mar 1;497:166079.
- [137] Anandhababu G, Ravi G. Facile synthesis of quantum sized Co<sub>3</sub>O<sub>4</sub> nanostructures and their magnetic properties. *Nano-Structures & Nano-Objects*. 2018 Jul 1;15:1-9.
- [138] Mammadyarova SJ. Synthesis And Characterization Of Cobalt Oxide Nanostructures A Brief Review. *Azerbaijan Chemical Journal*. 2021(2):80-93.
- [139] Samokhvalov AA, Arbusova TI, Viglin NA, Naumov SV, Galakhov VR, Zatsepin DA, Kotov YA, Samatov OM, Kleshchev DG. Paramagnetism in copper monoxide systems. *Physics of the Solid State*. 1998 Feb;40(2):268-71.
- [140] Kumar A, Singh S. Development of coatings for radar absorbing materials at X-band. *InIOP Conference Series: Materials Science and Engineering 2018 Mar 1 (Vol. 330, No. 1, p. 012006)*. IOP Publishing.
- [141] Deng, Jing Lan, and Bing Feng. "Absorbing Properties of Composite Material Plates of Multi-Layer Absorbing Structure." *Advanced Materials Research* 287-290 (2011): 9–14. <https://doi.org/10.4028/www.scientific.net/amr.287-290.9>
- [142] Wang L, Jia X, Li Y, Yang F, Zhang L, Liu L, Ren X, Yang H. Synthesis and microwave absorption property of flexible magnetic film based on graphene

oxide/carbon nanotubes and Fe<sub>3</sub>O<sub>4</sub> nanoparticles. *Journal of Materials Chemistry A*. 2014;2(36):14940-6.

[143] Lee, Sang-Eui, Ji-Ho Kang, and Chun-Gon Kim. 2006. "Fabrication and Design of Multi-layered Radar Absorbing Structures of MWNT-filled Glass/epoxy Plain-weave Composites." *Composite Structures* 76 (4) (December): 397–405

[144] Li BW, Shen Y, Yue ZX, Nan CW. Influence of particle size on electromagnetic behavior and microwave absorption properties of Z-type Ba-ferrite/polymer composites. *Journal of Magnetism and Magnetic Materials*. 2007 Jun 1;313(2):322-8.

[145] Zhang, Baoshan, Yong Feng, Jie Xiong, Yi Yang, and Huaixian Lu. 2006. "Microwave-absorbing Properties of De-aggregated Flake-shaped Carbonyl-iron Particle Composites at 2-18 GHz." *IEEE Transactions on Magnetics* 42 (7) (July): 1778–1781

[146] Li W, Li C, Lin L, Wang Y, Zhang J. All-dielectric radar absorbing array metamaterial based on silicon carbide/carbon foam material. *Journal of Alloys and Compounds*. 2019 Apr 15;781:883-91.

[147] Liu Y, Zhang Z, Xiao S, Qiang C, Tian L, Xu J. Preparation and properties of cobalt oxides coated carbon fibers as microwave-absorbing materials. *Applied Surface Science*. 2011 Jun 15;257(17):7678-83.

[148] Tang X, Yang Y. Surface modification of M-Ba-ferrite powders by polyaniline: towards improving microwave electromagnetic response. *Applied Surface Science*. 2009 Sep 15;255(23):9381-5.

[149] Feng YB, Qiu T, Shen CY, Li XY. Electromagnetic and absorption properties of carbonyl iron/rubber radar absorbing materials. *IEEE Transactions on Magnetics*. 2006 Feb 21;42(3):363-8.

[150] Xiang J, Li J, Zhang X, Ye Q, Xu J, Shen X. Magnetic carbon nanofibers containing uniformly dispersed Fe/Co/Ni nanoparticles as stable and high-performance electromagnetic wave absorbers. *Journal of Materials Chemistry A*. 2014;2(40):16905-14

- [151] Ghasemi A, Hossienpour A, Morisako A, Saatchi A, Salehi M. Electromagnetic properties and microwave absorbing characteristics of doped barium hexaferrite. *Journal of Magnetism and Magnetic Materials*. 2006 Jul 1;302(2):429-35.
- [152] Xu, F., Ma, L., Huo, Q., Gan, M. and Tang, J., “Microwave absorbing properties and structural design of microwave absorbers based on polyaniline and polyaniline/magnetite nanocomposite”, *Journal of Magnetism and Magnetic Materials*, 374; 311-316 (2015).
- [153] Jun Z, Huiqing F, Yangli W, Shiquan Z, Jun X, Xinying C. Ferromagnetic and microwave absorption properties of copper oxide/cobalt/carbon fiber multilayer film composites. *Thin Solid Films*. 2012 May 31;520(15):5053-9.
- [154] Handoko E, Sugihartono I, Budi S, Randa M, Jalil Z, Alaydrus M. The effect of thickness on microwave absorbing properties of barium ferrite powder. In *Journal of Physics: Conference Series* 2018 Aug 1 (Vol. 1080, No. 1, p. 012002). IOP Publishing.
- [155] Xu, Yonggang, Deyuan Zhang, Jun Cai, Liming Yuan, and Wenqiang Zhang. 2013. “Microwave Absorbing Property of Silicone Rubber Composites with Added Carbonyl Iron Particles and Graphite Platelet.” *Journal of Magnetism and Magnetic Materials* 327 (February): 82–86.
- [156] Tellakula, R a, V K Varadan, T C Shami, and G N Mathur. 2004. “Carbon Fiber and Nanotube Based Composites with Polypyrrole Fabric as Electromagnetic Absorbers.” *Smart Materials and Structures* 13 (5) (October 1): 1040–1044.
- [157] Sun J, Wang L, Yang Q, Shen Y, Zhang X. Preparation of copper-cobalt-nickel ferrite/graphene oxide/polyaniline composite and its applications in microwave absorption coating. *Progress in Organic Coatings*. 2020 Apr 1;141:105552.
- [158] Wu N, Qiao J, Liu J, Du W, Xu D, Liu W. Strengthened electromagnetic absorption performance derived from synergistic effect of carbon nanotube hybrid with Co@ C beads. *Advanced Composites and Hybrid Materials*. 2018 Mar;1(1):149-59.
- [159] Parsian P, Dorraji MS, Hosseini SF, Rasoulifard MH, Hajimiri I, Amani-Ghadim AR. Facile preparation of an enhanced microwave absorbing based on polyester

composite containing  $\text{Ca}_3\text{Al}_2\text{Si}_3\text{O}_{12}$ , polyaniline, and spinel ferrite (Cu, Mg, and Ni) nanoparticles. *Materials Chemistry and Physics*. 2020 Nov 15;255:123529.

[160] Mosleh Z, Kameli P, Poorbaferani A, Ranjbar M, Salamati H. Structural, magnetic and microwave absorption properties of Ce-doped barium hexaferrite. *Journal of Magnetism and Magnetic Materials*. 2016 Jan 1;397:101-7.

[161] Chang S, Kangning S, Pengfei C. Microwave absorption properties of Ce-substituted M-type barium ferrite. *Journal of Magnetism and Magnetic Materials*. 2012 Mar 1;324(5):802-5.

[162] Lee, Sang-Eui, Ji-Ho Kang, and Chun-Gon Kim. 2006. "Fabrication and Design of Multi-layered Radar Absorbing Structures of MWNT-filled Glass/epoxy Plain-weave Composites." *Composite Structures* 76 (4) (December): 397–405

[163] Yang, C. C., Gung, Y. J., Hung, W. C., Ting, T. H. and Wu, K. H., "Infrared and microwave absorbing properties of  $\text{BaTiO}_3$ /polyaniline and  $\text{BaFe}_{12}\text{O}_{19}$ / polyaniline composites", *Composites Science and Technology*, 70; 466-471 (2010).

[164] Shyr TW, Shie JW. Electromagnetic shielding mechanisms using soft magnetic stainless-steel fiber enabled polyester textiles. *Journal of Magnetism and Magnetic Materials*. 2012 Nov 1;324(23):4127-32.

# Curriculum Vitae

Name Surname : Mohamed Yousef Ali Issa

## Education:

- 2017–2022 PhD. Material Science and Engineering, İzmir Katip Çelebi Üniversitesi,
- 2018–2020 M.Sc. Material science and Engineering, National University of science and technology “MISIS,
- 2009-2013 B.Sc. Petroleum Engineering, University of Benghazi,